ESTIMATION ALGORITHM FOR AUTONOMOUS AERIAL REFUELING USING A VISION BASED RELATIVE NAVIGATION SYSTEM

A Thesis

by

ROSHAWN ELIZABETH BOWERS

Submitted to the Office of Graduate Studies of
Texas A&M University
in partial fulfillment of the requirements for the degree of

MASTER OF SCIENCE

August 2005

Major Subject: Aerospace Engineering

ESTIMATION ALGORITHM FOR AUTONOMOUS AERIAL REFUELING USING A VISION BASED RELATIVE NAVIGATION SYSTEM

A Thesis

by

ROSHAWN ELIZABETH BOWERS

Submitted to the Office of Graduate Studies of
Texas A&M University
in partial fulfillment of the requirements for the degree of

MASTER OF SCIENCE

Approved by:

Chair of Committee,	John Valasek
Committee Members,	John L. Junkins
	John E. Hurtado
	Reza Langari
Head of Department,	Helen L. Reed

August 2005

Major Subject: Aerospace Engineering

ABSTRACT

Estimation Algorithm for Autonomous Aerial Refueling
Using a Vision Based Relative Navigation System. (August 2005)
Roshawn Elizabeth Bowers, B.S., Texas A&M University
Chair of Advisory Committee: Dr. John Valasek

A new impetus to develop autonomous aerial refueling has arisen out of the growing demand to expand the capabilities of unmanned aerial vehicles (UAVs). With autonomous aerial refueling, UAVs can retain the advantages of being small, inexpensive, and expendable, while offering superior range and loiter-time capabilities. VisNav, a vision based sensor, offers the accuracy and reliability needed in order to provide relative navigation information for autonomous probe and drogue aerial refueling for UAVs. This thesis develops a Kalman filter to be used in combination with the VisNav sensor to improve the quality of the relative navigation solution during autonomous probe and drogue refueling. The performance of the Kalman filter is examined in a closed-loop autonomous aerial refueling simulation which includes models of the receiver aircraft, VisNav sensor, Reference Observer-based Tracking Controller (ROTC), and atmospheric turbulence. The Kalman filter is tuned and evaluated for four aerial refueling scenarios which simulate docking behavior in the absence of turbulence, and with light, moderate, and severe turbulence intensity. The docking scenarios demonstrate that, for a sample rate of 100 Hz, the tuning and performance of the filter do not depend on the intensity of the turbulence, and the Kalman filter improves the relative navigation solution from VisNav by as much as 50% during the early stages of the docking maneuver. For the aerial refueling scenarios modeled

in this thesis, the addition of the Kalman filter to the VisNav/ROTC structure resulted in a small improvement in the docking accuracy and precision. The Kalman filter did not, however, significantly improve the probability of a successful docking in turbulence for the simulated aerial refueling scenarios.

To my parents

ACKNOWLEDGMENTS

Many people contributed to the successful completion of this thesis, most notably Dr. John Valasek, who has been an exceptional advisor and mentor throughout my graduate career. I have greatly benefited from his dedication to my academic and professional success. The assistance of my committee in reviewing the technical aspects of this thesis is acknowledged and greatly appreciated. I am thankful to Dr. John Junkins for contributing the formulation of the Kalman filter for relative navigation, and for offering his time and expertise to help me understand the VisNav system, Kalman filters, and how they might work together. I also would like to thank Dr. John Hurtado and Dr. Reza Langari, whose guidance has been invaluable to my understanding of dynamic systems and control theory. I am very thankful to Monish Tandale for developing the Reference Observer-based Tracking Controller, and for the many useful insights he provided that greatly aided my understanding of the controller. Credit is due to Jeff Morris and Brian Wood at StarVision, Inc. for the creation of the VisNav sensor simulation code. Thanks to Steve Chambers for all of his encouragement and support, and for his editorial suggestions that greatly improved the quality of this thesis. I wish to thank Josh O'Neil, Andy Sinclair, and Lesley Weitz, whose friendship made the graduate school experience all the more enjoyable and rewarding for me. Finally, I am most grateful to my family, whose love and support made everything possible.

TABLE OF CONTENTS

CHAPTER Page

I INTRODUCTION 1

II AERIAL REFUELING 4

A. Overview of In-Flight Refueling Methods 4
1. Flying Boom 5
2. Probe and Drogue 7
B. Modeling 10
C. Autonomous Aerial Refueling 12
1. Sensors 13
2. Control 17

III THE VISNAV SYSTEM 22

A. System Description 22
B. Measurement Model 26
C. Gaussian Least Squares Differential Correction Algorithm . 29

IV VISNAV KALMAN FILTER 34

A. Discrete-Time Linear Kalman Filter 34
B. Kalman Filter Design for Relative Navigation 39
C. Tuning the Kalman Filter for Aerial Refueling 41

V REFERENCE OBSERVER-BASED TRACKING CONTROLLER 44

A. Control Objective 44
B. Reference Trajectory Generation 47
1. Stage I: Initial Alignment 49
2. Stage II: End Game Precision Tracking 50
C. Observer Design 51
D. Trajectory Tracking Controller Design 54
1. Continuous Controller 54
2. Sampled-Data Controller 57
E. Frequency Domain Analysis 58

VI AUTONOMOUS AERIAL REFUELING SIMULATION 65

CHAPTER Page

A. Receiver Linear Aircraft Model 65
B. Drogue Model 68
C. Atmospheric Turbulence Model 70
D. VisNav Sensor Model 72

VII EXPERIMENT DESIGN 79

A. Autonomous Aerial Refueling Scenario 80
B. Selection of ROTC Design Parameters 81
C. Kalman Filter Tuning Criteria 83
D. Evaluation of Closed-loop Performance with Combined VisNav and Kalman Filter 84

VIII NUMERICAL EXAMPLES 85

A. Tuning Case 1: No Turbulence 85
B. Tuning Case 2: Light Turbulence 94
C. Tuning Case 3: Moderate Turbulence 103
D. Tuning Case 4: Severe Turbulence 112
E. Closed-loop Performance with the Kalman Filter 120
1. Moderate Turbulence with Kalman Filter 120
2. Tuned Kalman Filter Simulation Results 124
F. Summary of Results 126

IX CONCLUSIONS 128

X RECOMMENDATIONS 131

REFERENCES 134

APPENDIX A 140

VITA 145

LIST OF TABLES

TABLE		Page
I	Summary of navigation systems for autonomous aerial refueling	18
II	Discrete-time linear Kalman filter [31]	38
III	UCAV6 steady, level $1g$ trim states	66
IV	Receiver aircraft linear model states and controls	67
V	UCAV6 control position and rate limits [29]	68
VI	Drogue dynamic model parameters	69
VII	Kalman filter tuning cases for autonomous aerial refueling	81
VIII	Reference trajectory design parameters and critical times	82
IX	Simulation results, no turbulence	124
X	Simulation results, light turbulence	124
XI	Simulation results, moderate turbulence	125
XII	Simulation results, severe turbulence	125
XIII	Summary of tuning cases	127

LIST OF FIGURES

FIGURE		Page
1	KC-135 Stratotanker refuels an F-16 Fighting Falcon using the boom method. (U.S. Air Force photo by Tech. Sgt. Mike Buytas) . .	6
2	Boom operator prepares to transfer fuel to a KC-10 Extender during Operation Iraqi Freedom. (U.S. Air Force photo by Master Sgt. Terry L. Blevins)	7
3	F/A-18E Super Hornet performs an in flight refueling evolution with an F/A-18C Hornet over the Pacific Ocean using the probe and drogue technique. (U.S. Navy photo by Lt. Perry Solomon) . . .	8
4	Navy F/A-18F Super Hornet is refueled by a KC-135R Stratotanker using a boom-drogue adapter. (U.S. Air Force photo by Senior Airman Joshua Strang)	9
5	Two F/A-18 aircraft involved in NASA Dryden's Automated Aerial Refueling project fly over the California desert. (NASA photo by Carla Thomas)	11
6	Nonzero Set Point (NZSP) control structure	19
7	Command Generator Tracker (CGT) control structure	20
8	VisNav system architecture (Reprinted with permission from "Vision-Based Sensor and Navigation System for Autonomous Air Refueling" by J. Valasek, K. Gunnam, J. Kimmett, M. Tandale, J.L. Junkins and D. Hughes, 2005. *Journal of Guidance, Control, and Dynamics* (accepted)).	23
9	The VisNav sensor	24
10	Illustration of VisNav operation	25
11	VisNav active beacons in three sizes	26

FIGURE Page

12 Ideal pin-hole model for VisNav sensor 27

13 Gaussian Least Squares Differential Correction (GSLDC) algorithm . 33

14 Sample tuning parameters for the Kalman filter 43

15 Reference Observer-based Tracking Controller (ROTC) block diagram 45

16 Autonomous aerial refueling coordinate frames 46

17 Reference trajectory design 49

18 Singular values of $T_1(s)$ 60

19 Singular values of $T_2(s)$ 62

20 Singular values of $T_3(s)$ 63

21 Singular values of $T_3(s)G_g$ and Dryden gust spectral density 63

22 AV-8B Harrier during probe and drogue refueling 66

23 Medium/high altitude turbulence intensities [39] 71

24 VisNav sensor simulation diagram 73

25 VisNav sensor simulation with calibration model 75

26 Comparison of VisNav sensor simulation a) without calibration model and b) with calibration model 77

27 3-dimensional view of beacon configuration for AAR simulation . . . 78

28 Beacon configuration for AAR simulation 78

29 Kalman filter placement in ROTC block diagram 84

30 Receiver aircraft and drogue trajectories (case 1, no turbulence) . . . 86

31 Drogue position and velocity (case 1, no turbulence) 86

32 Tracking error (case 1, no turbulence) 87

FIGURE Page

33 Receiver aircraft states (case 1, no turbulence) 89
34 Receiver aircraft controls and control rates (case 1, no turbulence) . . 90
35 VisNav error and 3σ bounds from GLSDC (case 1, no turbulence) . . 92
36 Tuned Kalman filter error and 3σ bounds (case 1, no turbulence) . . 92
37 Comparison of Kalman filter and GLSDC errors (case 1, no turbulence) 93
38 Receiver aircraft and drogue trajectories (case 2, light turbulence) . . 94
39 Drogue position and velocity (case 2, light turbulence) 95
40 Tracking error (case 2, light turbulence) 96
41 Receiver aircraft states (case 2, light turbulence) 98
42 Receiver aircraft controls and control rates (case 2, light turbulence) 99
43 VisNav error and 3σ bounds from GLSDC (case 2, light turbulence) . 101
44 Tuned Kalman filter error and 3σ bounds (case 2, light turbulence) . 101
45 Comparison of Kalman filter and GLSDC errors (case 2, light turbulence)102
46 Receiver aircraft and drogue trajectories (case 3, moderate turbulence) 103
47 Drogue position and velocity (case 3, moderate turbulence) 104
48 Tracking error (case 3, moderate turbulence) 105
49 Receiver aircraft states (case 3, moderate turbulence) 107
50 Receiver aircraft controls and control rates (case 3, moderate turbulence)108
51 VisNav error and 3σ bounds from GLSDC (case 3, moderate turbulence)110
52 Tuned Kalman filter error and 3σ bounds (case 3, moderate turbulence)110
53 Comparison of Kalman filter and GLSDC errors (case 3, moderate turbulence) 111

FIGURE Page

54 Receiver aircraft and drogue trajectories (case 4, severe turbulence) . 112

55 Drogue position and velocity (case 4, severe turbulence) 113

56 Tracking error (case 4, severe turbulence) 114

57 Receiver aircraft states (case 4, severe turbulence) 115

58 Receiver aircraft controls and control rates (case 4, severe turbulence) 117

59 VisNav error and 3σ bounds from GLSDC (case 4, severe turbulence) 118

60 Tuned Kalman filter error and 3σ bounds (case 4, severe turbulence) 118

61 Comparison of Kalman filter and GLSDC errors (case 4, severe turbulence) 119

62 Receiver aircraft and drogue trajectories, moderate turbulence, with Kalman filter 121

63 Kalman filter error and 3σ bounds, moderate turbulence 121

64 Receiver aircraft states, moderate turbulence, with Kalman filter . . 122

65 Receiver aircraft controls, moderate turbulence, with Kalman filter . 123

CHAPTER I

INTRODUCTION

Aerial refueling is a critical capability for the United States military, enabling tactical aircraft to reach distant theaters of operation and patrol aircraft to stay airborne for extended periods of time. A new impetus to develop autonomous aerial refueling (without a pilot or operator) has arisen out of the growing demand to expand the capabilities of unmanned aerial vehicles (UAVs).

UAVs are becoming important elements in the military and homeland security sectors because they are well-suited for missions that are dangerous or physically demanding for a human pilot. UAVs can be inexpensive, "expendable" tools for surveillance, reconnaissance, communications, and attack operations. UAVs are also capable of performing a wide variety of missions in the civilian and commercial sectors. Examples are search and rescue missions, disaster relief efforts, border patrol, traffic monitoring, meteorological research, and land management.

The need to stay in the air longer has caused modern UAVs to increase in size to accommodate larger amounts of fuel. These vehicles are not only more costly to build and maintain, but the significant weight of fuel reduces the payload capacity of the aircraft. Large UAVs also pose a greater risk to civilians when operating over populated areas. Autonomous aerial refueling (AAR) is an economical and technologically feasible way to increase the range and endurance of UAVs without increasing their size. A UAV with the ability to refuel in-flight could loiter on-station for two or more times as long as an un-refueled UAV, with room for additional payload [1]. With AAR, UAVs could retain the advantages of being small, inexpensive, and

---

The journal model is *IEEE Transactions on Automatic Control*.

expendable, while offering superior range and loiter time capabilities.

Currently there are two methods for aerial refueling used throughout the world: the boom method and the probe and drogue method. The refueling technique considered in this research is modeled after the probe and drogue method currently used by the United States Navy. During the refueling process, the tanker aircraft deploys a long refueling hose with an aerodynamically stabilized receptacle called a drogue attached to the end. The tanker aircraft maintains steady level flight while the receiver aircraft maneuvers to dock its refueling probe with the drogue. With the need for extremely precise movements and the susceptibility to pilot-induced oscillation, probe and drogue refueling is widely considered to be the most challenging task required of a human pilot. Many of the same difficulties must be addressed in the development of a system for autonomous aerial refueling.

Thus far, the main obstacle in developing AAR has been the lack of adequate sensors for measuring the relative position and orientation of the receiver vehicle. The rapid control corrections needed for docking, especially in turbulence, require navigation updates at a rate not yet achieved by current sensor technology. For example, DGPS (Differential Global Positioning System) provides navigation updates at a maximum of 10 Hz, and requires multiple satellite links which are subject to dropouts. Optical sensors based on pattern recognition or visual servoing are even slower because of the large computational burden required to obtain an accurate navigation solution. VisNav, a new vision-based sensor, offers the accuracy and reliability needed for a variety of relative navigation needs [2]. VisNav can provide measurements more accurately (within 1cm or 0.25 deg at 30 meters away) at a rate ten times that of DGPS. The VisNav sensor opens the door to a feasible AAR system. With its small size and low power requirements, VisNav can be easily integrated onto most UAV platforms.

Detailed simulations of the VisNav sensor have shown that the navigation solution is highly sensitive to the beacon configuration on the aircraft. Moreover, the navigation solution may be degraded or lost in the event that one or more beacons falls outside of the field of view of the sensor. This situation is most apparent at long range, when even a small change in the attitude of the receiver causes the beacons and the drogue to be lost from sight. In the event that the sensor fails to obtain a navigation solution, the current VisNav hardware is programed to return the last available estimate. In docking situations this can lead to problems when the controller is being told that the relative position is constant, when in fact the two vehicles are moving toward each other.

This situation can be improved with a Kalman filter, which may be able to offer an updated estimate in the event no measurement from VisNav is available. It may also allow the VisNav sensor to run at a slower rate (the current system updates at 100 Hz), thus saving computation time and power. Another use for the Kalman filter is to combine measurements from other sensors, such as DGPS or an IMU, with VisNav to further improve the solution. At this point it is unclear which combination of sensors is necessary to achieve successful docking. This will largely depend on the controller that is used and the operating conditions during docking.

The goal of this research is to develop an estimation tool to be used in combination with the VisNav sensor to improve the quality of the navigation solution from VisNav. Initial simulations show that using a Kalman filter with VisNav can improve the accuracy of the navigation solution by as much as 50%. In addition, it is likely that improved controller designs will need estimates of relative velocity and acceleration to ensure proper closing rate and engagement force. Finally, the Kalman filter will add fault tolerance to the AAR system by giving an updated navigation solution in the event that the VisNav sensor fails during docking.

CHAPTER II

AERIAL REFUELING

Since the invention of the airplane in 1903, engineers and aviation enthusiasts have sought ways to expand the role of aircraft in fulfilling a variety of transportation, military, and scientific needs. The concept of in-flight refueling was proposed by the some of the earliest aviators as a way to stay in the air longer. It has since become a critical capability for military aircraft across the globe.

Air-to-air refueling is an important military technology for several strategic reasons. The first is that it extends the combat radius of attack aircraft, fighters, and bombers so they may reach distant theaters of operation. Air refueling also increases the effectiveness of surveillance and patrol aircraft by allowing them to remain in the air longer. In addition, these aircraft can carry more payload than would be possible if they had to take off with fuel for an entire mission. Air refueling alleviates the need for forward air bases stationed throughout the world that act as deployment centers and filling stations.

This chapter will introduce and define the aerial refueling problem. Section A describes historical and modern methods of in-flight refueling. Approaches to modeling various aspects of air refueling are discussed in Section B. Finally, Section C presents issues and considerations for autonomous aerial refueling.

A. Overview of In-Flight Refueling Methods

The first attempts at transferring fuel in flight were awkward and often dangerous. In 1921, for example, one daring wing walker climbed from the wing of his Lincoln Standard biplane onto the wing of a Curtiss Jenny with a five-gallon can of gasoline strapped to his back. The first true air refueling took place in 1923 when Capt. Lowell

Smith and Lt. John P. Richter refueled their De Havilland DH-4 fourteen times during a flight over Southern California. Their refueling method was simple: a 40-foot hose reinforced with steel cable was tossed out of the tanker and a crewman on the receiver grabbed it as it whipped in the wind. The technique worked, but the crewman on the receiver was often drenched with fuel when turbulence caused the hose to disengage unexpectedly [3, 4].

Some of the first standard refueling equipment and techniques were developed by Lt. Richard Atcherly of Britain's Royal Air Force. In 1935 he patented the looped hose method, in which both the tanker and receiver aircraft release cables that trail behind them. As the tanker crosses from left to right above the receiver, the two cables engage. A hose attached to the tanker's cable is then reeled in by the receiver crew, and refueling takes place. Another Englishman named Alan Cobham and his company Flight Refueling, Ltd. later purchased the patent for the looped hose method and made further improvements. The system worked well but was limited to low speeds, so fighters could not be refueled. In addition, skilled operators were required in both aircraft, and the refueling operator in the tanker was left completely exposed to the elements [3, 4]. Although modern methods are vastly improved in terms of performance, safety and reliability, aerial refueling remains one of the most challenging operations required of a pilot and crew.

1. Flying Boom

The flying boom method was developed for the United States Air Force by the Boeing Aircraft Company. In this technique a boom operator in the tanker aircraft maneuvers an extendable pipe equipped with ruddervators into a refueling port on the receiver (Figs. 1 and 2). The pilot of the receiver aircraft must maintain the relative positioning to the tanker during the refueling operation. When it was introduced in

Fig. 1. KC-135 Stratotanker refuels an F-16 Fighting Falcon using the boom method. (U.S. Air Force photo by Tech. Sgt. Mike Buytas)

the late 1940's, the boom refueling system offered many advantages over the looped hose method. Connection between the receiver and the boom could be established in seconds, whereas the old system took at least four minutes under ideal conditions. In addition, the large diameter of the boom permitted a high flow rate, enabling large amounts of fuel to be transferred very quickly [4].

There are several drawbacks to the boom refueling method. The drag penalty on the tanker due to the rigid boom is significant, and under certain flight conditions the boom will experience buffet, a high frequency instability caused by flow separation. In addition there are mechanical limits that do not allow the boom to move in certain directions. [4] notes that "this narrows its operating envelope and requires a high degree of pilot skill to maintain the required close formation, especially during the latter portion of the refueling operation, when the receiver aircraft is reaching its maximum weight and becomes sluggish in handling characteristics."

Another problem with boom refueling has to do with the fact that the boom acts as a rigid connection between the tanker and receiver. When the two aircraft experience a gust, for instance, the relative motion must be accommodated by the boom. The pressure and flow rate of the fuel can cause the boom to develop a

Fig. 2. Boom operator prepares to transfer fuel to a KC-10 Extender during Operation Iraqi Freedom. (U.S. Air Force photo by Master Sgt. Terry L. Blevins)

certain rigidity along the telescoping axis. In most cases this causes an inadvertent disconnect and lengthens the time required to refuel. In the worst case, a gust can cause structural failure of the boom or a collision between the two aircraft. To avoid such accidents extensive emergency break-away procedures have been established and both boom operators and pilots are required to undergo intensive training [4].

2. Probe and Drogue

The probe and drogue technique was introduced in 1949 by Flight Refueling, Ltd. as an alternative to the flying boom. It is currently the refueling method of choice for the United States Navy and armed forces around the world. During this refueling process, the tanker aircraft deploys a long refueling hose with an aerodynamically stabilized receptacle called a drogue attached to the end. The tanker aircraft maintains steady level flight while the receiver maneuvers a refueling probe into the drogue (Fig. 3). An automatic coupling mechanism is activated as the probe enters the drogue, and fuel begins to flow. A reel take-up system maintains tension in the hose throughout

Fig. 3. F/A-18E Super Hornet performs an in flight refueling evolution with an F/A-18C Hornet over the Pacific Ocean using the probe and drogue technique. (U.S. Navy photo by Lt. Perry Solomon)

the operation[4, 3].

The probe and drogue system is capable of higher operating speeds than the flying boom; and because the hose is flexible, refueling in higher levels of turbulence is also possible. The system is simpler in that it does not require a highly trained operator in the tanker. The probe and drogue technique is well suited for agile aircraft such as fighters and helicopters, whose pilots generally prefer it over the flying boom. Although the larger diameter of the boom allows for a higher fuel flow rate, the decreased number of inadvertent disconnects with probe and drogue refueling system gives it almost the same average rate of transfer [4, 3]. The system has also made possible the idea of multipoint refueling, where several aircraft refuel from the same tanker simultaneously [5].

Although the flying boom and probe and drogue refueling systems are quite different, some effort has been made to solve their compatibility issues. A tanker that

Fig. 4. Navy F/A-18F Super Hornet is refueled by a KC-135R Stratotanker using a boom-drogue adapter. (U.S. Air Force photo by Senior Airman Joshua Strang)

can refuel any Navy, Air Force, or Marine aircraft has obvious strategic value, so there has been great interest in developing such an aircraft for the United States military. Originally, some models of the boom-equipped KC-135 Stratotanker were modified to accommodate a drogue adapter, enabling them to refuel Navy airplanes such as the F/A-18 shown in Fig. 4. This fix is not ideal, however, because the conversion must be made on the ground and afterward the tanker can only refuel probe-equipped fighters. This problem was solved by Boeing when it designed the replacement for the KC-135, the KC-10 Extender. The KC-10 comes equipped with both a boom and refueling drogue so that it can refuel any airplane in the US military fleet [4, 3].

The flexibility of the refueling hose allows for safer docking without the need for an operator in the tanker, opening the door to completely unmanned refueling

operations, where both the tanker and receiver are uninhabited. In addition, it is expected that the probe and drogue refueling method will better suit small agile UAVs. For these reasons this research will only consider autonomous probe and drogue refueling.

B. Modeling

Probe and drogue air refueling involves an inherently complex dynamic system, consisting of the tanker, hose, drogue, receiver, and the aerodynamic interactions between them. In addition to these component sub-systems, sensor noise and disturbances such as gusts and atmospheric turbulence play a significant role in the performance of the overall system. Although a comprehensive system model may not be practical for control synthesis or simulation purposes, it is important to note the limitations of a simplified model. This section will review work in the literature that has been done in modeling various aspects of probe and drogue refueling.

Some of the earliest pertinent literature for aerial refueling involves the modeling of the receiver aircraft. Many probe and drogue refueling operations involve a large tanker aircraft and a relatively smaller, more agile receiver aircraft [3]. In such cases the larger tanker produces a significant trailing vortex wake which influences the translational and rotational velocity of the receiver. For example, an induced rolling moment is created as the receiver is displaced sideways from the centerline of the tanker because one wing experiences more downwash than the other [6]. [6] and [7] demonstrate the importance of including the effects of the tanker wake in the receiver model; however it is unclear whether these effects will be significant when the tanker and receiver are of similar size. Further aerodynamic analysis is needed for cases where a UAV refuels another UAV.

Fig. 5. Two F/A-18 aircraft involved in NASA Dryden's Automated Aerial Refueling project fly over the California desert. (NASA photo by Carla Thomas)

Other important work on air refueling has focused on modeling the dynamics of the refueling hose and drogue. It has been found that the forebody flowfield of the receiver aircraft strongly influences the local flowfield around the drogue. This effect is different for each type of receiver aircraft. In 2003 Hansen *et al.* performed a series of 23 flight tests involving two F/A-18 aircraft and a conventional hose and drogue refueling store at NASA Dryden Flight Research Center (Fig. 5). The data collected was used to develop a parametric model to predict the drogue position based on several independent variables, including flight condition, drogue type, hose condition (empty or full), and the types of tanker and receiver. Using a video imaging system, they were able to define the area of influence (AOI), or the area where the nose of the receiver has a measurable effect on the drogue position, for several flight conditions and closing speeds [8].

Hose dynamic instabilities are another important aspect of hose and drogue modeling. Vassberg *et al.* investigated the effects of malfunctions in the reel take-up

system of a KC-10 hose and drogue refueling system [9]. The reel take-up is used to maintain adequate tension in the refueling hose during probe and drogue refueling. In this work the hose was numerically modeled as a chain of discrete elements in a flowfield defined by a linear panel method. It was found that among other factors, closure rates greater than 10 ft/sec resulted in dramatic hose oscillations and "whipping" of the drogue. These results show the need to ensure proper closing rates in both manned and autonomous refueling operations.

In addition to the physical systems, the refueling mission has also been modeled. Venkataramanan and Dogan divided the mission into four phases: approach, docking/capture, station-keeping, and fly-away [10]. Different modeling considerations come into play for each phase. During the station-keeping phase, for example, the transfer of fuel causes the mass and inertia of the receiver to change significantly. Venkataramanan and Dogan created an extensive model of the receiver aircraft that accounts for the effects of the tanker's wake, atmospheric turbulence, and changes in the mass, center of mass, and inertia matrix throughout the phases of refueling.

C. Autonomous Aerial Refueling

This section will outline previous work on autonomous probe and drogue aerial refueling. Docking the probe with the drogue is essentially a tracking task, performed by the pilot in manned refueling and the receiver's flight control system in unmanned refueling. An AAR flight control system must have adequate measurements of the position of the drogue from a sensor, and be able to relate them to commands to the aircraft through a set of control laws. Section 1 presents several sensors that have been proposed for AAR, and a survey of AAR control schemes is presented in Section 2.

1. Sensors

The ability of any controller to track and dock with a moving drogue in turbulence is conditional upon precise measurements at a rate fast enough to adequately capture the drogue dynamic behavior. This section presents several instruments and methods for relative navigation which have been proposed for autonomous aerial refueling. These include a form of GPS, passive vision sensors, active vision sensors, and combinations of sensors using estimation methods. Each system has advantages and disadvantages for in flight refueling that will be discussed.

The Differential Global Positioning System, or DGPS, is an existing technology capable of fulfilling requirements for many relative navigation applications. DGPS works by using reference stations on the ground to provide a correction to signals from GPS satellites. It is generally more accurate than GPS alone, with a typical position error of one to three meters [11]. Errors in the vertical direction (altitude) are usually larger than those in latitude and longitude. Most commercially available DGPS receivers provide an updated navigation solution at a rate of once per second (1 Hz), although some sources claim up to 10 Hz [12, 13]. DGPS can operate at great distances, giving it an advantage over vision-based sensors. Disadvantages of DGPS include problems with multipath effects, satellite drop-out, geometric dilution of precision, integer ambiguity resolution, and cycle slip [14].

If DGPS is used for the final docking phase of refueling, the only way to capture the drogue movement would be to install the antenna directly on to the refueling drogue. [8] notes that this situation poses many integration and safety problems. In addition, the tanker wing, empennage, or receiver aircraft may block signals from the GPS satellites. Finally, the accuracy and update rate required for proximity navigation, especially for small UAVs in turbulence, are beyond the capabilities of existing

DGPS hardware. For these reasons, several researchers have proposed combining DGPS with vision-based sensors for air refueling [13, 12, 15]. DGPS offers accuracy at long range, while vision sensors can provide more precise measurements during the final docking phase.

The engineering community has long studied the concept of machine vision for a wide range of applications, from manufacturing techniques to formation flying. The idea of using machine vision for navigation of unmanned vehicles has become very popular in the last decade. Vision sensors have been proposed for many aspects of UAV operation, including navigation, terrain avoidance, and landing [16, 17].

Most vision sensors work by processing 2D images from one or more cameras. To determine 3D information from 2D images, some sort of mapping is required. This involves relating some key markers, such as light beacons or patterned decals, in an image to their known positions on the target. At this point a distinction should be made between active and passive vision systems. A passive system does not require the cooperation of the target in any way, and can therefore be used for applications such as obstacle avoidance and detection. The difficulty with passive systems comes from distinguishing key points in the 2D image. Often significant computational burden is incurred to discern the identifying markers from background clutter under varying lighting conditions. In contrast, active systems communicate and coordinate with the target in some way, making the identification process much easier.

Pollini *et al.* proposed a passive vision sensor for AAR which processes images of infrared (IR) light-emitting diodes (LEDs) mounted to the drogue [18, 19]. The LEDs are mounted in a co-planar configuration, at the vertices of a regular polygon. Images taken with an IR camera mounted on the receiver vehicle are passed to a modified version of the estimation algorithm created by Lu, Hager and Mjolsness (LHM). The LHM algorithm determines the relative position and attitude based on minimizing the

object space collinearity error. The symmetry of the beacon configuration eliminates the need for uniquely identifiable markers. However, this leads to the relative roll angle becoming unobservable. The estimation algorithm is shown to converge within ten iterations in simulation and experiment, but no mention is made of the update rate, which is critical for refueling in turbulence.

Although recent advances in micro processors have made pattern recognition software a viable technology for many navigation applications, the update rate is still too slow to track a refueling drogue in light turbulence. In addition, many small UAVs may be unable to accommodate the weight and power requirements for image processing hardware. Because AAR involves two cooperating (friendly) vehicles, an active system offers significant advantages over a passive sensor.

VisNav is an active vision-based sensor developed by Junkins, Schaub, and Hughes at Texas A&M University [20]. Its ability to generate highly accurate measurements with an update rate of up to 100 Hz makes it an ideal sensor for autonomous refueling operations. VisNav is capable of producing six degree-of-freedom relative navigation information without the need for a computationally intensive image processing system [2]. The VisNav system is primarily composed of a set of structured light beacons and a sensor box. The VisNav sensor is mounted to the receiver aircraft and the beacons are attached to the refueling drogue, similar to Pollini's sensor [18]. However, instead of a camera, VisNav calculates line of sight vectors to each beacon using voltage measurements from a light sensitive diode. A controller on the receiver orchestrates the sequence and timing of the active beacon array through a wireless data link. This assures correspondence between each measurement and the known position of the beacon on the target, eliminating the marker identification problem. VisNav sensor is described in detail in Chapter III.

One of the drawbacks of an active sensor is that it may be susceptible to inter-

ception or jamming in hostile environments. Because the sensor is active only at close range, however, a relatively weak IR or radio signal may be employed to communicate with the beacons. Aerial refueling operations typically occur at high altitude, making such a signal difficult to detect from the ground.

For autonomous operations such as formation flying and air refueling, both long range and proximity measurements are needed at various phases during the mission. For AAR, the receiver aircraft must first find the tanker and get within range of the vision sensor. During the final phase of docking, very accurate, high frequency relative measurements are needed. The receiver may be equipped with an inertial measurement unit (IMU), GPS or DGPS receiver, air data probes, and a vision sensor of some kind. One way to take advantage of all of the available information is to the fuse measurements from these instruments.

In 2002 Williamson *et al.* proposed an instrument that uses a combination of GPS and and INS (inertial navigation system) called the Formation Flight Instrumentation System (FFIS). Measurements from Differential Carrier Phase GPS and an onboard INS are transmitted via wireless data links between aircraft flying in formation. An extended Kalman filter (EKF) is used to blend the measurements from each aircraft to provide estimates of relative position, velocity, and attitude. The authors developed a method to resolve integer ambiguity from DGPS measurements, however this algorithm has not been proven to converge in all situations. The state estimates are available to the control system at a rate of 40 Hz. Early flight test results showed fairly accurate position estimates with a mean error of 7 cm and a standard deviation of 13 cm. The attitude estimates, however, were poor due to larger than expected noise in the IMU during flight testing [21].

More recently Awalt *et al.* developed a Multi-Model Adaptive extended Kalman filter (MM EKF) to combine data from several sources for autonomous formation

flight [15]. The MM EKF fuses transmitted state information from the wingman (the lead vehicle), GPS/INS measurements, an unspecified vision sensor, and a choice of several *a priori* models of the wingman and its control laws. The MM EKF then provides the ownship (the follower) with an optimal estimate of the wingman state for its guidance laws. The adaptive component of the EKF allows the system to be robust to modeling errors due to turbulence effects, erroneous communication data, noisy vision sensor data, and rate gyro failure. The price for increased robustness, however, is a decrease in overall tracking performance. The MM EKF was demonstrated through nonlinear simulation using simple vehicle dynamics, but the system has yet to be tested in flight [15].

Table I summarizes the sensors and instruments discussed in this section. The advantages and disadvantages for the autonomous aerial refueling application are briefly listed for each system.

2. Control

Autonomous aerial refueling is a relatively nascent area of research; most of the previous work has been done within the past three years. Several approaches to the control aspects of AAR have been investigated in combination with the various sensor systems discussed in Section 1. Controllers have been developed for both probe and drogue and boom refueling methods, although the requirements for these two methods of refueling are quite different. The primary task of the receiver during boom refueling is to maintain a constant relative position to the tanker. [22] discusses a design for automatic boom refueling. Probe and drogue refueling requires the receiver to track and maneuver to the refueling drogue, a much more demanding control problem. This section will discuss controllers which have been developed for the probe and drogue refueling task.

Table I. Summary of navigation systems for autonomous aerial refueling

SYSTEM	ADVANTAGES	DISADVANTAGES
DGPS [11]	Long range measurements Existing technology	Low update rate (10 Hz max) Low accuracy (1 m) Reliability issues Installation on drogue difficult Susceptible to jamming
Pattern Recognition [18]	Not susceptible to jamming	Low update rate Weight and power requirements Sensitive to visibility conditions
VisNav [2]	High accuracy (about 3 cm) High update rate (100 Hz) Low weight, size and power	May be susceptible to jamming Sensitive to visibility conditions Has not been flight tested
FFIS [21]	Commercially available hardware Moderate update rate (40 Hz)	Accuracy about 20 cm Susceptible to jamming Reliability issues
MM EKF [15]	Robust to sensor failure High accuracy High update rate	Susceptible to jamming Has not been flight tested

Some of the first work in AAR was a result of the development of applications for the VisNav sensor at Texas A&M University. Valasek, Kimmett, Hughes, Gunnam, and Junkins first proposed a system for AAR using the VisNav sensor and the Nonzero Set Point (NZSP) control structure [23]. This work considered the case where the refueling drogue is stationary relative to the steady-state flight path of the receiver vehicle. NZSP is an optimal time-domain tracking control structure which assumes full-state feedback. A general block diagram is shown in Fig. 6.

The objective of the NZSP controller design is to find the optimal gain K, and the matrices X_{12} and X_{22} such that the actual output $\mathbf{y}$ tracks the desired output $\mathbf{y}_m$. Perfect tracking can be achieved when $\mathbf{y}_m$ is a known constant value. For air refueling, the desired output is the inertial position that the receiver aircraft must

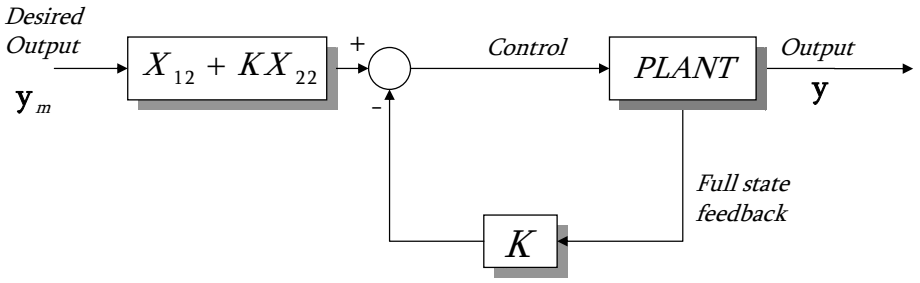

Fig. 6. Nonzero Set Point (NZSP) control structure

achieve in order for it to dock with the drogue. In some cases the heading angle may be commanded as well, but it is not required. The authors modified the control structure by adding a proportional integral filter (PIF) and control rate weighting (CRW) in order to avoid control saturation, resulting in the PIF-NZSP-CRW controller. In a subsequent publication, Kimmett, Valasek, and Junkins added a variational Kalman filter (VKF) to estimate full state feedback [24, 25]. This control/estimation structure, also known as a linear quadratic Gaussian (LQG) system, provides estimates of the states which are not measured and filters exogenous inputs and measurement noise.

Kimmett, Valasek and Junkins then extended this work for cases where the drogue position is no longer constant by using a command generator tracker (CGT) controller [26]. CGT (Fig. 7) is a model-following control structure which is similar to NZSP, but instead of tracking a constant value, CGT can track a time-varying reference trajectory that is generated with an *a priori* model. For perfect tracking the input to the model must be constant, otherwise the controller will lag the reference signal. The most challenging aspect of designing the CGT controller is the selection of the reference model. For aerial refueling Kimmett *et al.* [26] proposed a dynamic model of the drogue as the reference model system. The authors were able to show successful docking with the moving drogue in still air, however performance

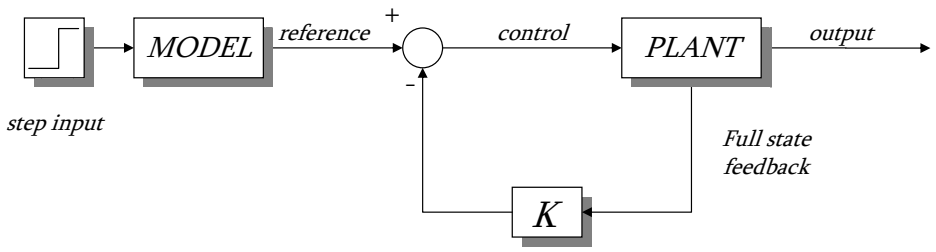

Fig. 7. Command Generator Tracker (CGT) control structure

was degraded in the presence of light atmospheric turbulence. This was mainly due to the fact that there is no direct correspondence in the controller between the *model* drogue and the *actual* drogue. Specifically, when the actual drogue experienced turbulence the controller tracked the model of the drogue in still air, leading to degraded performance.

The main limitation with applying a model-following controller such as CGT to air refueling is that the trajectory of the drogue must be known *a priori*. In practice, the desired or reference states need to be estimated based on the measured aircraft states and the estimated relative position and orientation of the drogue. In [27] Tandale, Bowers, and Valasek solved this problem by modifying the Nonzero Set Point control structure so that it does not require a drogue model or presumed knowledge of its position. The modified control structure is called the Reference Observer-based Tracking Controller (ROTC). Relative measurements from the VisNav sensor are fed forward into an estimator, which determines what the receiver states and controls need to be in order to track the drogue. A trajectory generation module creates a feasible trajectory for the receiver to follow to achieve successful docking. The trajectory tracking controller has been shown to be robust to errors in the model and disturbances due to turbulence. Additionally, this work considered cases where the navigation solution from VisNav is affected by factors such as the loss of one or more

beacons as they fall outside of the field of view. This thesis will use the ROTC to examine the closed-loop performance of an autonomous aerial refueling system. The control structure is discussed in detail in Chapter V.

Campa *et al.* [13] and Fraviolini *et al.* [12] proposed a robust H_∞ controller which tracks a reference signal from a fuzzy fusion of measurements from GPS and an unspecified artificial vision sensor. They included a finite element model of a flexible "boom-drogue" in Dryden moderate turbulence. Accurate tracking performance was demonstrated using nonlinear simulation, however, the resulting 24^{th} order controller may be difficult to implement in practice.

Stepanyan *et al.* considered the problem of autonomous air refueling autopilot design using techniques from differential games and adaptive control [28]. The performance of this controller was demonstrated in simulation assuming the availability of ideal measurements of the drogue position, i.e. no sensor model was incorporated in the design. Bounded random inputs to the drogue dynamic model were considered, but turbulence effects were not modeled explicitly.

CHAPTER III

THE VISNAV SYSTEM

The VisNav sensing system measures the relative position and orientation between two vehicles or objects. It works by measuring the line of sight (LOS) vectors between the sensor, which is mounted on one vehicle, and a set of structured light beacons attached to the second vehicle. Once LOS measurements from several beacons have been collected, VisNav uses an estimation algorithm to determine relative position and attitude. This chapter will describe some important aspects of the VisNav system and how it works. The interested reader should consult [2] and [14] for further details.

A. System Description

This section will give a brief description of some of the major components of VisNav. It is not intended to be a comprehensive description of VisNav hardware, rather, an introduction to the basic parts and their functions. Fig. 8 shows a schematic of the VisNav System architecture. The main components discussed here are the sensor, beacon controller, and beacon array. [2] contains a more detailed description of VisNav hardware.

The sensor part of the system (Fig. 9) contains a photodiode or position sensing diode (PSD), a wide angle lens, and a digital signal processor (DSP). For this research, it is assumed that the sensor components are located on the receiver aircraft. While this configuration is not required, it was chosen because the AAR controller, which uses VisNav measurements, is assumed to be on board the receiver vehicle. This avoids having to transmit the navigation solution from one vehicle to the other, which introduces latency and degrades controller performance.

It is important for the estimation algorithm to associate each LOS measurement

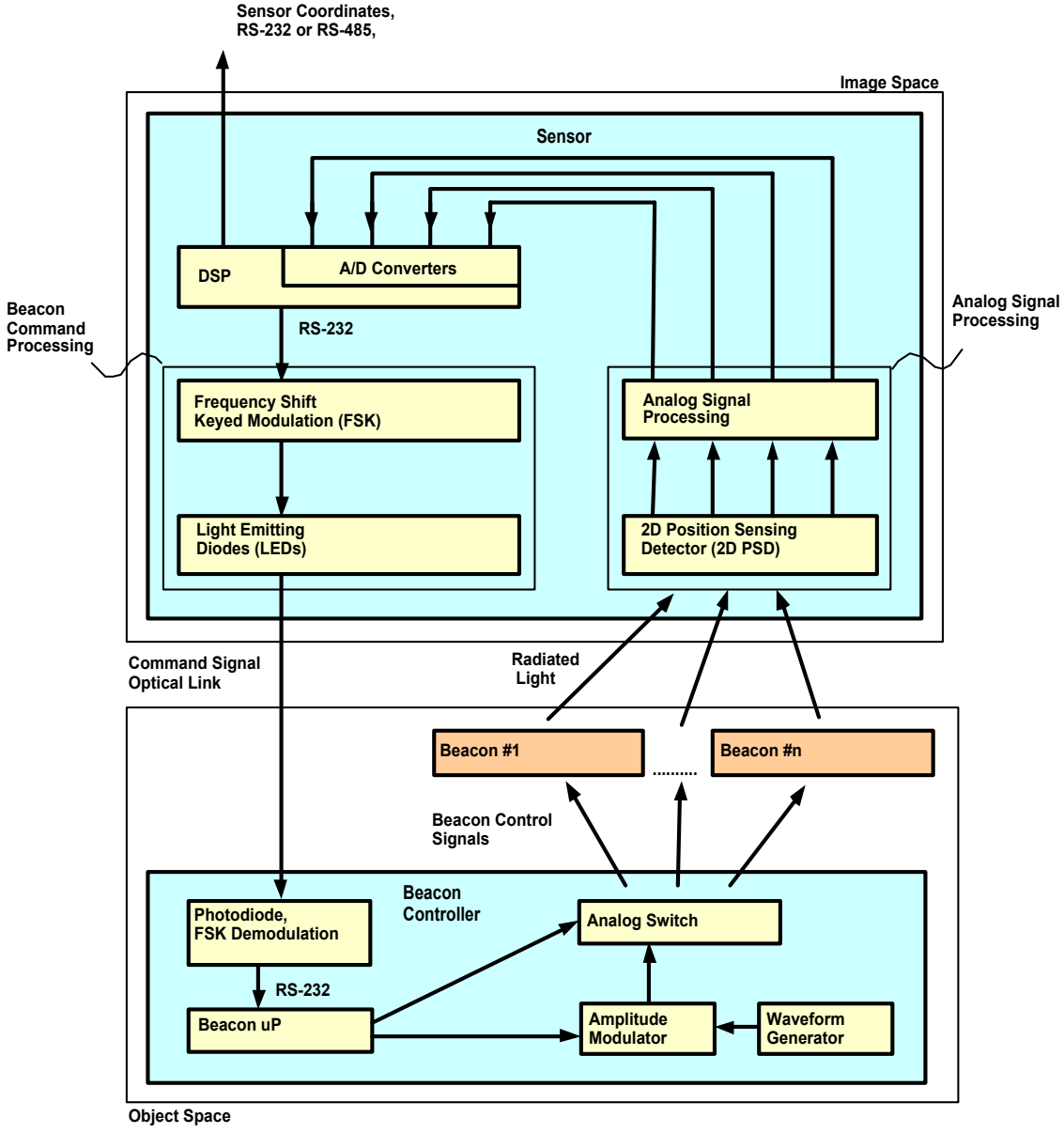

Fig. 8. VisNav system architecture (Reprinted with permission from "Vision-Based Sensor and Navigation System for Autonomous Air Refueling" by J. Valasek, K. Gunnam, J. Kimmett, M. Tandale, J.L. Junkins and D. Hughes, 2005. *Journal of Guidance, Control, and Dynamics* (accepted)).

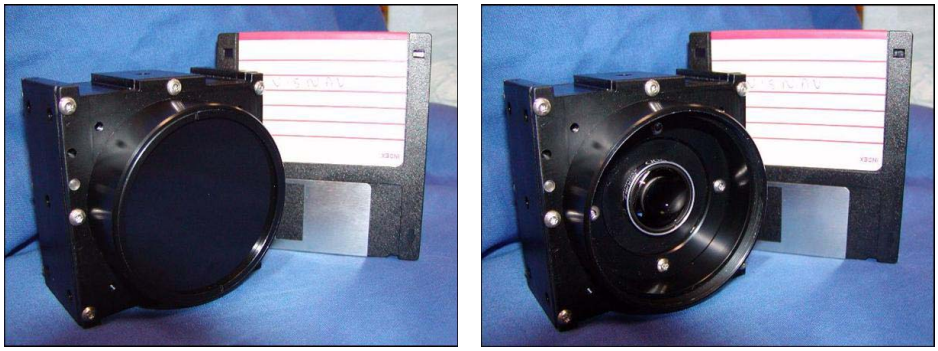

Fig. 9. The VisNav sensor

with the specific beacon which produced it. The beacon controller orchestrates the sequence and timing of the beacons' activation through an infrared or radio data link. Feedback from the controller is used to hold the beacon light intensity at about 70% of the saturation level of the PSD, preventing damage to the photodiode and maintaing an optimal signal-to-noise ratio throughout operation [2].

When VisNav is operating, the DSP commands the the beacon controller to signal each beacon to activate in turn. As each beacon turns on, light comes through the wide angle lens and is focused onto the PSD. The focused light creates a centroid, or spot, on the photodiode, which causes a current imbalance in the four terminals on each side of the PSD. The closer the light centroid is to one side of the photodiode, the higher the current in the nearest terminal (see Fig. 10). By measuring the voltage at each terminal, the 2-D position of the light centroid on the PSD can be found with a nonlinear calibration function, which is determined experimentally for each sensor[2].

For AAR the active beacon array is located on the refueling drogue and/or the tanker aircraft. Each beacon is made of a cluster of infrared light emitting diodes. The beacons currently come in three sizes, as shown in Fig. 11. Although only four

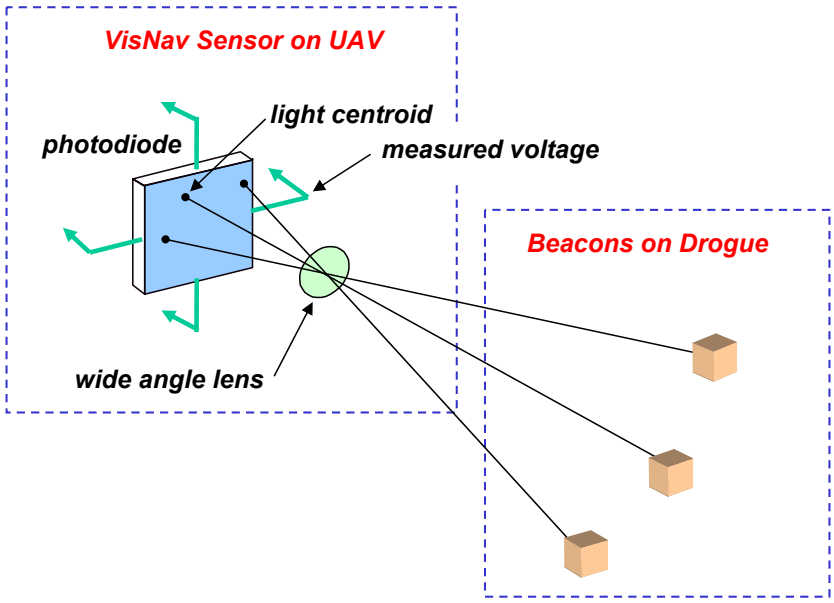

Fig. 10. Illustration of VisNav operation

beacons are required to obtain a unique six degree-of-freedom navigation solution, a configuration of eight beacons has been shown to give good results for AAR [29]. The extra beacons provide redundancy in case a beacon falls outside of the field of view, and additional measurements improve the convergence performance of the estimation routine.

The configuration of the beacons on the target vehicle is an important parameter which affects VisNav's ability to obtain a solution accurately and quickly. At long range, it is desirable to have a large beacon array, however at close range these beacons may fall outside the field of view. Thus a second, smaller beacon array may be used for proximity navigation. [2] states that a desirable configuration would ensure that the lateral extent of the beacon array takes up at least 10% of the sensor field of view within the range of interest.

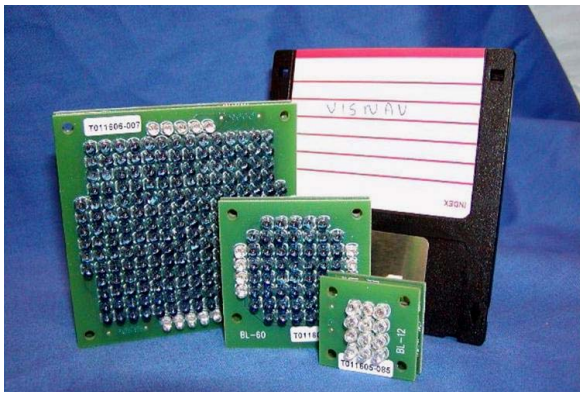

Fig. 11. VisNav active beacons in three sizes

B. Measurement Model

The measurement model used by VisNav is based on the collinearity equations. These equations assume that the beacon, the center of the lens, and the light centroid on the PSD lie along the same line (see Fig. 12). This is sometimes referred to as the ideal pin-hole model because it does not take into account distortions due to the lens and the PSD detector. These departures from the ideal case are accounted for in the calibration process [2].

In Fig. 12 there are two coordinate frames of interest. The first is image space, a body-fixed coordinate frame attached to the sensor with origin at the center of the lens. The focal length f lies along the image space x-axis, and the y-z plane is aligned with the surface of the PSD. The second frame, object space, is fixed to the target vehicle. The mounting location for beacon i on the target vehicle is known, thus the beacon's position in the object space frame, $\mathbf{B}_i$, is known. The objective is now to develop equations for the measured quantities y_i and z_i in terms of the unknown sensor position in the object space, $\mathbf{o}$, and the transformation between image space and object space, C.

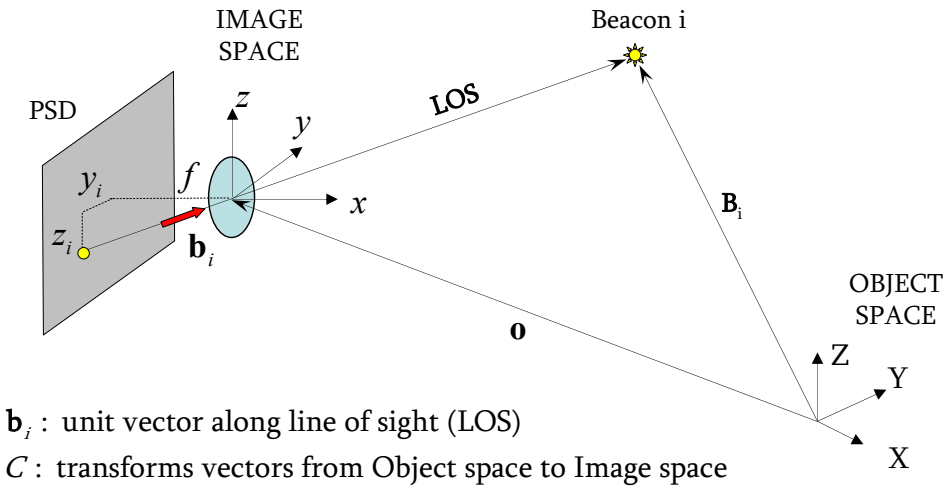

Fig. 12. Ideal pin-hole model for VisNav sensor

The unknown coordinates of the sensor in object space are defined as

$$\mathbf{o} = \begin{bmatrix} X_c \\ Y_c \\ Z_c \end{bmatrix} \tag{3.1}$$

and the known location of the i^{th} beacon in object space is defined as

$$\mathbf{B}_i = \begin{bmatrix} X_i \\ Y_i \\ Z_i \end{bmatrix} \tag{3.2}$$

The unknown direction cosine matrix which transforms object space to image space, C, will be parameterized with the Modified Rodrigues Parameters, or MRPs. MRPs are a set of three attitude parameters which can be related to the Euler parameters. In terms of the principal rotation vector, $\mathbf{e}$, and the principal rotation angle Φ, the

MRP (3×1) vector $\mathbf{p}$ is defined as

$$\mathbf{p} = \tan \frac{\Phi}{4} \mathbf{e} \tag{3.3}$$

A detailed explanation of attitude parameters may be found in [30]. The direction cosine matrix in terms of $\mathbf{p}$ is

$$C = I + \frac{8 \left[\mathbf{p}\times\right]^2 - 4 \left(1 - \mathbf{p}^T\mathbf{p}\right) \left[\mathbf{p}\times\right]}{\left(1 + \mathbf{p}^T\mathbf{p}\right)^2} \tag{3.4}$$

where

$$\left[\mathbf{p}\times\right] = \begin{bmatrix} 0 & -p_3 & p_2 \\ p_3 & 0 & -p_1 \\ -p_2 & p_1 & 0 \end{bmatrix}$$

The unit LOS vector to beacon i in image space coordinates is

$$\mathbf{b}_i = \frac{1}{\sqrt{f^2 + y_i^2 + z_i^2}} \begin{bmatrix} f \\ -y_i \\ -z_i \end{bmatrix} \tag{3.5}$$

The unit LOS vector to beacon i in object space coordinates is

$$\mathbf{r}_i = \frac{1}{\sqrt{(X_i - X_c)^2 + (Y_i - Y_c)^2 + (Z_i - Z_c)^2}} \begin{bmatrix} (X_i - X_c) \\ (Y_i - Y_c) \\ (Z_i - Z_c) \end{bmatrix} \tag{3.6}$$

Thus the unit vector form of the collinearity equations may be written as

$$\mathbf{b}_i = C\mathbf{r}_i \tag{3.7}$$

Solving for the measured image space coordinates gives

$$y_i = -f\frac{C_{21}(X_i - X_c) + C_{22}(Y_i - Y_c) + C_{23}(Z_i - Z_c)}{C_{11}(X_i - X_c) + C_{12}(Y_i - Y_c) + C_{13}(Z_i - Z_c)} \tag{3.8}$$

$$z_i = -f\frac{C_{31}(X_i - X_c) + C_{32}(Y_i - Y_c) + C_{33}(Z_i - Z_c)}{C_{11}(X_i - X_c) + C_{12}(Y_i - Y_c) + C_{13}(Z_i - Z_c)} \tag{3.9}$$

The collinearity equations represent the nonlinear relationship between the measured image space coordinates, y_i and z_i, and the six unknowns, X_c, Y_c, Z_c, p_1, p_2, and p_3. Measurements from each beacon contribute two equations, therefore at least three beacons are needed to obtain a solution. Some configurations of three beacons, however, can give more than one viable solution. At least four measurements are needed to find a unique solution, causing the problem to be overdetermined, with more equations than unknowns. The overdetermined problem is solved using the linear least squares method described in the next section.

C. Gaussian Least Squares Differential Correction Algorithm

Once measurements of the image space coordinates of at least four beacons are collected, the information is processed by a digital signal processor, or DSP. Inside the DSP, a Gaussian Least Squares Differential Correction (GLSDC) algorithm is used to estimate the position and attitude of the sensor relative to the beacons. The idea behind GLSDC is to determine some unknown parameters, such as relative position and attitude, given 1) a measurement model and 2) a set of measured data. These two are combined to produce an estimate of the unknown parameters which is optimal with respect to a specified amount of measurement noise [31].

To begin, a state vector consisting of the unknown parameters to be estimated is defined. In the case of VisNav, these are the relative position, $\mathbf{o}$, and relative attitude,

$\mathbf{p}$, as defined in (3.1) and (3.3).

$$\mathbf{x} = \begin{bmatrix} \mathbf{p} \\ \mathbf{o} \end{bmatrix} \tag{3.10}$$

It is assumed that a set of measurements from n beacons has been collected, where $n \geq 4$,

$$\tilde{\mathbf{b}} = \begin{bmatrix} \tilde{\mathbf{b}}_1 \\ \tilde{\mathbf{b}}_2 \\ \vdots \\ \tilde{\mathbf{b}}_n \end{bmatrix} \tag{3.11}$$

The measurement model for the i^{th} beacon derived in Section B is

$$\mathbf{b}_i = C\mathbf{r}_i = \mathbf{h}_i(\mathbf{x}) \tag{3.12}$$

When measurement noise ν_i is present, the model becomes

$$\tilde{\mathbf{b}}_i = \mathbf{h}_i(\mathbf{x}) + \nu_i \tag{3.13}$$

The measurement noise is assumed to have a Gaussian distribution with zero mean and covariance $R_i = E\{\nu_i \nu_i^T\}^*$. The measurement error covariance matrix for the set of n measurements is thus

$$R = \begin{bmatrix} R_1 & 0 & 0 & 0 \\ 0 & R_2 & 0 & 0 \\ 0 & 0 & \ddots & 0 \\ 0 & 0 & 0 & R_n \end{bmatrix} \tag{3.14}$$

---

*E represents the expectation operator. The expected value of a function $f(x)$ of a discrete random variable x is defined as $E\{f(x)\} = \sum_j f(x(j))p(x(j))$, where $p(x(j))$ is the probability of occurrence of $x(j)$.

It is desired to find an estimate $\hat{\mathbf{x}}$ which minimizes the residual error

$$\Delta\mathbf{b} = \begin{bmatrix} \tilde{\mathbf{b}}_1 - \mathbf{h}_1(\hat{\mathbf{x}}) \\ \tilde{\mathbf{b}}_2 - \mathbf{h}_2(\hat{\mathbf{x}}) \\ \vdots \\ \tilde{\mathbf{b}}_n - \mathbf{h}_n(\hat{\mathbf{x}}) \end{bmatrix} \tag{3.15}$$

To do this a cost function J is defined as the weighted sum of squares of the residual error

$$J = \frac{1}{2}\Delta\mathbf{b}^T W \Delta\mathbf{b} \tag{3.16}$$

where W is a matrix of weighting parameters. For a maximum likelihood estimate, the weights are chosen as the reciprocal of the measurement error covariance matrix, $W = R^{-1}$. The minimum cost is found by setting the derivative of J with respect to $\hat{\mathbf{x}}$ to zero and solving for the estimated state. Because $\mathbf{h}$ is a nonlinear function of $\hat{\mathbf{x}}$, however, an explicit solution for the estimate cannot be found. Instead, an iterative approach may be used under the assumption that a current estimate, $\mathbf{x}_c$, is available. The estimate is thus defined as the current value plus a differential correction:

$$\hat{\mathbf{x}} = \mathbf{x}_c + \Delta\mathbf{x} \tag{3.17}$$

Assuming that $\Delta\mathbf{x}$ is small, the nonlinear measurement model may be linearized about the current estimate:

$$\mathbf{h}(\hat{\mathbf{x}}) \approx \mathbf{h}(\mathbf{x}_c) + \bar{H}\Delta\mathbf{x} \tag{3.18}$$

where $\bar{H}$ is the $(3n \times 6)$ measurement sensitivity matrix evaluated at the current

estimate. $\bar{H}$ is found by differentiating the measurement model with respect to $\mathbf{x}$:

$$\bar{H} = \begin{bmatrix} \bar{H}_1 \\ \bar{H}_2 \\ \vdots \\ \bar{H}_n \end{bmatrix}, \; \bar{H}_i = \frac{\partial \mathbf{h}_i}{\partial \mathbf{x}} = \left[\frac{\partial \mathbf{h_i}}{\partial \mathbf{p}} : \frac{\partial \mathbf{h_i}}{\partial \mathbf{o}} \right] \tag{3.19}$$

where

$$\begin{aligned} \frac{\partial \mathbf{h_i}}{\partial \mathbf{p}} &= \frac{4}{\left(1 + \mathbf{p}^T\mathbf{p}\right)^2} \left[C\mathbf{r}_i\times\right] \left\{ \left(1 - \mathbf{p}^T\mathbf{p}\right) I_{3\times 3} - 2\left[\mathbf{p}\times\right] + 2\mathbf{p}\mathbf{p}^T \right\} \\ \frac{\partial \mathbf{h_i}}{\partial \mathbf{o}} &= -C\left\{ I_{3\times 3} - \mathbf{r}_i\mathbf{r}_i^T \right\} / \sqrt{(X_i - X_c)^2 + (Y_i - Y_c)^2 + (Z_i - Z_c)^2} \end{aligned} \tag{3.20}$$

Let $\Delta\mathbf{b}_c$ represent the residual error for the current estimate (before the correction):

$$\Delta\mathbf{b}_c \equiv \tilde{\mathbf{b}} - \mathbf{h}(\mathbf{x}_c) \tag{3.21}$$

The residual error may now be approximated as

$$\Delta\mathbf{b} \approx \tilde{\mathbf{b}} - \mathbf{h}(\mathbf{x}_c) - \bar{H}\Delta\mathbf{x} = \Delta\mathbf{b}_c - \bar{H}\Delta\mathbf{x} \tag{3.22}$$

and the cost function in terms of the linearly predicted residuals becomes

$$J_p = \frac{1}{2}\left(\Delta\mathbf{b}_c - \bar{H}\Delta\mathbf{x}\right)^T W \left(\Delta\mathbf{b}_c - \bar{H}\Delta\mathbf{x}\right) \tag{3.23}$$

To minimize (3.23), the following necessary and sufficient conditions must be satisfied:

$$\textit{Necessary:} \quad \nabla_{\Delta\mathbf{x}} J = \bar{H}^T W \bar{H}\Delta\mathbf{x} - \bar{H}^T W \tilde{\mathbf{b}}_c = 0 \tag{3.24}$$

$$\textit{Sufficient:} \quad \nabla^2_{\Delta\mathbf{x}} J = \bar{H}^T W \bar{H} > 0 \tag{3.25}$$

Solving (3.24) for the differential correction gives

$$\Delta\mathbf{x} = (\bar{H}^T W \bar{H})^{-1} \bar{H}^T W \Delta\mathbf{b}_c \tag{3.26}$$

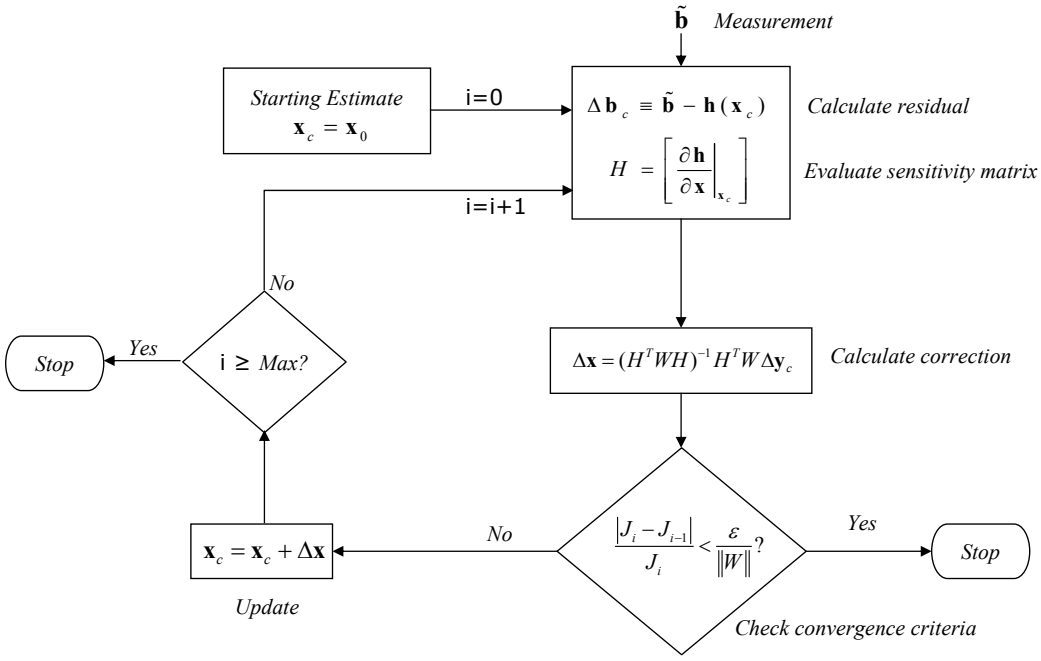

Fig. 13. Gaussian Least Squares Differential Correction (GSLDC) algorithm

The quantity $(\bar{H}^T W \bar{H})^{-1}$ is generally referred to as the estimation error covariance matrix. A large error covariance matrix is an indication that the solution has not converged to an acceptable value. Once the correction is calculated from (3.26), the estimate is updated and the process begins again until some stopping criteria is reached. One stopping condition given in [31] consists of evaluating the change in the cost function between iterations:

$$\frac{|J_i - J_{i-1}|}{J_i} < \frac{\epsilon}{\|W\|} \tag{3.27}$$

where ϵ is a prescribed small value. Other stopping conditions may include similar evaluations of the change in the residual or the differential correction between iterations. A flowchart for GLSDC is shown in Fig. 13.

CHAPTER IV

VISNAV KALMAN FILTER

The VisNav sensor provides a six degree-of-freedom navigation solution consisting of the relative position and attitude between two vehicles or bodies. This chapter will define how the measurements from VisNav may be passed into a linear Kalman filter to improve the navigation solution and obtain additional estimates of relative velocity and acceleration. Section A develops the theory behind the discrete-time linear Kalman filter. Section B discusses how the theory is applied to the relative navigation problem using measurements from VisNav. Finally, Section C details the process of tuning the Kalman filter for the air refueling application.

A. Discrete-Time Linear Kalman Filter

One purpose of an estimator is to obtain estimates of the states of a dynamic system, given a model of the system and the known inputs and measured outputs over some time interval. The Kalman filter is a specific type of estimation process in which the poles of the estimator are placed based upon assumed stochastic properties of the measurement error and model error. This section closely follows the development and uses the notation of the discrete-time linear Kalman filter in [31].

To begin, a discrete linear model of the dynamic system of interest is specified as

$$\mathbf{x}_{k+1} = \Phi_k \mathbf{x}_k + \Gamma_k \mathbf{u}_k + \Upsilon_k \mathbf{w}_k \tag{4.1}$$

where $\mathbf{x}_k \in \Re^n$ is the state vector, $\mathbf{u}_k \in \Re^m$ is the control vector, and $\mathbf{w}_k \in \Re^p$ is the vector of process noise, all at time step k. The process noise represents an unknown forcing input to the system, such as a disturbance or unmodeled dynamics. The state

transition matrix, Φ_k, control distribution matrix, Γ_k, and disturbance matrix, Υ_k, are real matrices of appropriate dimensions. The discrete measurement equation is defined as

$$\tilde{\mathbf{y}}_k = H_k \mathbf{x}_k + \mathbf{v}_k \tag{4.2}$$

where $\mathbf{y}_k \in \Re^r$ represents the measured output at time step k, and $\mathbf{v}_k$ represents the measurement noise. It is assumed that both the process noise $\mathbf{w}_k$ and the measurement noise $\mathbf{v}_k$ are zero-mean Gaussian† white-noise processes, where

$$E\left\{\mathbf{v}_k \mathbf{v}_j^T\right\} = \begin{cases} 0, & k \neq j \\ R_k, & k = j \end{cases} \tag{4.3}$$

and

$$E\left\{\mathbf{w}_k \mathbf{w}_j^T\right\} = \begin{cases} 0, & k \neq j \\ Q_k, & k = j \end{cases} \tag{4.4}$$

It is further assumed that $\mathbf{w}_k$ and $\mathbf{v}_k$ are uncorrelated for all k, or $E\left\{\mathbf{v}_k \mathbf{w}_k^T\right\} = 0$.

Because the initial condition of the state, $\mathbf{x}_0$, is unknown, the estimation process must begin with an initial guess, or prediction, of the state:

$$\hat{\mathbf{x}}\left(t_0\right) = \hat{\mathbf{x}}_0 \tag{4.5}$$

After the initial time, it is the job of the estimator to update the current estimate of the state, $\hat{\mathbf{x}}_k$, and to obtain the estimate at the next time step, $\hat{\mathbf{x}}_{k+1}$, based upon the measured and predicted output at time k. The estimator works through the dual processes of *prediction* and *correction*. The current estimate is first updated (or

†The Gaussian or Normal probability density function is typically denoted by $p(\mathbf{x}) \sim N(\mu, R)$, where $p(\mathbf{x})$ is the probability of the vector $\mathbf{x}$, μ is the mean, and R is the covariance matrix.

corrected) based upon measured and predicted quantities using the update equation:

$$\hat{\mathbf{x}}_k^+ = \underbrace{\hat{\mathbf{x}}_k^-}_{\text{model prediction}} + K_k \underbrace{\left[\tilde{\mathbf{y}}_k - H_k \hat{\mathbf{x}}_k^-\right]}_{\text{residual error}} \tag{4.6}$$

where the ($\hat{}$) denotes an estimated quantity and the superscripts $-$ and $+$ denote the predicted state before and after the update. The difference between the measured output and the estimated output at time step k is referred to as the residual error. The time-varying gain, K_k, affects the updated estimate by amplifying or attenuating the effect of the residual error. A large gain means that the measurement will dominate the update, whereas a smaller gain places more emphasis on the model prediction. Once the estimate is updated with (4.6), the estimate is propagated forward in time using the model for the system and the known input at time k:

$$\hat{\mathbf{x}}_{k+1}^- = \Phi_k \hat{\mathbf{x}}_k^+ + \Gamma_k \mathbf{u}_k \tag{4.7}$$

This value is then used as the model prediction in the update equation at the next time step, and the process repeats.

The selection of K_k is what sets the Kalman filter apart from other observers which have the form given in (4.6) and (4.7). For example, Luenberger's observer determines K_k using pole placement methods to specify the eigenvalues of the estimator. Not only is this process difficult for higher-order systems, but there is no rigorous method to determine where the estimator poles should be placed. Kalman developed a theoretical approach to optimally place the poles of the estimator based on the assumed stochastic properties of the process and measurement noise. By assuming that $\mathbf{w}_k$ and $\mathbf{v}_k$ are zero-mean uncorrelated Gaussian processes, it is possible to develop an expression for K_k which minimizes the estimation error at each time step.

The estimation error, denoted with a ($\tilde{}$), is defined as the estimated state minus the true state:

$$\tilde{\mathbf{x}}_k \equiv \hat{\mathbf{x}}_k - \mathbf{x}_k \tag{4.8}$$

The key to Kalman's solution is the estimation error covariance matrix, which is defined as the expectation of the squared sum of the estimation errors

$$P_k \equiv E\left\{\tilde{\mathbf{x}}_k \tilde{\mathbf{x}}_k^T\right\} \tag{4.9}$$

Like the estimated state, it is necessary to define an initial value for the estimation error covariance at time zero

$$P_0 = E\left\{\tilde{\mathbf{x}}\left(t_0\right)\tilde{\mathbf{x}}\left(t_0\right)^T\right\} \tag{4.10}$$

Using (4.6) and (4.7) and the assumed stochastic properties of $\mathbf{w}_k$ and $\mathbf{v}_k$, it is possible to derive the following expressions for the estimation error covariance before and after the update

$$P_k^+ = \left[I - K_k H_k\right] P_k^- \tag{4.11}$$

$$P_{k+1}^- = \Phi_k P_k^+ \Phi_k^T + \Upsilon_k Q_k \Upsilon_k^T \tag{4.12}$$

The cost function for optimization can be defined as the trace of the error covariance after the update

$$J(K_k) = \mathrm{tr}(P_k^+) \tag{4.13}$$

To find the gain which minimizes the cost function, the derivative of J with respect to K_k is set to zero and solved for K_k. Using properties of the trace function, as well as the fact that P_k^- and R_k are symmetric, the following expression can be found:

$$\frac{\partial J}{\partial K_k} = -2\left(I - K_k H_k\right) P_k^- H_k^T + 2K_k R_k = 0 \tag{4.14}$$

Solving (4.14) for the gain yields

$$K_k = P_k^- H_k^T \left[H_k P_k^- H_k^T + R_k \right]^{-1} \tag{4.15}$$

A summary of the discrete-time linear Kalman filter is presented in Table II.

Table II. Discrete-time linear Kalman filter [31]

MODEL	$\mathbf{x}_{k+1} = \Phi_k \mathbf{x}_k + \Gamma_k \mathbf{u}_k + \Upsilon_k \mathbf{w}_k$ $\tilde{\mathbf{y}}_k = H_k \mathbf{x}_k + \mathbf{v}_k$
NOISE	$\mathbf{w}_k \sim N(0, Q_k)$ $\mathbf{v}_k \sim N(0, R_k)$
INITIALIZE	$\hat{\mathbf{x}}(t_0) = \hat{\mathbf{x}}_0$ $P_0 = E\left\{ \tilde{\mathbf{x}}(t_0) \tilde{\mathbf{x}}(t_0)^T \right\}$
GAIN	$K_k = P_k^- H_k^T \left[H_k P_k^- H_k^T + R_k \right]^{-1}$
UPDATE	$\hat{\mathbf{x}}_k^+ = \hat{\mathbf{x}}_k^- + K_k \left[\tilde{\mathbf{y}}_k - H_k \hat{\mathbf{x}}_k^- \right]$ $P_k^+ = \left[I - K_k H_k \right] P_k^-$
PROPAGATION	$\hat{\mathbf{x}}_{k+1}^- = \Phi_k \hat{\mathbf{x}}_k^+$ $P_{k+1}^- = \Phi_k P_k^+ \Phi_k^T + \Upsilon_k Q_k \Upsilon_k^T$

B. Kalman Filter Design for Relative Navigation

The first step in designing a Kalman filter is to develop a system model and measurement equation. For the relative navigation problem, the dynamic system model will represent the relative translational and rotational motion between the VisNav sensor and the target. The continuous state vector is defined as

$$\mathbf{x}(t) \equiv \begin{bmatrix} \mathbf{z}(t) \\ \dot{\mathbf{z}}(t) \\ \ddot{\mathbf{z}}(t) \end{bmatrix} \tag{4.16}$$

where

$$\mathbf{z}(t) \equiv \begin{bmatrix} \mathbf{o}(t) \\ \mathbf{p}(t) \end{bmatrix} \tag{4.17}$$

The relative position $\mathbf{o}(t)$ and attitude $\mathbf{p}(t)$ are defined in (3.1) and (3.3). The state vector $\mathbf{x}(t)$ is an (18×1) vector consisting of the relative position, attitude, translational velocity, rotational velocity, translational acceleration, and rotational acceleration.

To develop the relative equations of motion, one simplifying assumption will be made. It is assumed that the relative translational and rotational accelerations are constant, or $\dddot{\mathbf{z}}(t) = 0$. This is a relatively acceptable assumption in the case of aerial refueling because ideally the closing rate and acceleration between the receiver and drogue will be small. Since there is still some error in this assumption, however, process noise $\mathbf{w}(t)$ will be added to the $\dddot{\mathbf{z}}(t)$ equation only. In this case the process noise represents dynamics which are present in the real system but not in the model.

The continuous dynamic model for the Kalman filter is

$$\dot{\mathbf{x}}(t) = \begin{bmatrix} \dot{\mathbf{z}}(t) \\ \ddot{\mathbf{z}}(t) \\ \dddot{\mathbf{z}}(t) \end{bmatrix} = \begin{bmatrix} 0 & I & 0 \\ 0 & 0 & I \\ 0 & 0 & 0 \end{bmatrix} \begin{bmatrix} \mathbf{z}(t) \\ \dot{\mathbf{z}}(t) \\ \ddot{\mathbf{z}}(t) \end{bmatrix} + \begin{bmatrix} 0 \\ 0 \\ I \end{bmatrix} \mathbf{w}(t) \tag{4.18}$$

where I is a (6×6) identity matrix. Note that the model does not include a control input $\mathbf{u}(t)$ to the system. The kinematic relationships between position, velocity, and acceleration in (4.18) are modeled exactly. All of the error in the model comes from the assumption that the relative acceleration is constant. In discrete time, (4.18) becomes

$$\mathbf{x}_{k+1} = \Phi_k \mathbf{x}_k + \Upsilon_k \mathbf{w}_k \tag{4.19}$$

where

$$\Phi_k = \begin{bmatrix} I & (t_{k+1} - t_k) I & \frac{1}{2}(t_{k+1} - t_k)^2 I \\ 0 & I & (t_{k+1} - t_k) I \\ 0 & 0 & I \end{bmatrix} \quad \text{and} \quad \Upsilon_k = \begin{bmatrix} 0 \\ 0 \\ I \end{bmatrix}$$

The VisNav sensor takes discrete measurements of the line of sight vectors to each beacon and estimates the relative position and attitude using the nonlinear least squares algorithm described in Chapter III. In the discrete-time form of the Kalman filter formulation, it is assumed that measurements are available at each time step. This corresponds to an integration step size of $(t_{k+1} - t_k) = 0.01$ sec with a VisNav update rate of 100 Hz. The six degree-of-freedom relative navigation solution from VisNav at time step k is the measured output of the system,

$$\tilde{\mathbf{y}}_k = \begin{bmatrix} I & 0 & 0 \end{bmatrix} \begin{bmatrix} \mathbf{z}_k \\ \dot{\mathbf{z}}_k \\ \ddot{\mathbf{z}}_k \end{bmatrix} + \mathbf{v}_k = H_k \mathbf{x}_k + \mathbf{v}_k \tag{4.20}$$

where $\mathbf{v}_k$ represents the error in the VisNav solution. The measurement error covariance $R_k = E\left\{\mathbf{v}_k \mathbf{v}_k^T\right\}$ is required for the Kalman filter formulation. The VisNav sensing system provides a time-varying measurement error covariance matrix from the GLSDC algorithm, which may be passed to the Kalman filter as

$$R_k = \left(\bar{H}_k^T W \bar{H}_k\right)^{-1} \tag{4.21}$$

Recall from Chapter III that $\bar{H}$ is the measurement sensitivity matrix defined in (3.19) and W is the weighting matrix in GLSDC. When the output from VisNav has a high degree of error, R_k will be large and the dynamic model in the filter will improve the estimate by enforcing the kinematic relationships in the system. As the estimates from VisNav improve, the value of R_k will decrease, and the filter will rely more heavily on the measurements. Disruptions in the solution due to beacon drop-out or loss of lock will cause R_k to increase in magnitude, and the Kalman gain in (4.15) will be reduced to place less emphasis on the measurements from VisNav. The relative weighting between Q_k (modeling error) and R_k (measurement error) determines the convergence behavior of the filter estimated states. The selection of Q_k is discussed in the next section.

C. Tuning the Kalman Filter for Aerial Refueling

The process of tuning the Kalman filter is application-dependent, and must therefore involve simulations involving realistic aerial refueling scenarios. The value of Q_k, which quantifies the degree to which the constant acceleration assumption is true, is used as the tuning parameter. Q_k is a symmetric positive-definite matrix, defined in Section B as

$$Q_k = E\left\{\mathbf{w}_k \mathbf{w}_k^T\right\} \tag{4.22}$$

It is necessary to simulate the estimation process in order to find appropriate values for Q_k. This is due to the fact that the process noise $\mathbf{w}_k$ represents modeling error, which is not a random or uncorrelated process. During the tuning process the estimation error, defined in (4.8), is typically plotted versus time, along with the so-called 3σ bounds. The 3σ bounds are calculated by multiplying the square root of the diagonal elements P_k by a factor of three. For a Gaussian process, the probability of any sample lying within the 3σ bounds is 99.7% [32]. Although $\mathbf{w}_k$ is not a true Gaussian process in this case, the 3σ bounds remain good indicators of the performance of the Kalman filter. While the estimation error may only be calculated in simulation (where the true state is known), the estimation error covariance P_k can be used in practice to give an indication of the error in the estimate and thus the performance of the filter. The tuning process is used to ensure that the estimation error covariance is consistent with the estimation error for realistic docking scenarios.

An example of tuning the Kalman filter is shown in Fig. 14. In the topmost graph, the estimation error exceeds the 3σ bounds in several places, indicating that the magnitude of Q_k is too small. The middle plot shows an example of a well-tuned Kalman filter, where the estimation error touches, but does not exceed the bounds over the entire simulation. The bottom graph shows a noticeable gap between the estimation error and the 3σ bounds, meaning that Q_k is too large.

The value of Q_k for the Kalman filter described in Section B will be determined through a series of simulations of closed-loop docking maneuvers. It will be represented as a constant matrix,

$$Q_k = \begin{bmatrix} q_1 I & 0 \\ 0 & q_2 I \end{bmatrix} \tag{4.23}$$

where q_1 and q_2 are scalars corresponding to the relative translational and rotational

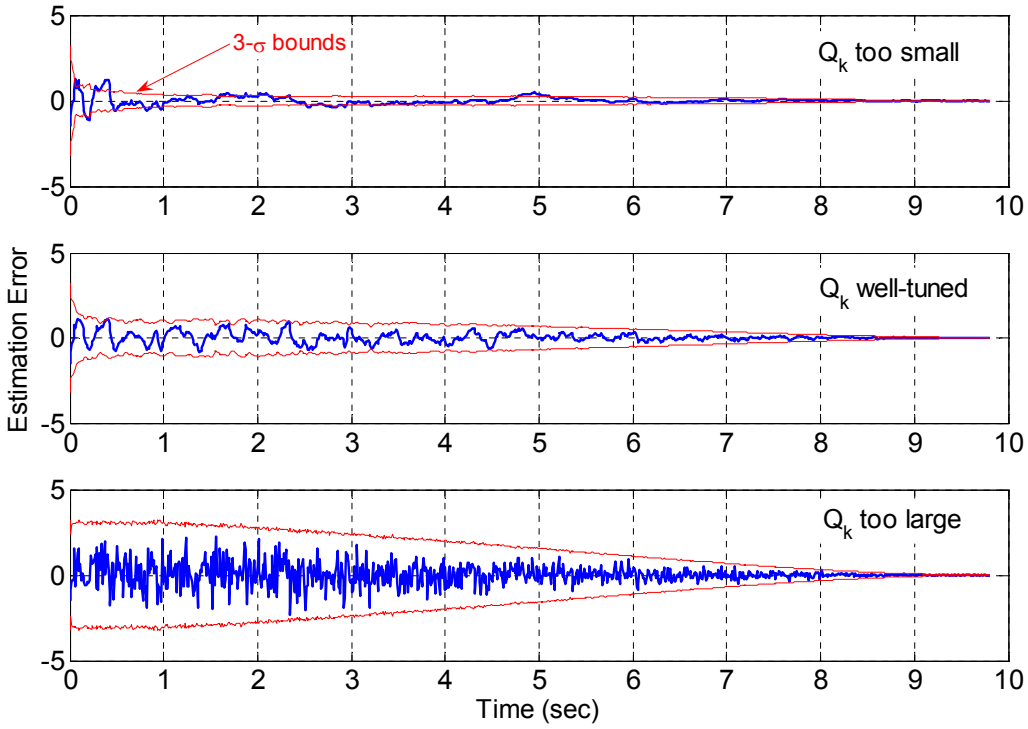

Fig. 14. Sample tuning parameters for the Kalman filter

acceleration, respectively. Two scalars were chosen to account for differences in the order of magnitude of the rotational and translational acceleration terms. The process of selecting q_1 and q_2 is described in Chapter VII.

CHAPTER V

REFERENCE OBSERVER-BASED TRACKING CONTROLLER

The Reference Observer-based Tracking Controller (ROTC) was developed for autonomous aerial refueling in [27] by Tandale, Bowers and Valasek. This chapter describes the controller structure, as shown in Fig. 15. The control objective is defined in Section A. Sections B, C, and D describe the main components of the controller: the reference trajectory generation module, the observer, and the feedback control law. Lastly, a robustness analysis is presented in Section E.

A. Control Objective

This section will describe the aerial refueling scenario and define the control problem. To begin, it is assumed that the receiver aircraft has located the refueling drogue, and has adjusted its heading angle to match that of the tanker aircraft. Both vehicles are assumed to be traveling at constant velocity V_P when the docking maneuver begins. An inertial coordinate frame $N : \{X_N, Y_N, Z_N\}$ is defined such that the steady-state heading of the receiver aircraft is oriented along the X_N axis, and the gravity vector acts along the Z_N axis. A body-fixed coordinate system $B : \{X_B, Y_B, Z_B\}$ is attached to the receiver aircraft at the center of gravity. Both frames are shown in Fig. 16. The inertial coordinates of the receiver aircraft and the drogue at time t are defined as $(X(t), Y(t), Z(t))$ and $(X_d(t), Y_d(t), Z_d(t))$, respectively.

The controller presented in this chapter is developed assuming that the receiver aircraft is modeled as a linear time-invariant system. To obtain a linear model, the general airplane equations of motion must linearized about a steady-state flight condition. The states of this model represent perturbations of the motion variables from their steady-state (or equilibrium) values. It is therefore most useful to define

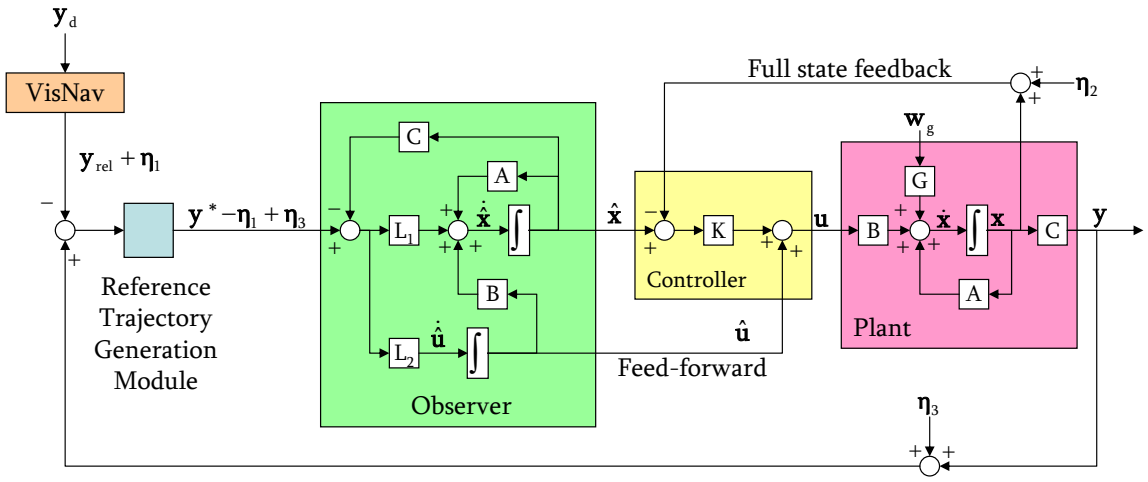

$\mathbf{y}$: Inertial position of receiver aircraft
$\mathbf{y}_d$: Inertial position of refueling drouge
$\mathbf{y}_{rel}$: Position of drogue relative to receiver
$\mathbf{y}^*$: Reference trajectory
$\mathbf{x}$: Receiver aircraft state vector
$\hat{\mathbf{x}}$: Observer state vector
$\mathbf{u}$: Receiver aircraft control vector
$\hat{\mathbf{u}}$: Observer control vector
$\mathbf{w}_g$: Gust input
$\boldsymbol{\eta}_1$: VisNav sensor noise
$\boldsymbol{\eta}_2$: Receiver position feedback noise
$\boldsymbol{\eta}_3$: Receiver state feedback noise

Fig. 15. Reference Observer-based Tracking Controller (ROTC) block diagram

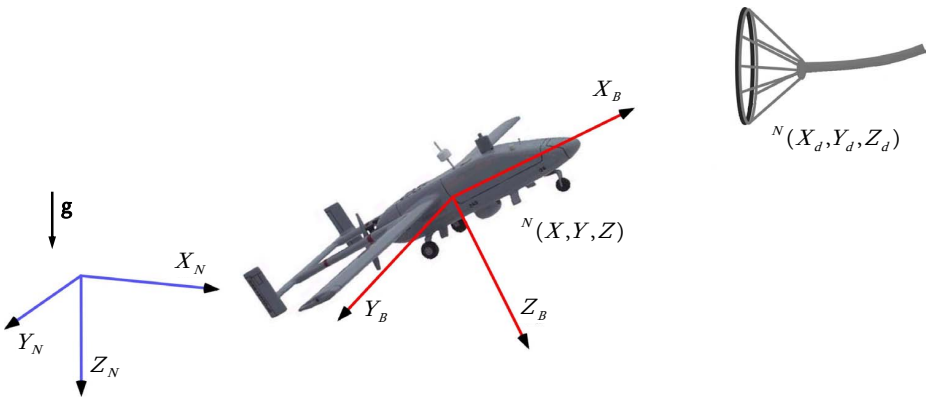

Fig. 16. Autonomous aerial refueling coordinate frames

the control objective in terms of *perturbed* motion variables. Thus the trajectory of the receiver aircraft will be defined as

$$\begin{aligned} X(t) &= X_1(t) + x(t) \\ Y(t) &= Y_1(t) + y(t) \\ Z(t) &= Z_1(t) + z(t) \end{aligned} \tag{5.1}$$

where the $(_1)$ subscript denotes the steady-state trajectory of the receiver, and (x, y, z) represent perturbations, or deviations, from the steady-state trajectory. The steady-state trajectory is defined by steady, level, $1g$ flight, where there is no net translational acceleration or angular velocity. The inertial coordinates of the drogue may be similarly defined as

$$\begin{aligned} X_d(t) &= X_1(t) + x_d(t) \\ Y_d(t) &= Y_1(t) + y_d(t) \\ Z_d(t) &= Z_1(t) + z_d(t) \end{aligned} \tag{5.2}$$

The inertial positions of the receiver and the drogue relative to the steady-state flight

path are thus defined as

$$\mathbf{y}(t) = \begin{bmatrix} x(t) \\ y(t) \\ z(t) \end{bmatrix} \quad \text{and} \quad \mathbf{y}_d(t) = \begin{bmatrix} x_d(t) \\ y_d(t) \\ z_d(t) \end{bmatrix} \tag{5.3}$$

The control objective is to drive the inertial position of the receiver aircraft to the inertial position of the drogue , or $\mathbf{y}(t) \rightarrow \mathbf{y}_d(t)$ over a specified finite time interval (t_0, t_f).

B. Reference Trajectory Generation

The purpose of the reference trajectory generation module is to produce a feasible trajectory that drives the probe of the receiver aircraft to the drogue. The docking maneuver is performed over the time interval (t_0, t_f). To ensure that the reference trajectory is feasible and does not cause control saturation, t_f must be chosen judiciously as a function of the initial offset between the receiver and the drogue. There are several ways to do this, depending on the constraints on the receiver aircraft states and controls. For this research, the final time is determined by

$$t_f = 10 * \text{ceil}\left(\frac{|\bar{x}_d| + |\bar{y}_d| + |\bar{z}_d|}{\gamma_f}\right) \tag{5.4}$$

where the "ceil" function rounds the argument up to the nearest integer, and γ_f is a design parameter which is chosen such that the closing rate between the receiver and the drogue is sufficiently small. The closing rate is typically less than 4 ft/s, depending on the specifications of the refueling equipment.

Because the tanker and the receiver aircraft have the same initial speed and

orientation, the offset at time t_0 is constant. This initial displacement is defined as

$$\begin{aligned} x_d(t_0) &= \bar{x}_d \\ y_d(t_0) &= \bar{y}_d \\ z_d(t_0) &= \bar{z}_d \end{aligned}$$

The range in X_N is gradually reduced using a reference trajectory that is generated with a smooth 7^{th} order polynomial. The reference trajectory is defined from t_0 to t_f as

$$x_{ref}(t) = \mathbf{f}(t)\mathbf{a}_x \tag{5.5}$$

where $\mathbf{a}_x \in \Re^4$ and

$$\mathbf{f}(t) \equiv \begin{bmatrix} t^4 & t^5 & t^6 & t^7 \end{bmatrix} \tag{5.6}$$

The four coefficients in $\mathbf{a}_x$ are found by enforcing the final position, $\bar{x}_d$, and zero velocity, acceleration, and jerk at t_f:

$$\mathbf{a}_x = \begin{bmatrix} \mathbf{f}(t_f) \\ \mathbf{f}'(t_f) \\ \mathbf{f}''(t_f) \\ \mathbf{f}'''(t_f) \end{bmatrix}^{-1} \begin{bmatrix} \bar{x}_d \\ 0 \\ 0 \\ 0 \end{bmatrix} \tag{5.7}$$

The Y_N and Z_N components of the reference trajectory, y_{ref} and z_{ref}, are defined for two stages during the docking maneuver, as shown in Fig. 17. In the first stage from time t_0 to t_1, a smooth 7^{th} order polynomial reference trajectory is designed to overcome the initial offsets $\bar{y}_d$ and $\bar{z}_d$. In the second stage from t_1 to t_f, another reference trajectory is designed to track small changes in y_d and z_d as the range $(x_d - x)$ decreases in the end game.

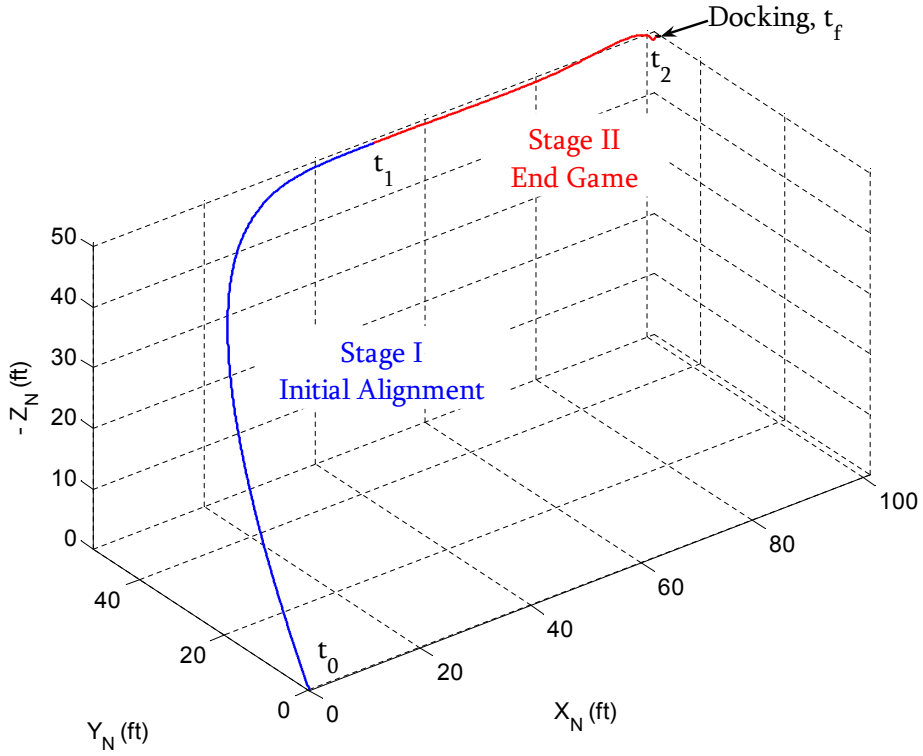

Fig. 17. Reference trajectory design

1. Stage I: Initial Alignment

The purpose of the first stage of the docking maneuver is to align the receiver aircraft in the Y_N and Z_N directions. Stage I lasts from t_0 to t_1, which is determined as a fraction of the total time

$$t_1 = \gamma_1 t_f \tag{5.8}$$

The design parameter γ_1 is selected to ensure that the trajectory is not too aggressive, i.e. the receiver aircraft has enough control effectiveness to track the reference. Similar to (5.5), y_{ref} and z_{ref} are defined as

$$y_{ref}(t) = \mathbf{f}(t)\mathbf{a}_y \tag{5.9}$$

$$z_{ref}(t) = \mathbf{f}(t)\mathbf{a}_z \tag{5.10}$$

where $\mathbf{a}_y$ and $\mathbf{a}_z$ are determined by enforcing the final position at t_1, as well as zero velocity, acceleration, and jerk:

$$\mathbf{a}_y = \begin{bmatrix} \mathbf{f}(t_1) \\ \mathbf{f}'(t_1) \\ \mathbf{f}''(t_1) \\ \mathbf{f}'''(t_1) \end{bmatrix}^{-1} \begin{bmatrix} \bar{y}_d \\ 0 \\ 0 \\ 0 \end{bmatrix}, \quad \mathbf{a}_z = \begin{bmatrix} \mathbf{f}(t_1) \\ \mathbf{f}'(t_1) \\ \mathbf{f}''(t_1) \\ \mathbf{f}'''(t_1) \end{bmatrix}^{-1} \begin{bmatrix} \bar{z}_d \\ 0 \\ 0 \\ 0 \end{bmatrix} \tag{5.11}$$

2. Stage II: End Game Precision Tracking

Once the receiver aircraft is aligned with the drogue, it must track small changes in position laterally and vertically during Stage II, which lasts from t_1 to t_f. The position of the drogue during this stage is represented as

$$y_d(t) = \bar{y}_d + \Delta y_d(t) \tag{5.12}$$

$$z_d(t) = \bar{z}_d + \Delta z_d(t) \tag{5.13}$$

The reference trajectory after t_1 is defined as

$$y_{ref}(t) = \bar{y}_d + K_{ref}(t)\Delta y_d(t) \tag{5.14}$$

$$z_{ref}(t) = \bar{z}_d + K_{ref}(t)\Delta z_d(t) \tag{5.15}$$

The gain $K_{ref}(t)$ is determined by

$$K_{ref}(t) = \begin{cases} 10\left(\frac{t-t_1}{t_2-t_1}\right)^3 - 15\left(\frac{t-t_1}{t_2-t_1}\right)^4 + 6\left(\frac{t-t_1}{t_2-t_1}\right)^5 & \text{for } t \leq t_2 \\ 1 & \text{for } t > t_2 \end{cases} \tag{5.16}$$

The definition of K_{ref} allows for a smooth transition from the first stage to the second stage, so there is not a discontinuity in the reference. The gain is gradually increased

from 0 at time t_1 to 1 at time t_3 using a 5^{th} order polynomial. The time at which the gain becomes 1 is determined by

$$t_2 = \gamma_2 t_f \tag{5.17}$$

where the parameter γ_2 is selected by the designer.

C. Observer Design

The reference trajectory in Section B is defined in terms of the three receiver aircraft position states: x, y, and z. The controller designed in Section D, however, is full-state and requires references for *all* of the states and controls. This section will develop an observer that is used to estimate the full reference state and control vectors based on the reference trajectory. In essence, the observer will determine what the states and controls of the receiver must be in order to follow the reference trajectory.

The receiver aircraft equations of motion are represented as a linear time-invariant system,

$$\begin{aligned} \dot{\mathbf{x}}(t) &= A\mathbf{x}(t) + B\mathbf{u}(t) \\ \mathbf{y}(t) &= C\mathbf{x}(t) \end{aligned} \tag{5.18}$$

where $\mathbf{x}(t) \in \Re^n$ is the state vector, $\mathbf{u}(t) \in \Re^m$ is the control vector, $\mathbf{y}(t) \in \Re^r$ is the output vector, and A, B, and C are real, constant matrices of the appropriate dimension. The output vector is defined as

$$\mathbf{y}(t) = \begin{bmatrix} x(t) \\ y(t) \\ z(t) \end{bmatrix} \tag{5.19}$$

where $x(t)$, $y(t)$, and $z(t)$ are defined in (5.1). Let $\mathbf{y}^*(t)$ represent the *desired* output,

defined as

$$\mathbf{y}^*(t) = \begin{bmatrix} x_{ref}(t) \\ y_{ref}(t) \\ z_{ref}(t) \end{bmatrix} \tag{5.20}$$

where x_{ref}, y_{ref}, and z_{ref} are defined in Section B. For the output to follow the desired output, or $\mathbf{y}(t) \rightarrow \mathbf{y}^*(t)$, there must exist states $\mathbf{x}^*(t)$ and controls $\mathbf{u}^*(t)$ such that

$$\begin{aligned} \dot{\mathbf{x}}^*(t) &= A\mathbf{x}^*(t) + B\mathbf{u}^*(t) \\ \mathbf{y}^*(t) &= C\mathbf{x}^*(t) \end{aligned} \tag{5.21}$$

An output injection observer may now be designed to estimate $\mathbf{x}^*(t)$ and $\mathbf{u}^*(t)$ from $\mathbf{y}^*(t)$. To do this, first an augmented state vector is defined as

$$\mathbf{X}^* = \begin{bmatrix} \mathbf{x}^* & \mathbf{u}^* \end{bmatrix}^T \tag{5.22}$$

Taking the derivative, it is seen that

$$\begin{aligned} \dot{\mathbf{X}}^* &= \mathcal{A}\mathbf{X}^* + \mathcal{B}\dot{\mathbf{u}}^* \\ \mathbf{y}^* &= \mathcal{C}\mathbf{X}^* \end{aligned} \tag{5.23}$$

where

$$\mathcal{A} = \begin{bmatrix} A & B \\ 0 & 0 \end{bmatrix}, \quad \mathcal{B} = \begin{bmatrix} 0 \\ I \end{bmatrix}, \quad \mathcal{C} = \begin{bmatrix} C & 0 \end{bmatrix} \tag{5.24}$$

The augmented observer state vector is defined as

$$\hat{\mathbf{X}} = \begin{bmatrix} \hat{\mathbf{x}} & \hat{\mathbf{u}} \end{bmatrix}^T \tag{5.25}$$

where the ($\hat{}$) denotes an estimated quantity. The observer dynamics are specified as

$$\begin{aligned} \dot{\hat{\mathbf{X}}} &= \mathcal{A}\hat{\mathbf{X}} + L\mathcal{C}\left(\mathbf{X}^* - \hat{\mathbf{X}}\right) \\ \hat{\mathbf{y}} &= \mathcal{C}\hat{\mathbf{X}} \end{aligned} \tag{5.26}$$

where $L \in \Re^{(n+m)\times r}$ is observer gain. The observer error $\mathbf{e}$ is defined as the difference between the desired state and the estimated state:

$$\mathbf{e} = \mathbf{X}^* - \hat{\mathbf{X}} \tag{5.27}$$

The observer error dynamics are found by taking the time derivative of (5.27) and substituting (5.23) and (5.26):

$$\dot{\mathbf{e}} = (\mathcal{A} - L\mathcal{C})\,\mathbf{e} + \mathcal{B}\dot{\mathbf{u}}^* \tag{5.28}$$

Here it is seen that the error dynamics are determined by the poles of $(\mathcal{A} - L\mathcal{C})$ as well as a bounded disturbance $\mathcal{B}\dot{\mathbf{u}}^*$. Assuming that $(\mathcal{A}, \mathcal{C})$ is observable, the observer gain L may be selected using the dual of the Linear Quadratic Regulator theory [33] as

$$L = P_o\mathcal{C}^T R_o^{-1} \tag{5.29}$$

where P_o is a solution to the steady-state algebraic Riccati equation

$$0 = \mathcal{A}P_o + P_o\mathcal{A}^T + Q_o - P_o\mathcal{C}^T R_o^{-1}\mathcal{C}P_o \tag{5.30}$$

Q_o, a positive semi-definite weighting matrix, and R_o, a positive definite weighting matrix, are both selected by the designer. When the bounded disturbance $\mathcal{B}\dot{\mathbf{u}}^*$ becomes zero, the estimation error tends to zero asymptotically.

D. Trajectory Tracking Controller Design

The trajectory tracking controller is a variation of the Nonzero Set Point control structure from [23, 24, 25]. In NZSP, $\mathbf{x}^*$ and $\mathbf{u}^*$ represent the desired states and controls which will cause the output $\mathbf{y}$ to approach the desired output $\mathbf{y}^*$ as $t \to \infty$. Because the desired output is assumed to be both known and constant, the desired states and controls may be found off-line using analytical methods. However, in the ROTC formulation, the desired output is not perfectly known or constant, hence the desired states and controls must be estimated on-line using the observer described in Section C. The controller is designed so that the plant states and controls track the desired states and controls. The derivation of the continuous controller is presented in Subsection 1, and a sampled-data version is presented in Subsection 2.

1. Continuous Controller

The errors between the plant states and controls and the desired states and controls are defined as

$$\tilde{\mathbf{x}}(t) \equiv \mathbf{x}(t) - \mathbf{x}^*(t) \tag{5.31}$$

$$\tilde{\mathbf{u}}(t) \equiv \mathbf{u}(t) - \mathbf{u}^*(t) \tag{5.32}$$

Differentiating with respect to time and substituting the system dynamics from (5.18) gives

$$\dot{\tilde{\mathbf{x}}} = A\tilde{\mathbf{x}} + B\tilde{\mathbf{u}} \tag{5.33}$$

Assuming that all of the states are available for feedback, the errors may be driven to zero using the control law

$$\tilde{\mathbf{u}} = -K\tilde{\mathbf{x}} \tag{5.34}$$

Assuming that (A, B) is controllable, the feedback gain K may be calculated using Linear Quadratic Regulator theory [33] as

$$K = R^{-1}B^T P_c \tag{5.35}$$

where P_c is determined from the steady-state Riccati equation

$$0 = A^T P_c + P_c A + Q - P_c B R^{-1} B^T P_c \tag{5.36}$$

The positive semi-definite state weighting matrix Q and the positive definite control weighting matrix R are selected by the designer. The selection of Q and R is an iterative process which involves simulation of the closed-loop system. The weight elements are typically adjusted to give the best tracking performance without saturating the controls. The closed-loop system is

$$\dot{\tilde{\mathbf{x}}} = (A - BK)\,\tilde{\mathbf{x}} \tag{5.37}$$

Expressed in terms of the plant states and controls

$$\mathbf{u} = \mathbf{u}^* + K(\mathbf{x}^* - \mathbf{x}) \tag{5.38}$$

If the desired states and controls $\mathbf{x}^*$ and $\mathbf{u}^*$ are replaced by the estimated state and control, $\hat{\mathbf{x}}$ and $\hat{\mathbf{u}}$, the control law becomes

$$\mathbf{u} = \hat{\mathbf{u}} + K\hat{\mathbf{x}} - K\mathbf{x} \tag{5.39}$$

The tracking error dynamics using the estimated state and control are given by

$$\dot{\tilde{\mathbf{x}}} = A\tilde{\mathbf{x}} + B\hat{\mathbf{u}} + BK\hat{\mathbf{x}} - BK\mathbf{x} - B\mathbf{u}^* \tag{5.40}$$

Adding and subtracting $BK\mathbf{x}^*$ from the right hand side of (5.40) gives

$$\dot{\tilde{\mathbf{x}}} = (A - BK)\,\tilde{\mathbf{x}} + \begin{bmatrix} BK & B \end{bmatrix} \begin{bmatrix} \hat{\mathbf{x}} - \mathbf{x}^* \\ \hat{\mathbf{u}} - \mathbf{u}^* \end{bmatrix} \tag{5.41}$$

Using the definition of the estimation error $\mathbf{e}$ from (5.27), the combined controller and estimator error dynamics are

$$\begin{bmatrix} \dot{\tilde{\mathbf{x}}} \\ \dot{\mathbf{e}} \end{bmatrix} = \begin{bmatrix} A - BK & [BK\ B] \\ 0 & \mathcal{A} - L\mathcal{C} \end{bmatrix} \begin{bmatrix} \tilde{\mathbf{x}} \\ \mathbf{e} \end{bmatrix} + \begin{bmatrix} 0 \\ \mathcal{B} \end{bmatrix} \dot{\mathbf{u}}^* \tag{5.42}$$

The eigenvalues of the combined controller and observer system are the union of the eigenvalues of $(A - BK)$ and $(\mathcal{A} - L\mathcal{C})$. This is proved using the following property of block diagonal matrices: If T, U, V, W are arbitrary matrices of the appropriate dimensions,

$$\det \begin{bmatrix} T & U \\ V & W \end{bmatrix} = \det(TW) - \det(UV) \tag{5.43}$$

$$\det(TW) = \det(T)\det(W) \tag{5.44}$$

This property allows the controller and observer gains to be designed separately. If both sets of gains are stabilizing, the combined system will also be stable with a bounded disturbance from the term $\dot{\mathbf{u}}^*$.

2. Sampled-Data Controller

In order to implement the control law on a digital computer, the control input may be defined as a piecewise constant function of time

$$\tilde{\mathbf{u}}(t) = \tilde{\mathbf{u}}(t_k) = \tilde{\mathbf{u}}_k \quad \text{for} \quad t_k \leq t \leq (t_k + T) \tag{5.45}$$

where T is the sample rate of the controller. This is equivalent to a zero-order hold acting on the sampled control input. Assuming that all of the states are available for feedback and are sampled at the discrete time points t_k, let the control law be given by,

$$\tilde{\mathbf{u}}_k = -K\tilde{\mathbf{x}}(t_k) \quad \text{for} \quad t_k \leq t \leq (t_k + T) \tag{5.46}$$

Assuming that (A, B) is controllable, the sampled-data regulator of [34] may be used to find the optimal gain K that minimizes the cost function

$$J = \frac{1}{2}\sum_{k=0}^{\infty}\left[\tilde{\mathbf{x}}_k\hat{Q}\tilde{\mathbf{x}}_k + \tilde{\mathbf{u}}_k\hat{R}\tilde{\mathbf{u}_k} + 2\tilde{\mathbf{x}}_k M\tilde{\mathbf{u}_k}\right]dt \tag{5.47}$$

where

$$\hat{Q} = \int_0^T \left(e^{A^T t}Qe^{At}\right)dt \tag{5.48}$$

$$M = \left\{\int_0^T \left[e^{A^T t}Q\left(\int_0^t e^{As}ds\right)\right]dt\right\}B \tag{5.49}$$

$$\hat{R} = RT + B^T\left\{\int_0^T \left[\left(\int_0^T e^{A^T ts}ds\right)Q\left(\int_0^t e^{A\tau}d\tau\right)\right]dt\right\}B \tag{5.50}$$

The positive semi-definite state weighting matrix Q and the positive definite control weighting matrix R are selected by the designer.

Let (Φ, Γ) be the discrete-time equivalents of the continuous system matrices (A, B) in (5.18) with sample period T. The sampled-data optimal gain is given

by[35]

$$K = \left(\hat{R} + \Gamma^T P_c^{-1} \Gamma\right)^{-1} \left(\Gamma^T P_c \Phi + M^T\right) \tag{5.51}$$

where P_c is the solution to the steady-state Riccati equation

$$P_c = \Phi^T P_c \Phi + \hat{Q} - \left(\Gamma^T P_c \Phi + M^T\right)^T \left(\hat{R} + \Gamma^T P_c \Gamma\right)^{-1} \left(\Gamma^T P_c \Phi + M^T\right) \tag{5.52}$$

The zero-order hold adds latency to the system, which grows as the sample period is increased. The controller is designed to track the output of the observer, therefore the frequency of the output signal of the observer is determined by the modeled aircraft dynamics. It is therefore necessary for the controller sample rate to be at least twice as fast as the fastest mode in the observer.

E. Frequency Domain Analysis

This section presents a frequency domain analysis of the continuous Reference Observer-based Tracking controller. The following analysis is used to give insight into the robustness properties of the closed-loop system, which includes the plant dynamics for the UCAV6 aircraft and the designed observer and controller gains (see Chapter VI). It is noted that the closed-loop robustness properties depend upon the selection of the weighting matrices in the observer and the controller, as well as the receiver aircraft model. Performance specifications and criteria depend upon the specified drogue dynamics and the noise properties of VisNav and the sensors on board the receiver aircraft.

The four exogenous input terms illustrated in Fig. 15, η_1, η_2, η_3, and $\mathbf{w}_g$ are considered. The sources of these inputs are sensor noise, estimation error, and atmospheric disturbances. A fifth exogenous input, Δ, is defined here to represent unmodeled plant dynamics. The effects of each term on the output of the system are

examined in this Section using a frequency domain analysis. The closed-loop system response is written in the frequency domain as

$$\mathbf{y}(s) = T_1(s)\mathbf{y}^* + T_1(s)\left(\eta_3 - \eta_1\right) + T_2(s)\eta_2 + T_3(s)\left(G_g\mathbf{w}_g(s) + G_d\Delta(s)\right) \tag{5.53}$$

where s is the Laplace variable $s = j\omega$ and

$$T_1(s) = C_{CL}\left(sI - A_{CL}\right)^{-1}\mathcal{L} \tag{5.54}$$

$$T_2(s) = C_{CL}\left(sI - A_{CL}\right)^{-1}\mathcal{K} \tag{5.55}$$

$$T_3(s) = C_{CL}\left(sI - A_{CL}\right)^{-1} \tag{5.56}$$

and

$$A_{CL} = \begin{bmatrix} (A - L_1C) & B & 0 \\ -L_2C & 0 & 0 \\ BK & B & (A - BK) \end{bmatrix} \quad C_{CL} = \begin{bmatrix} 0 & 0 & C \end{bmatrix}$$

$$\mathcal{L} = \begin{bmatrix} L_1 \\ L_2 \\ 0 \end{bmatrix} \mathcal{K} = \begin{bmatrix} 0 \\ 0 \\ -BK \end{bmatrix} \quad G_g = \begin{bmatrix} 0 \\ 0 \\ G \end{bmatrix} G_d = \begin{bmatrix} 0 \\ 0 \\ I \end{bmatrix}$$

The terms L_1 and L_2 are submatrices of the observer gain L in (5.29)

$$L = \begin{bmatrix} L_1 \\ L_2 \end{bmatrix} \tag{5.57}$$

such that $L_1 \in \Re^{(n\times r)}$ affects the estimated state $\hat{\mathbf{x}}$ and $L_2 \in \Re^{(m\times r)}$ affects the estimated control $\hat{\mathbf{u}}$. Singular-value decompositions (SVD) of the transfer functions (5.54)-(5.56) are used to give insight to the stability and performance robustness of the closed-loop system. For MIMO (multi-input multi-output) systems, the maximum

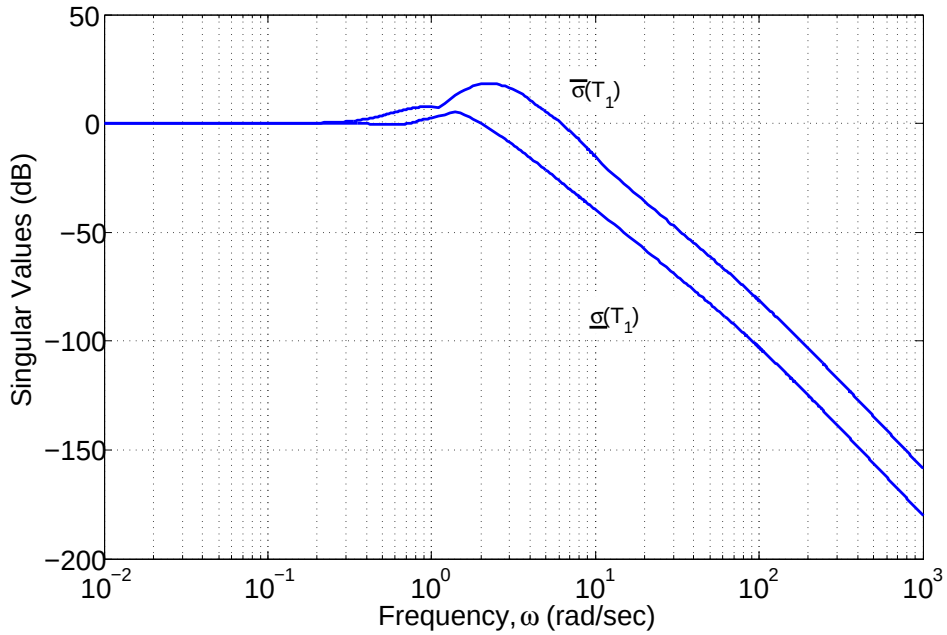

Fig. 18. Singular values of $T_1(s)$

and minimum singular values, denoted by $\overline{\sigma}$ and $\underline{\sigma}$ are plotted versus frequency ω.

The transfer function $T_1(s)$ in (5.54) characterizes the closed-loop system response to the reference signal $\mathbf{y}^*$ and to measurement noise $(\eta_3 - \eta_1)$. For perfect tracking performance, the singular values of $T_1(s)$ should be 0 dB for low frequencies. At high frequencies, a small maximum singular value $\overline{\sigma}(T_1)$ is desired in order to attenuate noise η_1 from the VisNav sensor and η_3 from the output feedback. The VisNav noise has a nominal frequency of 100 Hz, or 628 rad/sec (the update rate of the sensor). The maximum and minimum singular values of $T_1(s)$ are plotted versus frequency in Fig. 18.

It can be seen in Fig. 18 that for input frequencies between 0.3 and 6 rad/sec, the singular values of $T_1(s)$ surpass 0 dB, indicating that the reference signal is amplified by the system. The best tracking is achieved when the singular values equal 0 dB, which is true when the reference signal has a frequency below 0.3 rad/sec (about

1 Hz). Perfect tracking may be achieved in the first stage of docking because the reference signal comes from the 7^{th} order spline, which has a frequency well below 0.3 rad/sec. The frequency of reference signal during the second stage of the docking maneuver is characterized by the full motion of the drogue, therefore the dynamics of the drogue will determine the highest frequency in the reference signal. The fastest mode in the drogue model defined in Chapter VI is 0.387 rad/sec, so in this case the tracking performance is good. If faster drogue dynamics are specified, the weighting matrices Q and R should be adjusted to achieve better tracking at higher frequencies. Fig. 18 also shows that input signals greater than 10 rad/sec are attenuated by at least a factor of 10 dB. VisNav sensor noise is attenuated by a factor of 140 dB.

The transfer function $T_2(s)$ characterizes the response of the closed-loop system to noise η_2 in the full-state feedback. The frequency of η_2 depends on the type of sensors (or observers) which are used to measure (or estimate) the states. The maximum and minimum singular values of $T_2(s)$ are plotted versus frequency in Fig. 19. The plot shows that the system amplifies low-frequency noise and attenuates noise with frequency greater than 100 rad/sec by at least a factor of 10 dB. It may be concluded that the system is robust to noise in the feedback loop as long as it has a frequency higher than 100 rad/sec.

In addition to sensor noise, the closed-loop system experiences disturbances due to exogenous inputs from turbulence, $\mathbf{w}_g$, and a disturbance Δ which represents unmodeled dynamics. The transfer function $T_3(s)$ characterizes the closed-loop response to these two types of inputs. Fig. 20 presents the singular values of $T_3(s)$ versus frequency. It may be concluded from the figure that low frequency disturbances are amplified by the system. Low frequency disturbances may be caused by parametric uncertainty in the plant, indicating that the the receiver aircraft must be modeled well to achieve performance robustness. Disturbances with frequencies greater than

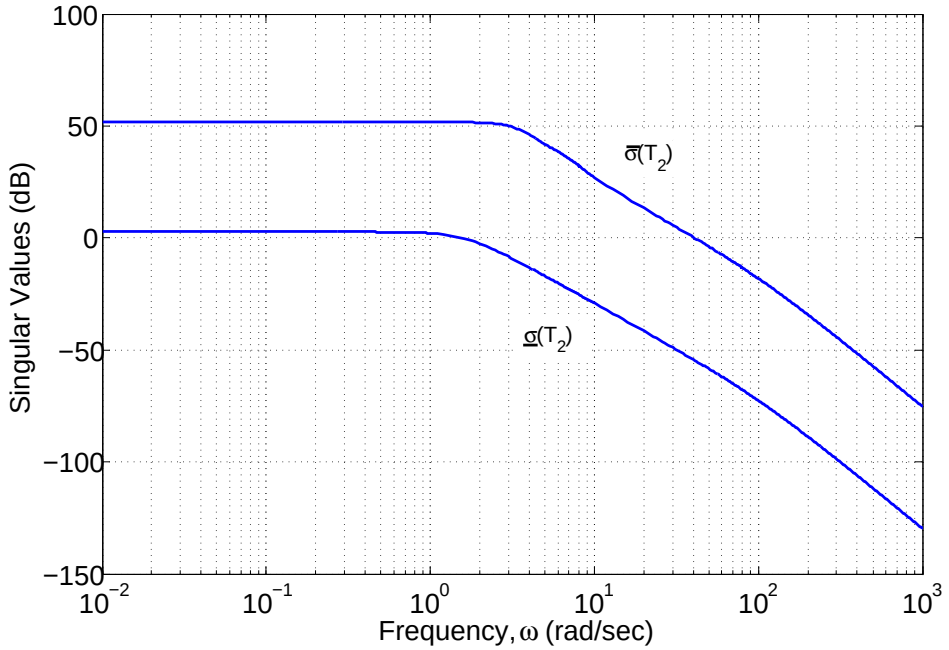

Fig. 19. Singular values of $T_2(s)$

about 16 rad/sec, however, are attenuated by at least a factor of 10. If the system has been modeled properly (i.e. all low-frequency modes are accurately represented), high-frequency unmodeled dynamics will be attenuated by the system.

Disturbances from atmospheric turbulence occur at low frequencies. Fig. 21 shows the minimum and maximum singular values of the transfer function $T_3(s)G_g$ and the singular values of the spectral density function for Dryden moderate turbulence. In the frequency range of the Dryden wind gusts, the maximum singular value of $T_3(s)G_g$ is slightly below 0 dB, indicating that inputs from gusts are attenuated, however the effects of the gusts will most likely be visible in the output of the system.

In summary, the robustness analysis shows that the designed closed-loop system has good tracking performance for the specified drogue dynamics. If different drogue dynamics are specified, the controller gains should be adjusted such that the singular values of $T_1(s)$ are 0 dB for all frequencies in the drogue dynamics. Measurement noise

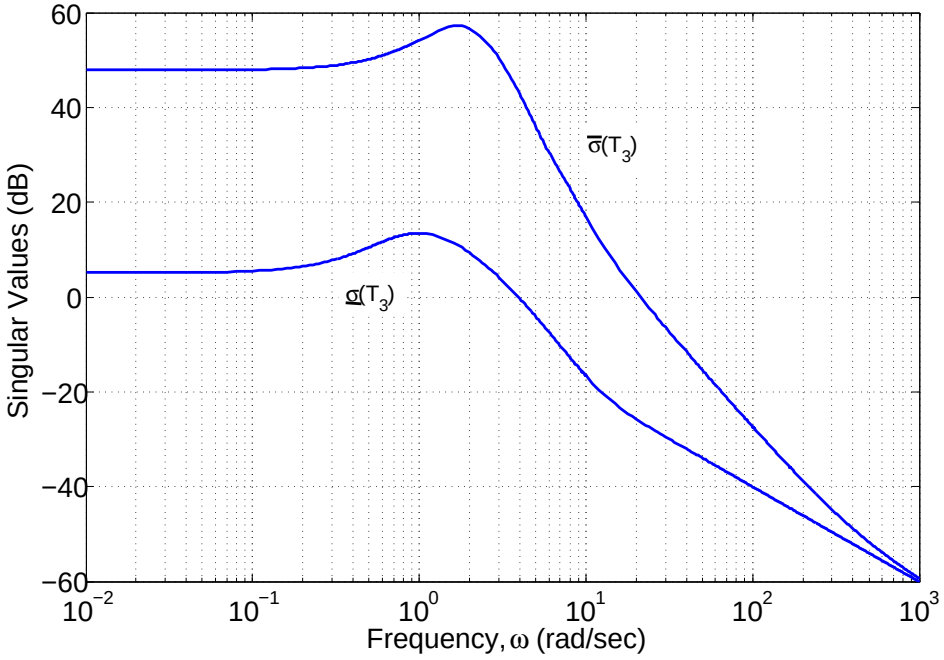

Fig. 20. Singular values of $T_3(s)$

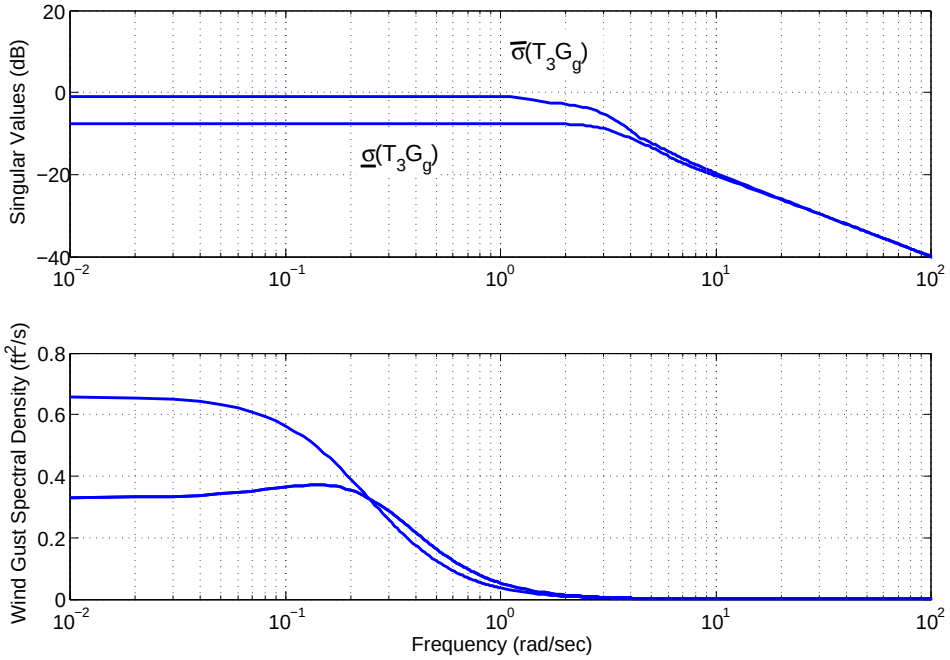

Fig. 21. Singular values of $T_3(s)G_g$ and Dryden gust spectral density

from the VisNav sensor is attenuated by a factor of 140 dB. The system is robust to noise in the full-state feedback as long as it has a frequency higher than 100 rad/sec. Although the low frequency gust disturbances are slightly attenuated by the system, turbulence effects will still be present in the output of the system. Lastly, performance robustness depends upon the parametric uncertainty in the receiver aircraft model. Previously published results have shown that the system performs well with as much as 10% error in the A matirx [27].

CHAPTER VI

AUTONOMOUS AERIAL REFUELING SIMULATION

Thus far all of the components of the AAR system have been developed independently. In order to examine the performance of the combined system, a medium fidelity simulation was developed that includes the receiver aircraft, VisNav sensor, the Kalman filter, controller, drogue, and atmospheric turbulence effects. The Kalman filter and controller were developed in Chapters IV and V. This chapter will describe the modeling of the remaining sub-systems in the simulation. In Section A, a mathematical model of the receiver aircraft is developed. Next, Section B discusses how representative drogue dynamics were selected for the simulation. Section C describes the model used to generate realistic atmospheric turbulence. Finally, a description of the detailed VisNav simulation model is presented in Section D.

A. Receiver Linear Aircraft Model

The receiver aircraft modeled in the simulation is called UCAV6 (Unmanned Combat Aerial Vehicle 6). It was constructed using a nonlinear batch simulation process developed at Texas A&M University in [36]. UCAV6 represents a 60% scale AV-8B Harrier (Fig. 22) with the pilot and associated equipment removed. The UCAV6 linear model was generated by linearizing the six degree-of-freedom airplane equations of motion about a steady-state flight condition. [37] describes this method of modeling aircraft flight dynamics. The steady, level $1g$ trim flight conditions for the model are listed in Table III.

The receiver aircraft equations of motion are represented as a linear time-invariant

Fig. 22. AV-8B Harrier during probe and drogue refueling

Table III. UCAV6 steady, level $1g$ trim states

Altitude	20,000	ft
Pitch attitude, Θ_1	4	deg
Forward speed, U_1	421	ft/s
Vertical speed, W_1	32	ft/s
Throttle setting, δ_{t1}	55	%
Elevator deflection, δ_{e1}	7	deg

state-space system,

$$\begin{aligned} \dot{\mathbf{x}}(t) &= A\mathbf{x}(t) + B\mathbf{u}(t) + G\mathbf{w}_g(t) \\ \mathbf{y}(t) &= C\mathbf{x}(t) \end{aligned} \tag{6.1}$$

where $\mathbf{x} \in \Re^{12}$ is the state vector, $\mathbf{u} \in \Re^4$ is the control vector, $\mathbf{y} \in \Re^3$ is the output vector, and $\mathbf{w}_g \in \Re^3$ is the input to the system due to atmospheric turbulence, discussed in Section C. The matrices A, B, C, and G, given in Appendix A, are of

Table IV. Receiver aircraft linear model states and controls

States	Definition	Units
(x, y, z)	Inertial position relative to steady-state flight path	ft
(U, V, W)	Body-axis velocity components	ft/s
(P, Q, R)	Body-axis angular rates	rad/s
(Ψ, Θ, Φ)	3-2-1 Euler Attitude Angles	rad
Control	**Definition**	**Units**
δ_e	Elevator deflection angle	deg
δ_T	Throttle setting	%
δ_a	Aileron deflection angle	deg
δ_r	Rudder deflection angle	deg

the appropriate dimension. The model states and controls are given in Table IV.

All model state variables are in expressed in terms of the body-fixed axis system with the exception of x, y, and z, which are expressed in the inertial frame (see Fig. 16) . The output vector is composed of the three inertial coordinates (x, y, z). The full receiver aircraft model is presented in Appendix A.

The UCAV6 control position and rate limits for UCAV6 are given in Table V. The throttle control (not listed in Table V has a minimum value of 0% and a maximum value of 100%. Although no specifications on the throttle rate limits are given in [29], a maximum throttle rate of 30% per second is assumed here. This throttle rate limit is representative of a high-performance aircraft engine. The position limits are enforced directly in the simulation code, but the rate limits are not. Selection of low controller gains will prevent rate saturation. The controls are sampled at a rate of 10 Hz using

Table V. UCAV6 control position and rate limits [29]

	Position(+) (deg)	Position(-) (deg)	Rate (deg/s)
Elevator, δ_e	13	-10	± 40
Aileron, δ_a	27	-27	± 100
Rudder, δ_r	15	-15	± 56

a zero-order hold for signal reconstruction. For this sample rate the performance of the closed-loop sampled-data system is very close to that of the continuous system.

B. Drogue Model

There is no existing drogue dynamic model based on empirical data, so a method of modeling representative drogue behavior was created. The movement of the drogue is modeled after a three degree-of-freedom spring mass damper system. The stiffness and damping coefficients were selected such that the drogue moves in a realistic manner as compared to video taken during flight test in [38]. The drogue is modeled as a linear time-invariant system,

$$\dot{\mathbf{x}}_d(t) = A_d \mathbf{x}_d(t) + B_d \mathbf{w}_g(t) \tag{6.2}$$

$$\dot{\mathbf{y}}_d(t) = C_d \mathbf{x}_d(t) \tag{6.3}$$

with the drogue state vector defined as

$$\mathbf{x}_d = \begin{bmatrix} \Delta x_d & \Delta y_d & \Delta z_d & \Delta \dot{x}_d & \Delta \dot{y}_d & \Delta \dot{z}_d \end{bmatrix}^T \tag{6.4}$$

where the quantities Δx_d, Δy_d, and Δz_d are defined in (5.12). The input $\mathbf{w}_g$ is an exogenous input representing a disturbance due to atmospheric turbulence, defined

in Section C. The state matrix A_d was selected as

$$A_d = \begin{bmatrix} 0 & 0 & 0 & 1 & 0 & 0 \\ 0 & 0 & 0 & 0 & 1 & 0 \\ 0 & 0 & 0 & 0 & 0 & 1 \\ -k_x & 0 & 0 & -c_x & 0 & 0 \\ 0 & -k_y & 0 & 0 & -c_y & 0 \\ 0 & 0 & -k_z & 0 & 0 & -c_z \end{bmatrix} \tag{6.5}$$

where the k and c parameters are listed in Table VI. B_d and C_d in (6.2) are

$$B_d = \begin{bmatrix} 0 & 0 & 0 \\ 0 & 0 & 0 \\ 0 & 0 & 0 \\ 0.01 & 0 & 0 \\ 0 & 0.3 & 0 \\ 0 & 0 & 0.3 \end{bmatrix} \quad C_d = \begin{bmatrix} 1 & 0 & 0 & 0 & 0 & 0 \\ 0 & 1 & 0 & 0 & 0 & 0 \\ 0 & 0 & 1 & 0 & 0 & 0 \end{bmatrix} \tag{6.6}$$

Table VI. Drogue dynamic model parameters

Parameter	Value	Units
k_x	0.15	$1/s^2$
k_y	0.06	$1/s^2$
k_z	0.10	$1/s^2$
c_x	0.50	$1/s$
c_y	0.04	$1/s$
c_z	0.05	$1/s$

C. Atmospheric Turbulence Model

The turbulence model in the AAR simulation is based on the Dryden turbulence model given in the Military Specification for Flying Qualities of Piloted Airplanes, MIL-F-8785C [39]. The Dryden turbulence model is based on a stochastic process defined by velocity spectra. For the three body-axis velocity components u, v, and w, the Dryden forms of the spectra are

$$\Phi_{u_g}(\Omega) = \sigma_u^2 \frac{2L_u}{\pi} \frac{1}{1+(L_u\Omega)^2} \tag{6.7}$$

$$\Phi_{v_g}(\Omega) = \sigma_v^2 \frac{L_v}{\pi} \frac{1+3(L_v\Omega)^2}{\left[1+(L_v\Omega)^2\right]^2} \tag{6.8}$$

$$\Phi_{w_g}(\Omega) = \sigma_w^2 \frac{L_w}{\pi} \frac{1+3(L_w\Omega)^2}{\left[1+(L_w\Omega)^2\right]^2} \tag{6.9}$$

where Ω is the spatial frequency of the turbulence field, L_u, L_v, and L_w are the turbulence scale lengths, and σ_u, σ_v, and σ_w are the root-mean-square (RMS) turbulence intensities. For medium to high altitudes, $L_u = L_v = L_w = 1,750$ ft and the turbulence intensity is selected from Fig. 23.

Coloring filters derived from (6.7) through (6.9) may be used to simulate velocity disturbances from inputs consisting of unit variance, band-limited white noise, ξ. These filters are transfer functions with inputs of white noise and outputs of the three body-axis gust velocity components:

$$H_u(s) \equiv \frac{u_{gust}(s)}{\xi(s)} \tag{6.10}$$

$$H_v(s) \equiv \frac{v_{gust}(s)}{\xi(s)} \tag{6.11}$$

$$H_w(s) \equiv \frac{w_{gust}(s)}{\xi(s)} \tag{6.12}$$

where s is the Laplace variable $s = j\omega$. For an aircraft traveling through the turbu-

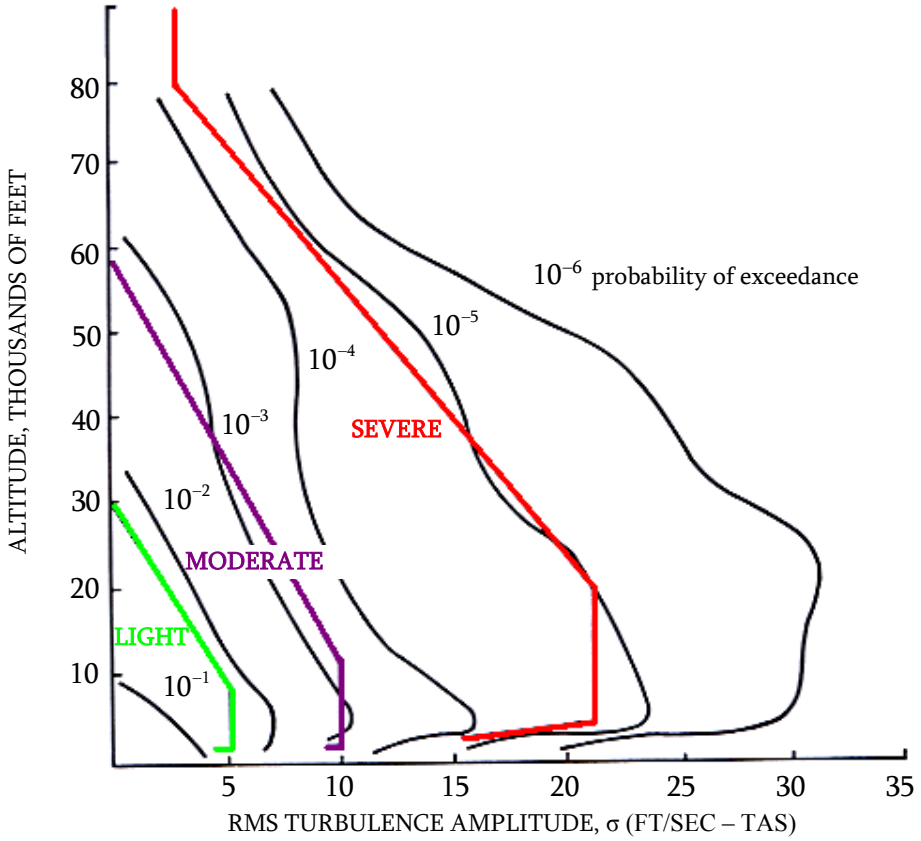

Fig. 23. Medium/high altitude turbulence intensities [39]

lence field at speed V_P, these filters are given by [40]

$$H_u(s) = \sigma_u \sqrt{\frac{2L_u}{\pi V_P}} \frac{1}{1 + \frac{L_u}{V_P} s} \tag{6.13}$$

$$H_v(s) = \sigma_v \sqrt{\frac{L_v}{\pi V_P}} \frac{1 + \frac{\sqrt{3}L_v}{V_P} s}{(1 + \frac{L_v}{V_P} s)^2} \tag{6.14}$$

$$H_w(s) = \sigma_w \sqrt{\frac{L_w}{\pi V_P}} \frac{1 + \frac{\sqrt{3}L_w}{V_P} s}{(1 + \frac{L_w}{V_P} s)^2} \tag{6.15}$$

The state-space realizations of (6.13) through (6.15) may be combined to form a single

time-domain model

$$\dot{\mathbf{x}}_g(t) = A_g\mathbf{x}_g(t) + B_g\mathbf{u}_g(t) \tag{6.16}$$

$$\mathbf{w}_g(t) = C_g\mathbf{x}_g(t) + D_g\mathbf{u}_g(t) \tag{6.17}$$

where $\mathbf{x}_g \in \Re^3$ is a state vector, $\mathbf{u}_g \in \Re^3$ is a vector of unit variance band-limited white noise, and $\mathbf{w}_g \in \Re^3$ is the output vector of body-axis velocity disturbances due to atmospheric turbulence,

$$\mathbf{w}_g = \begin{bmatrix} u_{gust} & v_{gust} & w_{gust} \end{bmatrix}^T \tag{6.18}$$

This vector of disturbances is an input to the aircraft model described in Section A. Atmospheric turbulence itself is independent of aircraft states, although clearly a large aircraft will respond differently than a small UAV to a given gust disturbance. This effect is captured by G in (6.1), which defines how gust disturbances act upon a particular aircraft. Appendix A gives the G matrix for the UCAV6, which is chosen as the negative of the columns of A corresponding to the body-axis velocities.

D. VisNav Sensor Model

A model of the VisNav sensor was developed for the AAR simulation to determine the behavior of the sensor in a closed-loop docking environment. A flowchart of the sensor model is presented in Fig. 24. The inputs to the simulated sensor are the positions and attitudes of the receiver and the drogue, the beacon arrangement on the drogue, and the previous estimate or initial guess for the GLSDC routine. Once the states (position and attitude) of the receiver and drogue are passed in, the "truth" relative position and orientation are calculated. These truth values are used to calculate the ideal line-of-sight (LOS) vectors to each beacon. The ideal LOS vectors are corrupted

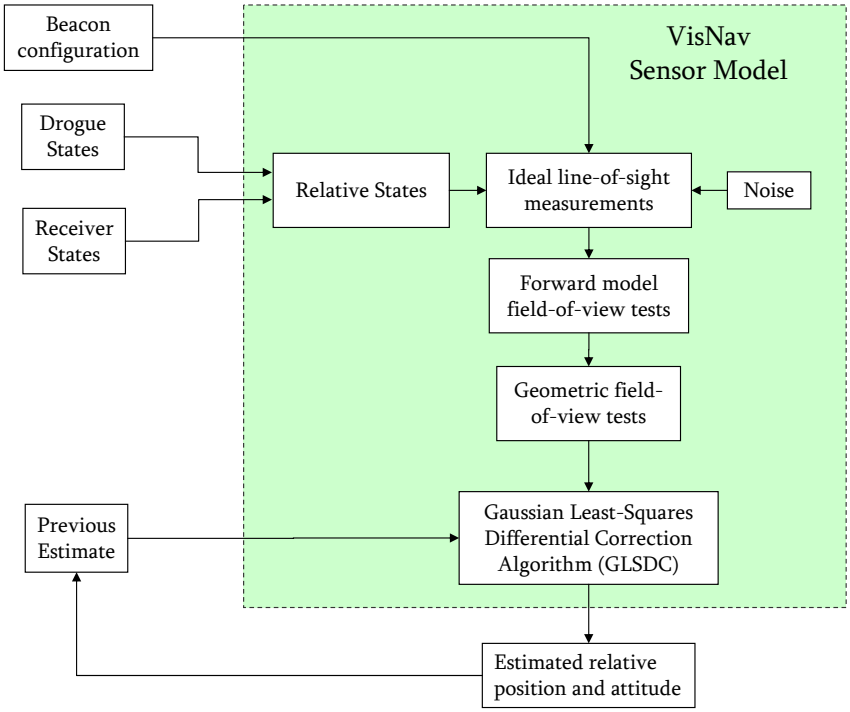

Fig. 24. VisNav sensor simulation diagram

with zero-mean Gaussian noise. To emulate optical distortion effects, measurements closer to the periphery of the sensor receive noise with a larger variance than those in the center. Beacon tests are performed to check the validity of the measurements. Measurements from a particular beacon are discarded if the light centroid does not fall within the calibrated area of the photodiode, or when a beacon is not in the sensor's field of view (forward model and geometric field-of-view tests). When measurements from a beacon fail one or both of the field-of-view tests, it is said that the beacon has dropped out, and those measurements are not given to the estimation routine. GLSDC is capable of producing an updated estimate with as few as four beacons. The sensor software is programmed to return the last available estimate when less than four beacons are available.

The detailed VisNav sensor model which was the basis for the simulation in

Fig. 24 is described in [41]. The main difference between the simulation used for this thesis and the code developed in [41] is a representation of the sensor calibration process. The real VisNav sensor undergoes a nonlinear calibration to establish the relationship between the measured PSD voltages and the image-space LOS coordinates. The calibration function, which is slightly different for each individual sensor, accounts for departures from the ideal pin-hole camera model due to small defects in the sensor hardware as well as the optical distortion due to the wide-angle lens. Of these two sources, the optical distortion produces the most significant nonlinearity.

A flowchart of the sensor model with calibration is shown in Fig. 25. Here the ideal line-of-sight measurements are passed through an inverse calibration function, which gives the ideal PSD voltages. These voltages are then corrupted with Gaussian white noise to obtain simulated measurements. The measured voltages are then passed through the calibration function to obtain the measured line-of-sight vector. Because the calibration function is highly nonlinear (especially away from the center of the PSD), the simulated measurement noise no longer has a Gaussian distribution. The measurements undergo field-of-view tests before and after the calibration process. Because the optical distortion decreases the field-of-view of the sensor, beacons are much more likely to fail a field-of-view test in the simulation which includes the calibration model.

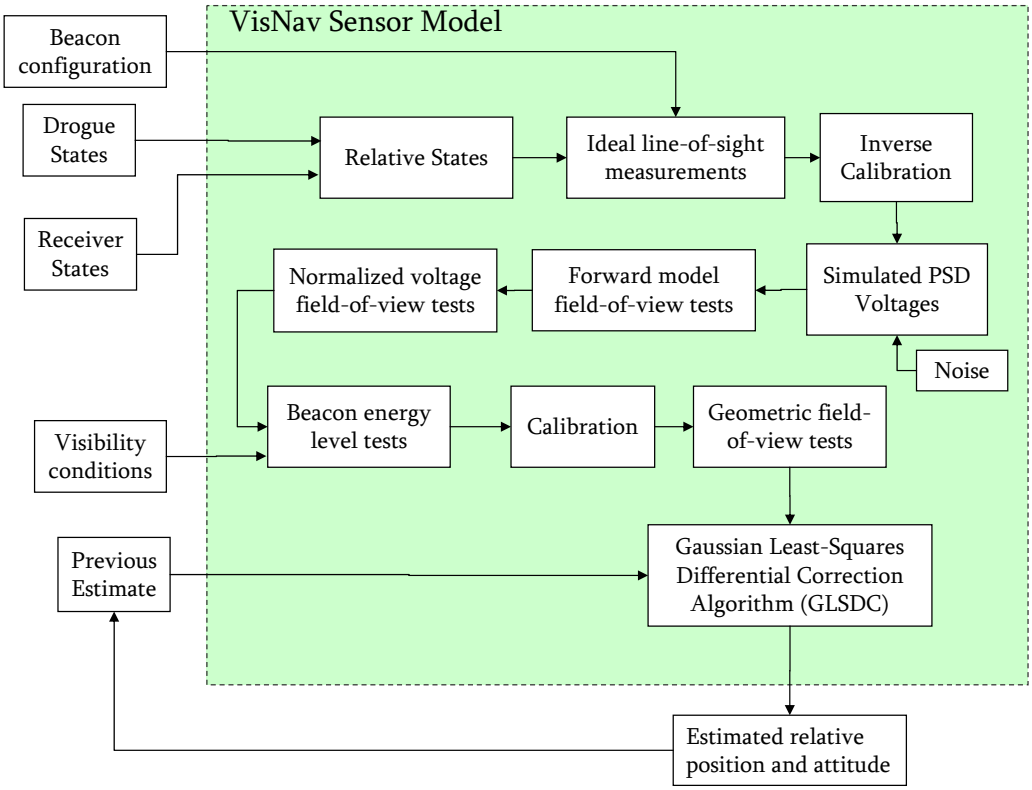

Fig. 25. VisNav sensor simulation with calibration model

The difference between the VisNav output using the simulation without calibration (Fig. 24) and with calibration (Fig. 25) is shown in Fig. 26. Although the sensor errors in both simulations have about the same magnitude, it is noted that the frequency of the two signals are quite different. The high-frequency errors in the sensor without calibration are a result of the sensor noise being added directly to the ideal LOS measurements. Because the GLSDC formulation assumes these type of noise characteristics, the 3σ bounds fit very well around the measurement error. In the simulation results which include the calibration model, it can be seen that the range errors in X_c are higher than those in the lateral and vertical directions, Y_c and Z_c. The high-frequency sensor noise is somewhat attenuated in the calibration process, however new low-frequency errors are introduced. The low-frequency error dynamics are a result of the Gaussian noise being passed through the nonlinear calibration function. Also, the fit of the calibration is dependent upon range, which introduces range-dependent errors if the sensor is calibrated for only one range. The overall performance of both versions is very similar as long as the beacons stay within the field of view.

The beacon configuration used in the AAR simulation is illustrated in Figs. 27 and 28. The arrangement is intented to give adequate depth-of-field in each dimension (i.e. no set of 3 or more beacons lie in the same plane) to improve the quality of the navigation solution from VisNav. The axis labels in the figure represent a drogue-fixed reference frame, with the the center of the refueling port at coordinates $(5, 0, 0)$ ft. The beacons are placed around the perimeter of the refueling drogue. The array has an outer radius of 1.5 feet in the $Y - Z$ plane, and a depth of 3 feet along the X-axis.

The performance of the VisNav sensor is highly dependent on the geometry of the beacon array. The operating range and susceptibility to beacon drop-out are the

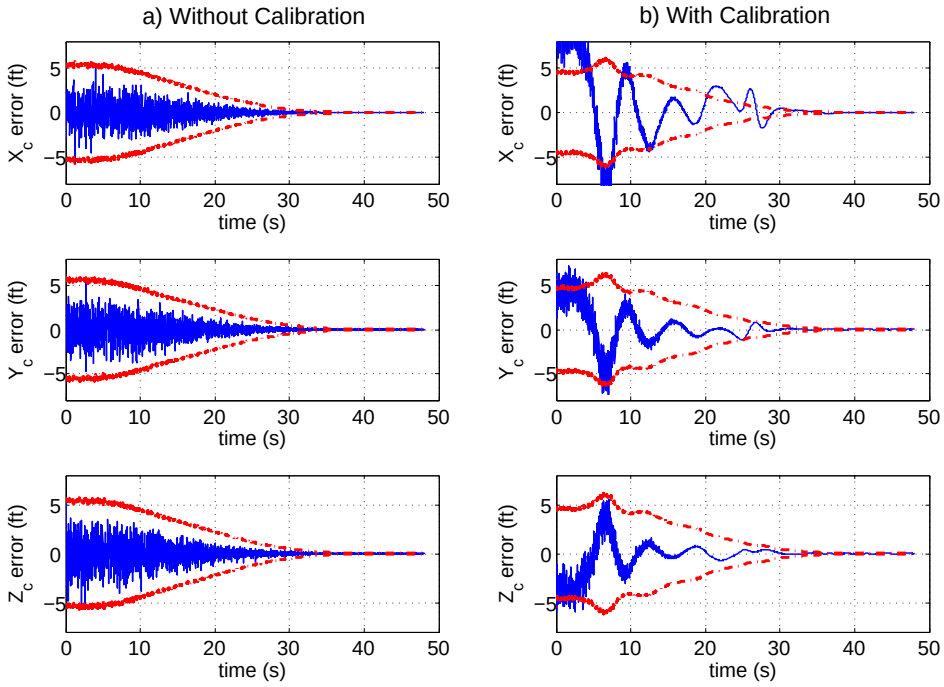

Fig. 26. Comparison of VisNav sensor simulation a) without calibration model and b) with calibration model

primary, conflicting concerns in the selection of beacon configuration. The beacon configuration in Figs. 27 and 28 was chosen to reduce beacon drop-out. As a result the operating range of the simulated sensor is about 100 ft. For operation at greater range, a larger array must be chosen, however this will most likely result in some beacons falling outside of the field of view at close range. Another limitation on the choice of beacon arrangement is the availability of space on the refueling drogue and/or tanker aircraft. Physical constraints such as moving control surfaces will most likely drive the placement of the beacons on the tanker aircraft. It is also noted that if the beacons move relative to each other (when they are placed on both the tanker and the drogue, for example) the VisNav navigation solution will be degraded.

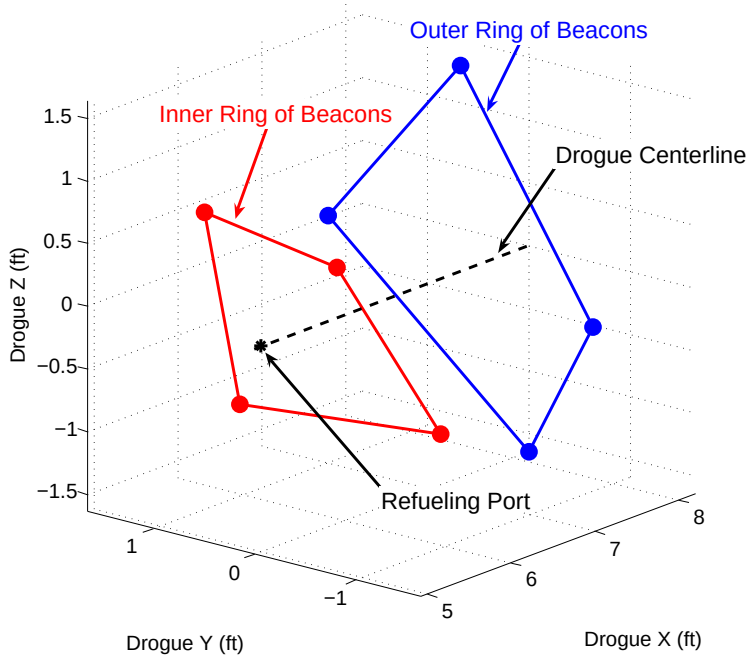

Fig. 27. 3-dimensional view of beacon configuration for AAR simulation

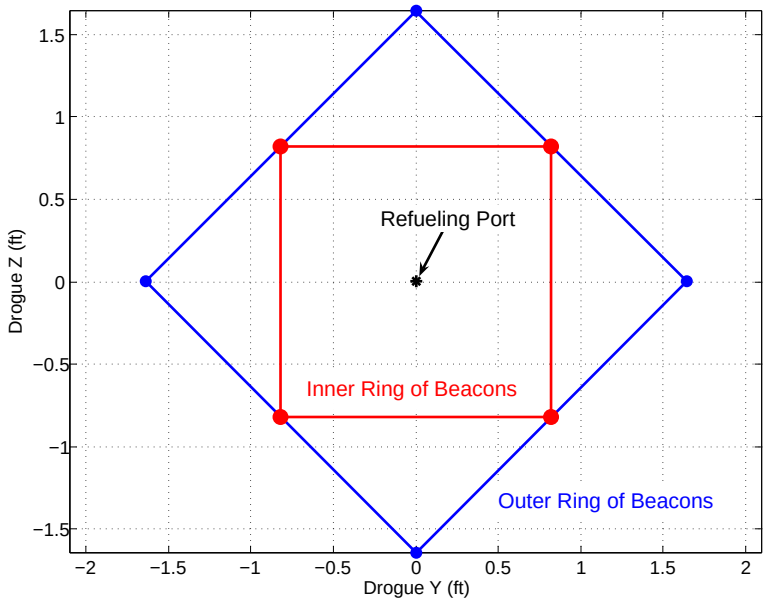

Fig. 28. Beacon configuration for AAR simulation

CHAPTER VII

EXPERIMENT DESIGN

This chapter defines the experiment that is used to demonstrate the performance of the combined sensor and controller for autonomous aerial refueling and to tune the Kalman filter. The autonomous aerial refueling simulation described in Chapter VI is the testing platform. Four test cases using VisNav and the Reference Observer-based Tracking Controller are simulated to evaluate the closed-loop docking performance under varying degrees of turbulence intensity. Once results from these simulations are obtained, they are used to tune the Kalman filter. Further simulations are then run to determine the closed-loop performance of the system with the tuned Kalman filter. The questions answered by the experiment are:

1. What is the closed-loop docking performance of the combined VisNav sensor and ROTC in still air, light turbulence, moderate turbulence, and severe turbulence?

2. How is the Kalman filter tuned for aerial refueling? Does the selection of the tuning parameters depend on the level of turbulence intensity?

3. How well does the tuned Kalman filter improve the navigation solution from VisNav in the refueling scenarios?

4. Does the combination of VisNav and Kalman filter result in improved closed-loop docking performance over VisNav alone?

The refueling scenario for the four cases is described in Section A, along with docking criteria and other measures of merit. The selection of the weighting matrices and other design parameters for the ROTC is detailed in Section B. Section C discusses the tuning criteria for the Kalman filter. After the Kalman filter is tuned,

several additional simulations are run to determine how the Kalman filter affects the closed-loop performance of the autonomous aerial refueling system. These simulations are described in Section D. The purpose of these simulations is to determine if the combination of the Kalman filter and VisNav improves the docking success rate in turbulence over VisNav alone.

A. Autonomous Aerial Refueling Scenario

The simulated autonomous aerial refueling takes place at an altitude of 20,000 feet, corresponding to the trim flight condition of the UCAV6 receiver aircraft. In each case the refueling drogue begins 100 feet ahead, 50 feet to the side, and 50 feet above the receiver aircraft, corresponding to an initial offset of

$$(\ \bar{x}_d, \quad \bar{y}_d, \quad \bar{z}_d \ ) = (\ 100, \quad 50, \quad -50 \ ) \ \text{ft}$$

The values of root-mean-squared (RMS) turbulence amplitude for each case are selected from Fig. 23 for the altitude of 20,000 feet (see Table VII). The magnitudes of the three body-axis turbulence intensities are chosen to be equal for simplicity. It is noted that in reality the vertical and lateral gusts σ_w and σ_w may have greater magnitude than the axial gusts σ_u.

The simulated drogue is given a small initial velocity so that it oscillates slightly in the $Y_N - Z_N$ plane, even in the absence of atmospheric turbulence. As the value of RMS turbulence intensity is increased, the oscillations of the drogue become larger in magnitude. The final docking error is calculated when $x - x_d = 0$ as

$$\text{docking error} = \sqrt{(y - y_d)^2 + (z - z_d)^2} \tag{7.1}$$

Successful docking is achieved when the docking error is less than 0.3 feet (about 4

Table VII. Kalman filter tuning cases for autonomous aerial refueling

	RMS Turbulence Amplitudes at 20,000 ft (ft/sec)	Probability of Exceedance [39]
Case 1	$\sigma_u = \sigma_v = \sigma_w = 0$ (None)	1/1
Case 2	$\sigma_u = \sigma_v = \sigma_w = 1$ (Light)	1/10
Case 3	$\sigma_u = \sigma_v = \sigma_w = 5$ (Moderate)	1/100
Case 4	$\sigma_u = \sigma_v = \sigma_w = 10$ (Severe)	1/10000

in), and the controls and control rates of receiver aircraft do not exceed the values given in Table V at any point during the simulation. After a successful docking, the receiver aircraft and the drogue are constrained to move together until the simulation ends at $t = 60$ seconds. If the receiver aircraft fails to dock with the refueling drogue when $x - x_d = 0$, the simulation is stopped.

B. Selection of ROTC Design Parameters

The trajectory generation module in the Reference Observer-based Tracking Controller designs a reference trajectory in two stages. The design parameters and critical times for the reference trajectory are listed in Table VIII. The design parameters γ_1, γ_2, and γ_f are chosen such that the average closing rate between the receiver aircraft and the drogue is around 2 ft/sec. The critical times are a function of the initial offset and the design parameters.

The first stage of the maneuver takes place from time $t_0 = 0$ to $t_1 = 25$ seconds. During this stage, a reference trajectory is generated to overcome the 50-foot offsets $\bar{y}_d$ and $\bar{z}_d$. Because the gross initial offset is assumed to be known from a different sensor such as GPS, measurements from the VisNav sensor are not used during Stage I. The

Table VIII. Reference trajectory design parameters and critical times

	Equation	Design Parameter	Value (sec)
Initial time, t_0	—	—	0
End of Stage I, t_1	(5.8)	$\gamma_1 = 0.5$	25
Time when $K_{ref} = 1$, t_2	(5.17)	$\gamma_2 = 0.8$	40
Projected docking time, t_f	(5.4)	$\gamma_f = 45$	50

second stage, or end game maneuver, begins at $t_1 = 25$ seconds. At this time the measurements from VisNav are used to track the position of the drogue. The sensor is active during the first stage so that a converged navigation solution is available at immediately at t_1. The reference gain in (5.14) is gradually increased from zero to one between t_1 and t_2. After t_2, the receiver aircraft tracks the full motion of the drogue. The trajectory is designed so that docking between the receiver aircraft and the refueling drogue occurs at approximately $t_f = 50$ seconds. After docking, the receiver aircraft and the drogue are constrained to move together in the simulation.

The weighting matrices used to calculate the observer gain are

$$Q_o = \begin{bmatrix} Q_{o_1} & 0 & 0 & 0 \\ 0 & Q_{o_2} & 0 & 0 \\ 0 & 0 & Q_{o_3} & 0 \\ 0 & 0 & 0 & Q_{o_4} \end{bmatrix} \quad R_o = \begin{bmatrix} 0.1 & 0 & 0 \\ 0 & 0.1 & 0 \\ 0 & 0 & 0.1 \end{bmatrix} \tag{7.2}$$

where

$$Q_{o_1} = 0.1 \begin{bmatrix} 1 & 0 & 0 \\ 0 & 1 & 0 \\ 0 & 0 & 1 \end{bmatrix} \quad Q_{o_3} = 0.001 \begin{bmatrix} 1 & 0 & 0 & 0 \\ 0 & 1 & 0 & 0 \\ 0 & 0 & 1 & 0 \\ 0 & 0 & 0 & 1 \end{bmatrix} \quad Q_{o_4} = \begin{bmatrix} 1 & 0 & 0 & 0 \\ 0 & 1 & 0 & 0 \\ 0 & 0 & 1 & 0 \\ 0 & 0 & 0 & 1 \end{bmatrix}$$

and $Q_{o_2} \in \Re^{9\times 9} \equiv 0$ array of zeros. The weighting matrices for the controller gain are

$$Q = \begin{bmatrix} Q_1 & 0 \\ 0 & Q_2 \end{bmatrix} \quad R = \begin{bmatrix} 1 & 0 & 0 & 0 \\ 0 & 1 & 0 & 0 \\ 0 & 0 & 1 & 0 \\ 0 & 0 & 0 & 1 \end{bmatrix} \tag{7.3}$$

where

$$Q_1 = 10000 \begin{bmatrix} 1 & 0 & 0 \\ 0 & 1 & 0 \\ 0 & 0 & 1 \end{bmatrix} \quad Q_2 = 100 I_{13} \tag{7.4}$$

and $I_{13} \in \Re^{13\times 13} \equiv 1$ is the identity matrix.

C. Kalman Filter Tuning Criteria

The tuning parameters q_1 and q_2 (see Section C of Chapter IV), are selected for each case to give the best performance of the Kalman filter, defined by

1. The degree to which the relative position and orientation estimation errors fit closely inside the Kalman filter $3-\sigma$ bounds (see Fig. 14).

2. The ability of the estimate to track realistic variations in the relative position and orientation for each value of turbulence intensity.

D. Evaluation of Closed-loop Performance with Combined VisNav and Kalman Filter

The performance of the Kalman filter in combination with VisNav for autonomous aerial refueling is evaluated through a series of simulations with and without the Kalman filter in the loop. The location of the Kalman filter in the ROTC/VisNav structure is shown in Fig. 29. The docking scenario described in Section A is run 30 times with the Kalman filter and 30 times without the Kalman filter for each level of turbulence intensity from Table VII. The measures of merit for each simulation are the docking success and the final docking error.

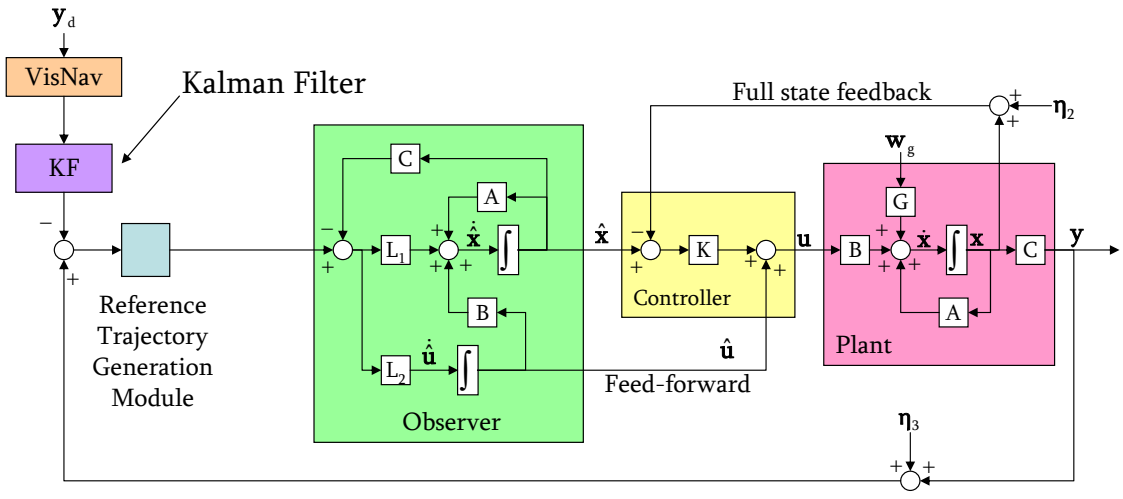

Fig. 29. Kalman filter placement in ROTC block diagram

CHAPTER VIII

NUMERICAL EXAMPLES

This chapter presents the results of several docking scenarios performed with the autonomous aerial refueling simulation described in Chapter VI. Sections A through D present four cases that are used to tune the Kalman filter for various levels of turbulence intensity. The first tuning case is a docking maneuver in the absence of turbulence. Case 2 illustrates docking performance in Dryden light turbulence, and case 3 presents results for Dryden moderate turbulence. The final case illustrates docking performance in severe turbulence. Sections E presents results of simulations with the tuned Kalman filter in the control loop. Section F gives a summary of all results.

A. Tuning Case 1: No Turbulence

Case 1 simulates an autonomous aerial refueling scenario in the absence of turbulence, with $\sigma_u = \sigma_v = \sigma_w = 0$. The two stages of the receiver aircraft trajectory and the trajectory of the drogue are illustrated in Fig. 30. The first stage of the receiver aircraft maneuver, the initial alignment phase, is shown in blue. The second stage, when the receiver aircraft tracks the drogue movement using measurements from the VisNav sensor, is shown in red. The path of the drogue is shown in green. It can be seen that the drogue movement is relatively small compared to that of the receiver aircraft.

Fig. 31 shows the drogue's inertial position and velocity relative to the steady-state flight path of the receiver aircraft. Because the drogue is given a small initial velocity, it oscillates in the $Y_N - Z_N$ plane, moving about 3 feet in each direction. When docking is achieved after approximately 46 seconds, the probe of the receiver

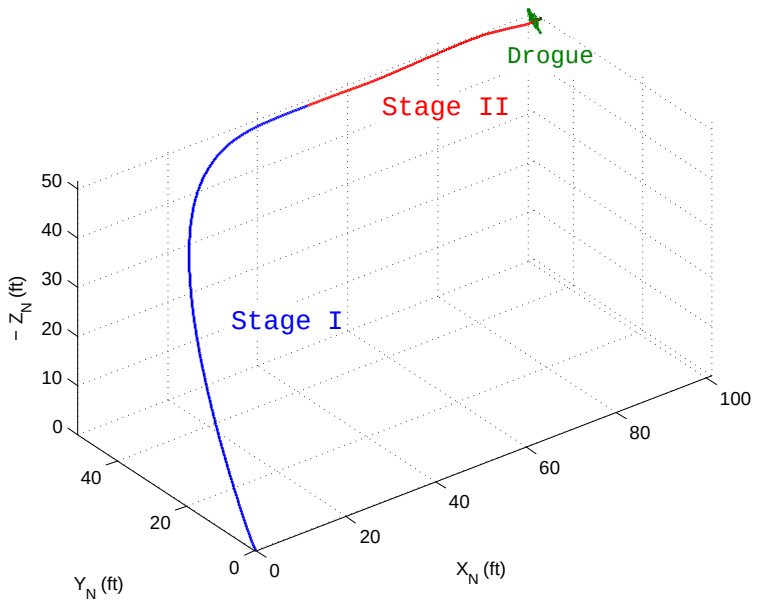

Fig. 30. Receiver aircraft and drogue trajectories (case 1, no turbulence)

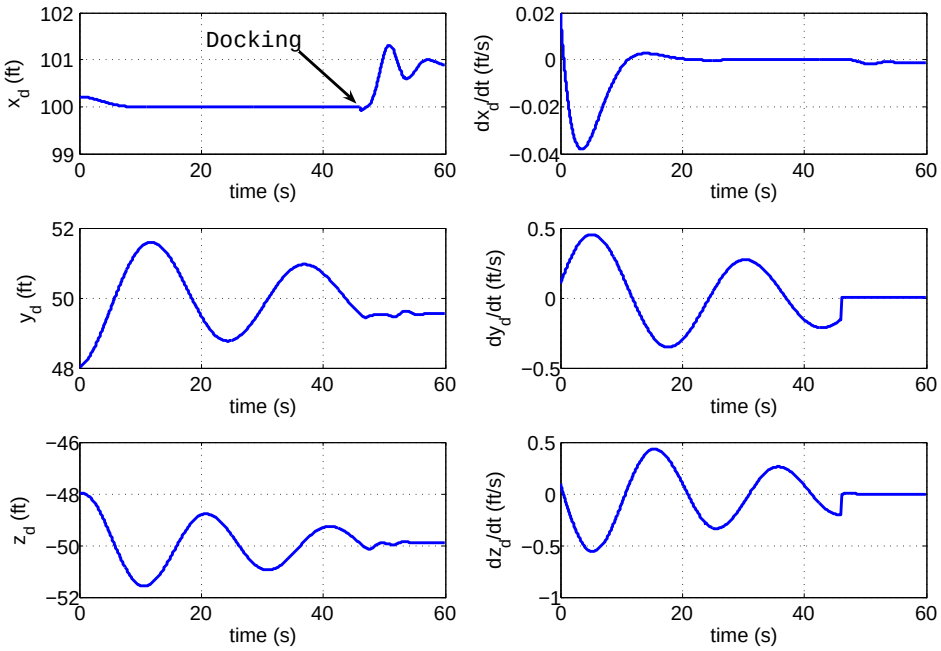

Fig. 31. Drogue position and velocity (case 1, no turbulence)

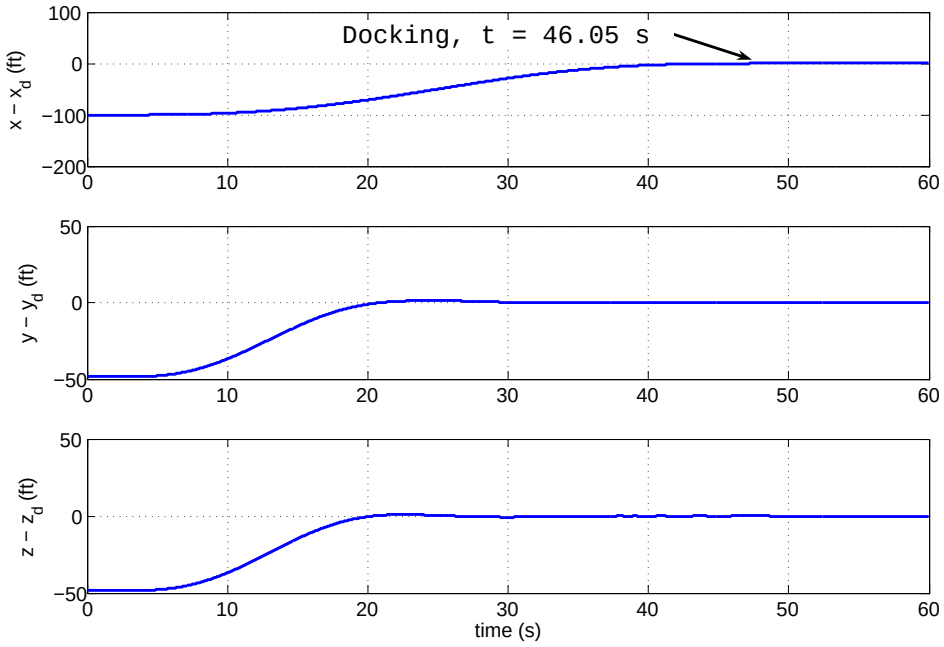

Fig. 32. Tracking error (case 1, no turbulence)

aircraft pushes into the drogue, causing it to move about 1 foot in the X_N direction.

Fig. 32 shows the tracking error between the receiver and the drogue over the entire maneuver. Successful docking is achieved at $t = 46.05$ seconds, with a docking error of less than 1 inch. Docking is achieved sooner than the projected docking time of $t_f = 50$ seconds. The difference is due to the fact that the reference trajectory is based only on the initial constant offset between the receiver aircraft and the drogue, and does not take into account the fact that the drogue moves from its initial position during the maneuver. The controller has no trouble tracking the movements, however, even with noisy measurements from the VisNav sensor.

The receiver aircraft states are shown in Fig. 33. The inertial coordinates x, y, and z each converge to the position of the drogue. The z coordinate is negative, indicating an increase in altitude because the inertial axis is defined with Z_N pointing down, or in the direction of gravity. The pitch attitude angle Θ increases from its

steady-state value by about half of a degree as the receiver aircraft climbs 50 feet. The bank angle Φ shows that the aircraft banks to align itself during the first stage of the maneuver. After $t = 25$ seconds, the second stage of the maneuver begins. During the second stage the body-axis velocities and angular rates increase due to the noisy measurements from the VisNav sensor. It can be seen that deviations from the steady-state values for all of the states are small. This is desirable because large excursions of the aircraft states are an indication that the linear model may no longer be valid.

The receiver control inputs are presented in Fig. 34. During the alignment phase in the first 25 seconds of the maneuver, the control inputs are low in magnitude and frequency. The aileron (δ_a) and rudder (δ_r) have small defections during the first few seconds of Stage I, when the receiver aircraft aligns itself laterally with the drogue. The elevator (δ_e) inputs during the first stage are more drawn out, lasting the full duration of the first stage. The throttle setting (δ_T) increases by about 2% during the first stage to maintain speed during the climb. When the second stage begins after 25 seconds, the control inputs increase in frequency as the controller tracks the drogue using measurements from VisNav. The control inputs that occurr after 46 seconds happen because the control law is modified after docking so that the receiver and the drogue move together. This is done only for simulation purposes; in reality physical constraints would keep the two systems together. The receiver control positions and rates remain well below the limits specified in Table V throughout the docking maneuver. The aileron control surface has the highest rate, about 10 deg/s, which is well below the 100 deg/s limit. Consideration of the control rate limits is particularly imporant because of pilot-induced osciallation, an instability which occurrs when a pilot or flight control system demand unachievable control rates.

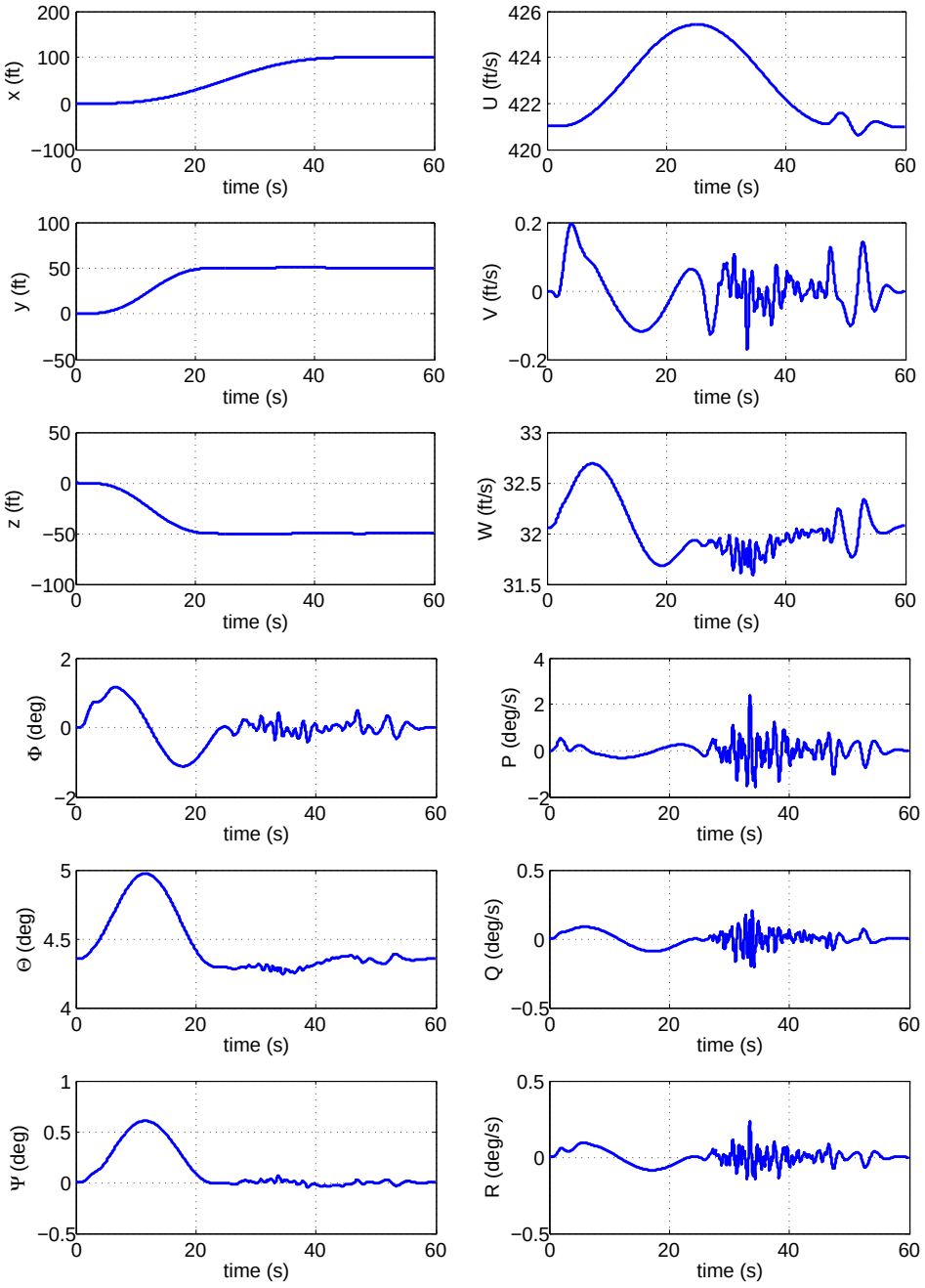

Fig. 33. Receiver aircraft states (case 1, no turbulence)

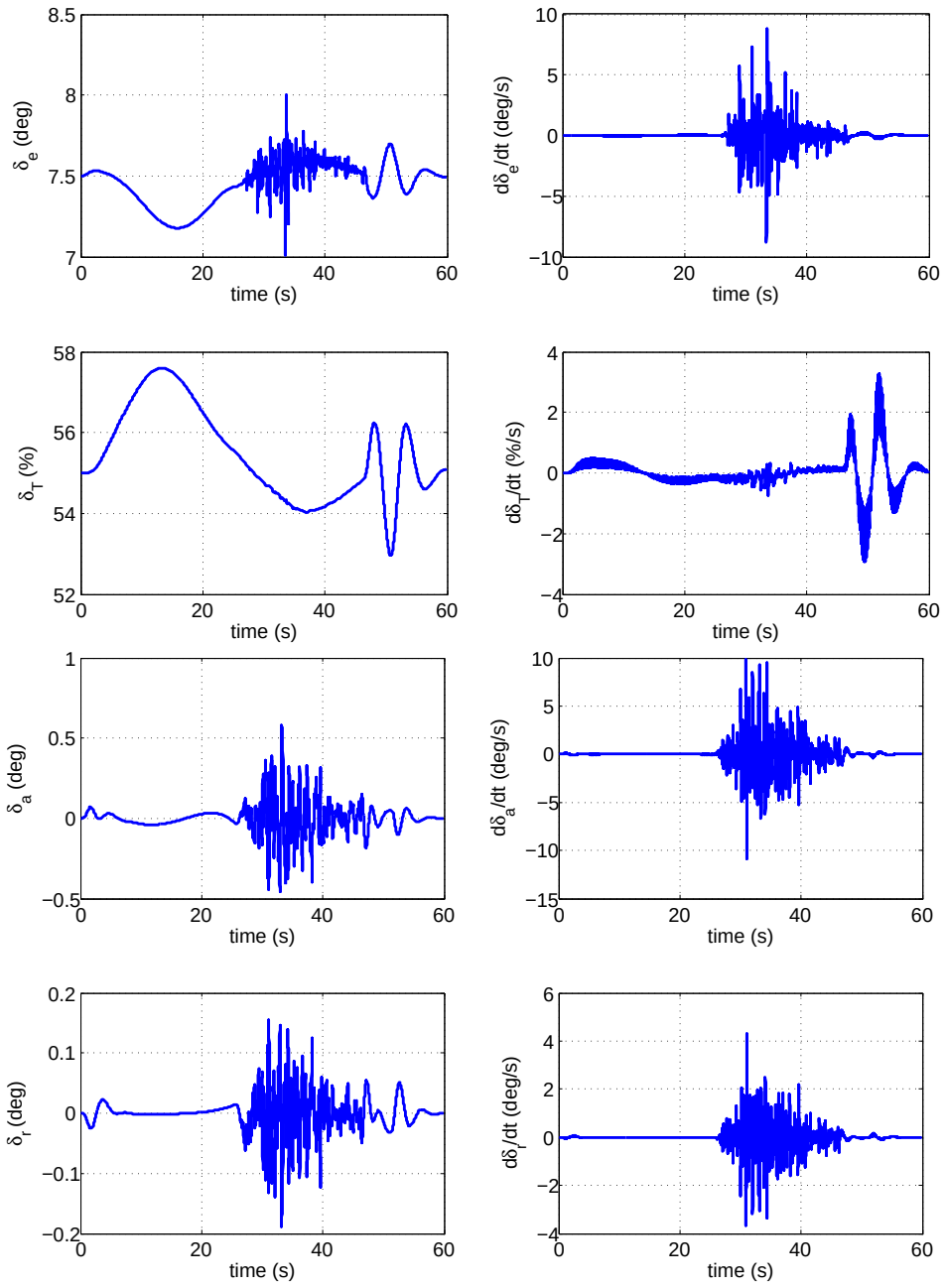

Fig. 34. Receiver aircraft controls and control rates (case 1, no turbulence)

Fig. 35 shows the error in the navigation solution from VisNav, along with the 3σ bounds from the GLSDC algorithm. The initial estimation error begins at about 3 ft in position, and converges to zero as the sensor moves closer to the beacon array, and more measurements are taken. By the time measurements from VisNav are used in the control law at $t = 25$, the position estimate is within 1 ft of the true value. Noise from the sensor shows up at a frequency of 100 Hz, which is the rate at which GLSDC produces and updated estimate. No beacons drop out of the field of view during the maneuver.

The Kalman filter was tuned using the simulation results discussed above. The values of the tuning parameters which give the best fit are

$$\begin{aligned} q_1 &= 1 \\ q_2 &= 0.01 \end{aligned}$$

The tuned Kalman filter results are shown in Fig. 36. The Kalman filter decreases both the magnitude and the frequency of the estimation error from VisNav. It takes about 10 seconds for the Kalman filter estimation error to converge within the 3σ bounds. Compared to GLSDC alone, the estimation error in position is reduced by almost half. A direct comparison of the estimation error is shown in Fig. 37.

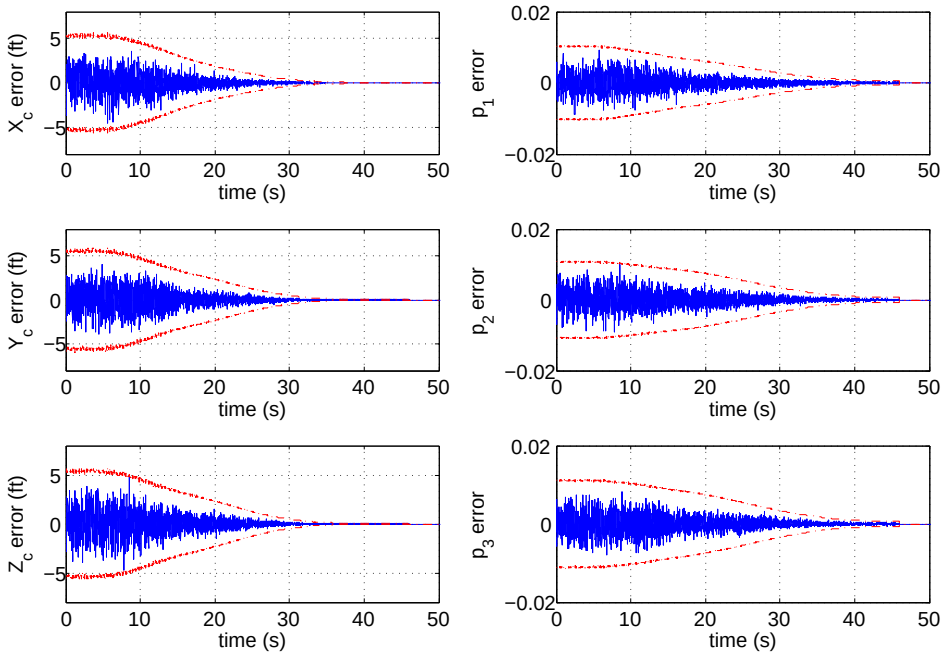

Fig. 35. VisNav error and 3σ bounds from GLSDC (case 1, no turbulence)

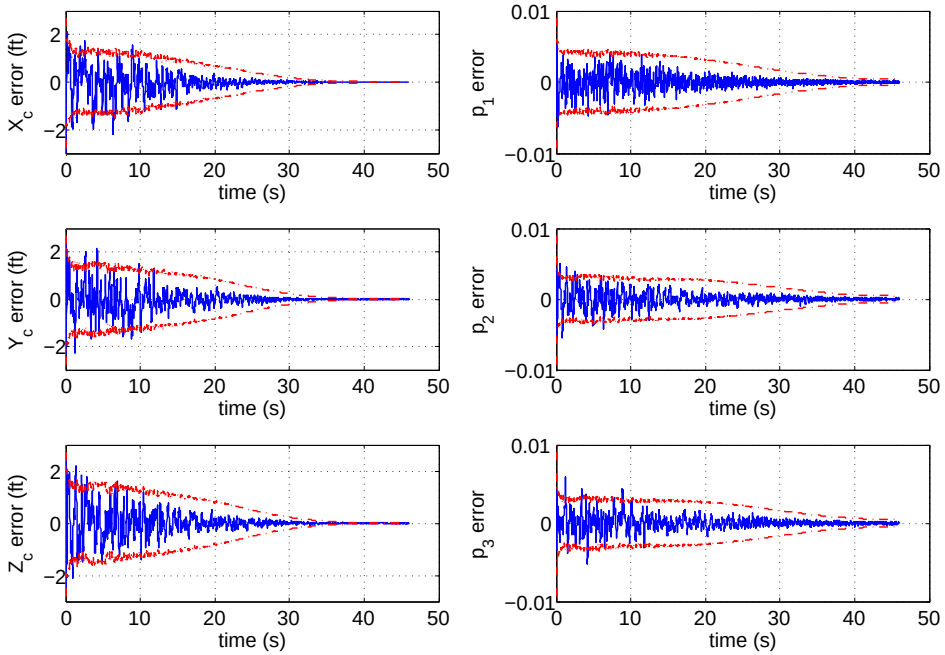

Fig. 36. Tuned Kalman filter error and 3σ bounds (case 1, no turbulence)

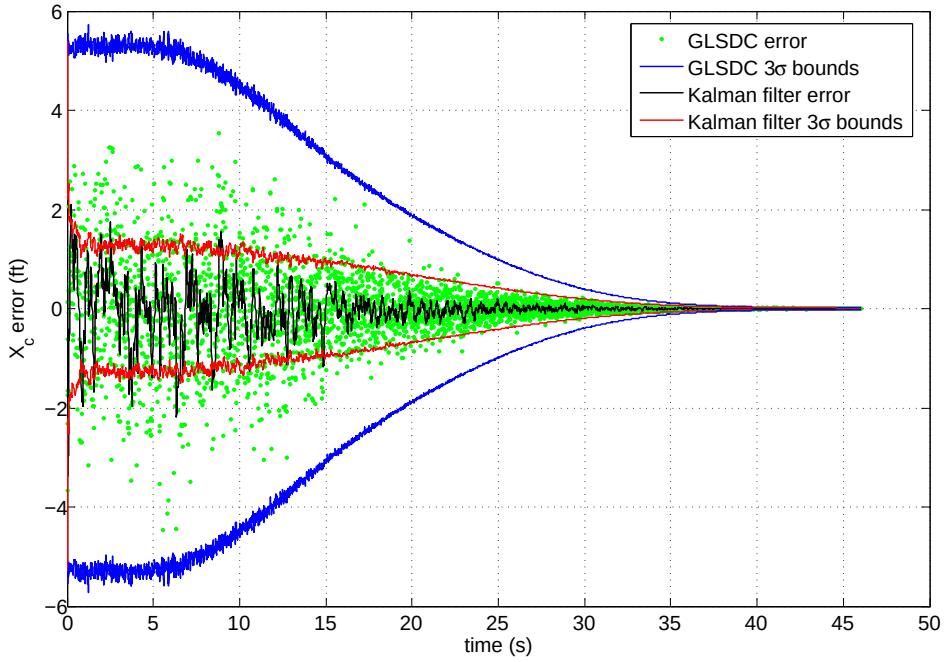

Fig. 37. Comparison of Kalman filter and GLSDC errors (case 1, no turbulence)

B. Tuning Case 2: Light Turbulence

Case 2 simulates an autonomous aerial refueling scenario in light turbulence, with turbulence intensity $\sigma_u = \sigma_v = \sigma_w = 1$ ft/s true airspeed (TAS). The two stages of the receiver aircraft trajectory and the trajectory of the drogue are illustrated in Fig. 38. The first stage of the receiver aircraft maneuver, the initial alignment phase, is shown in blue. The second stage, when the receiver aircraft tracks the drogue movement using measurements from the VisNav sensor, is shown in red. The path of the drogue is shown in green. As in case 1, the drogue movement is relatively small compared to that of the receiver aircraft.

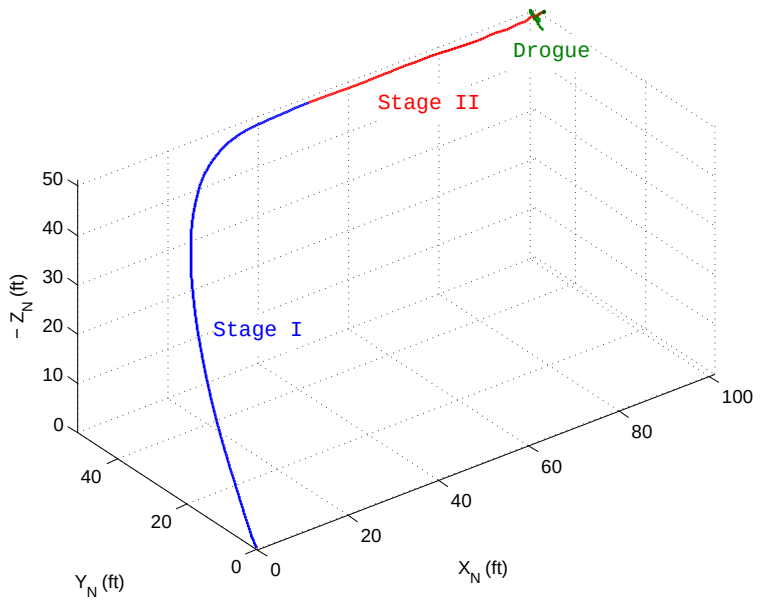

Fig. 38. Receiver aircraft and drogue trajectories (case 2, light turbulence)

Fig. 31 shows the drogue's inertial position and velocity relative to the steady-state flight path of the receiver aircraft. The drogue is given a small initial velocity so that it oscillates in the $Y_N - Z_N$ plane, moving about 3 feet in each direction. When docking is achieved after about 47 seconds, the probe of the receiver aircraft

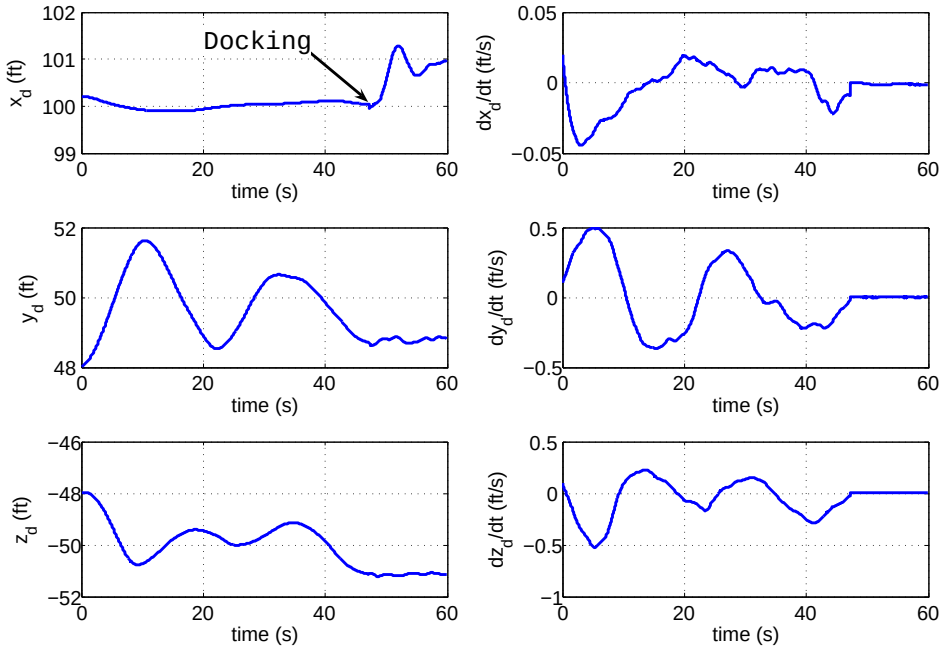

Fig. 39. Drogue position and velocity (case 2, light turbulence)

pushes into the drogue, causing it to move about 1 foot in the X_N direction. The disturbances due to light turbulence may be seen in the velocity time histories of the drogue on the right hand side of Fig. 39. The light turbulence, however, does not significantly change the overall behavior of the drogue compared to case 1.

Fig. 40 shows the tracking error between the receiver and the drogue over the entire maneuver. Successful docking is achieved at $t = 47.13$ seconds, with a docking error of less than 1 inch. Docking is achieved sooner than the projected time of $t_f = 50$ seconds which was used to design the reference trajectory. As in case 1, the difference is due to the fact that the reference trajectory does not take into account the fact that the drogue moves from its initial position during the maneuver. The controller is able to track the drogue movements and achieve a successful docking within the specified design time.

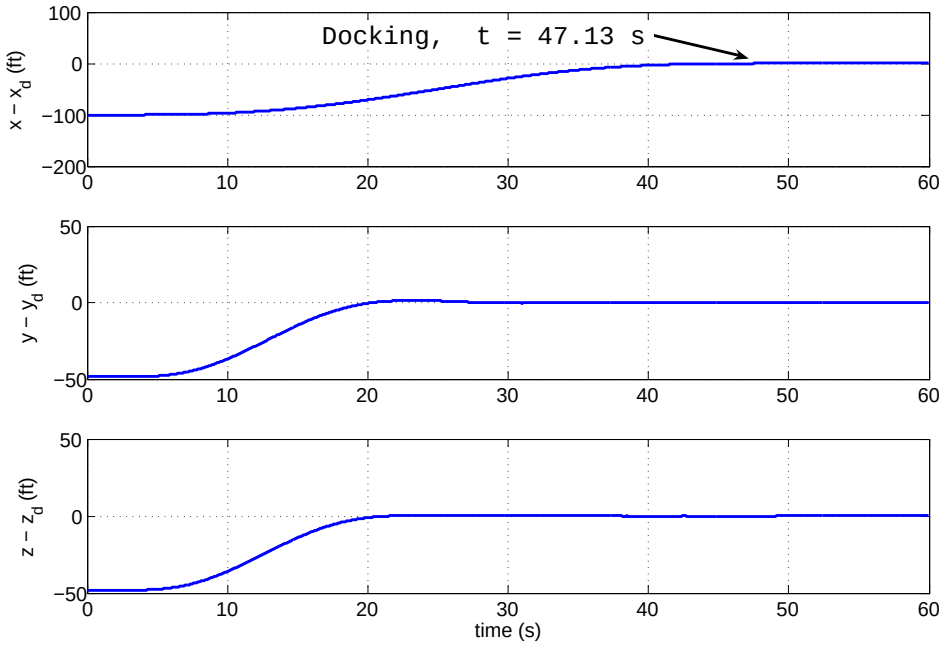

Fig. 40. Tracking error (case 2, light turbulence)

The receiver aircraft states are plotted in in Fig. 41. The inertial coordinates x, y, and z each converge to the position of the drogue. The z coordinate is negative, indicating an increase in altitude because the inertial axis is defined with Z_N pointing down, or in the direction of gravity. The pitch attitude angle Θ increases from its steady-state value by about half of a degree as the receiver aircraft climbs 50 feet. The bank angle Φ shows that the aircraft banks to align itself during the first stage of the maneuver.

After $t = 25$ seconds, the second stage of the maneuver begins. During the second stage the body-axis velocities and angular rates increase due to the noisy measurements from the VisNav sensor. The angular rates, roll rate P in particular, increase slightly from case 1, with no turbulence. It can be seen that deviations from the steady-state values for all of the states are small for the light turbulence case.

The receiver control inputs are presented in Fig. 42. The effects of light turbulence are visible in the time histories of the controls and control rates. Compared to the case with no turbulence, case 2 has increased control activity, especially during Stage I of the maneuver. The additional inputs represent small corrections and adjustments that the receiver aircraft must make as it is perturbed from the reference trajectory by turbulence. The overall magnitudes and rates of the controls are similar to those in the case with no turbulence. When the second stage begins after 25 seconds, the control inputs increase in magnitude as the receiver aircraft tracks the drogue using measurements from VisNav. The control positions and rates are well below the limits specified in Table V. The aileron control surface has the highest rate, about 15 deg/s, which is well below the limit of 100 deg/s.

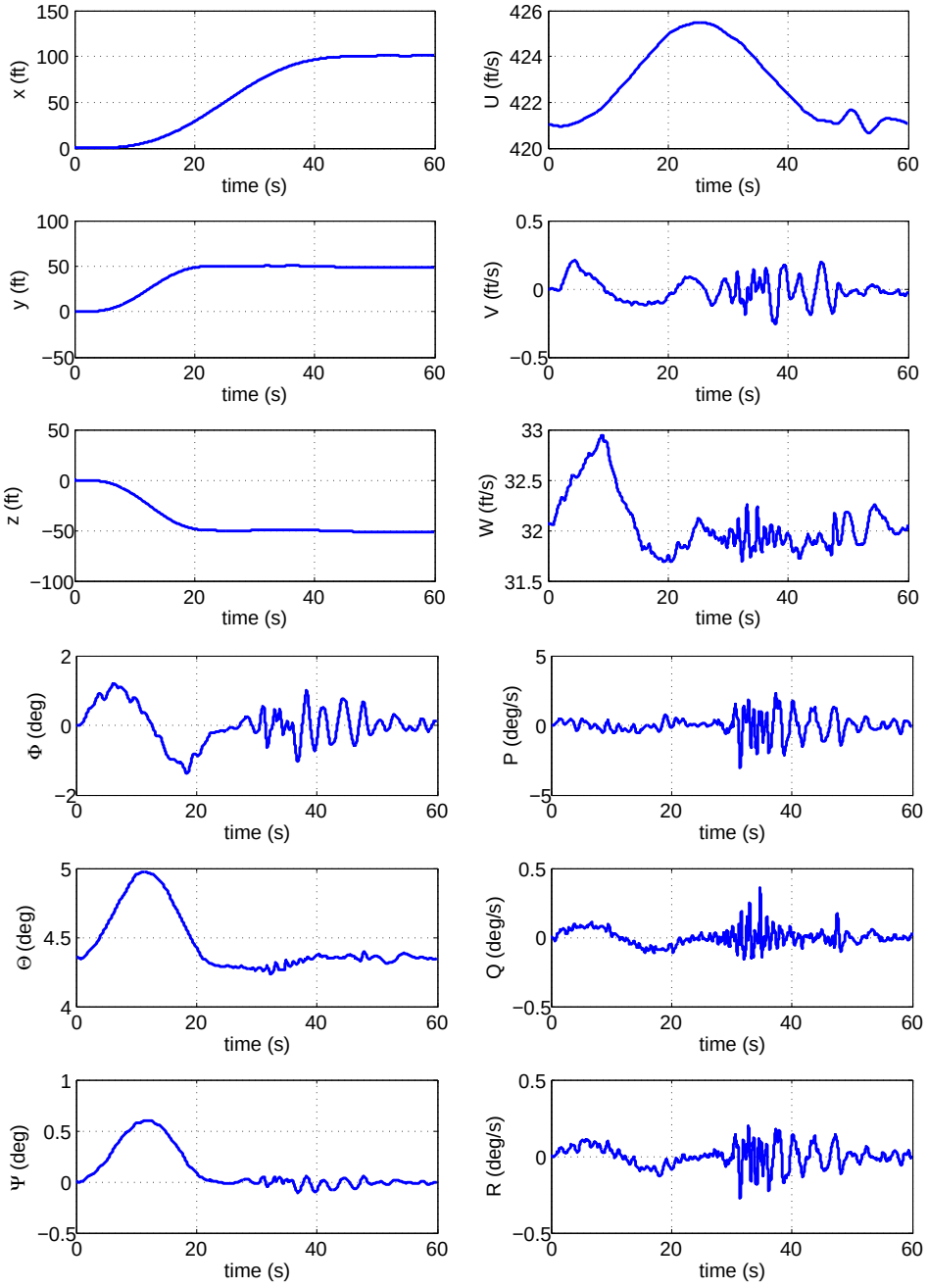

Fig. 41. Receiver aircraft states (case 2, light turbulence)

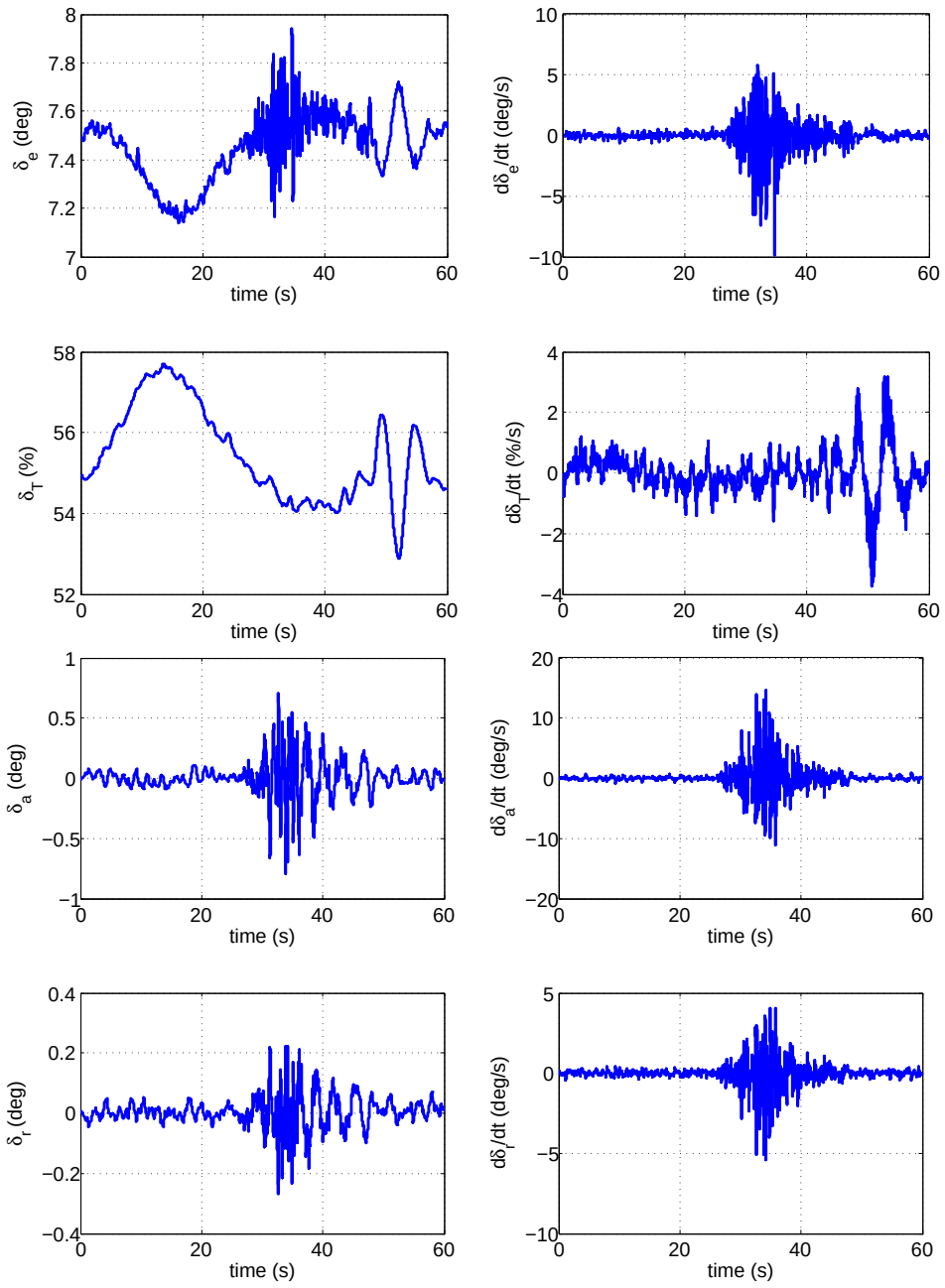

Fig. 42. Receiver aircraft controls and control rates (case 2, light turbulence)

Fig. 43 shows the error in the navigation solution from VisNav, along with the 3σ bounds from the GLSDC algorithm. The initial estimation error begins at about 3 ft in position, and converges to zero as the sensor moves closer to the beacon array, and more measurements are taken. By the time measurements from VisNav are used in the control law at $t = 25$, the position estimate is within 1 ft of the true value. Noise from the sensor shows up at a frequency of 100 Hz, which is the rate at which GLSDC produces and updated estimate. No beacons drop out of the field of view during the maneuver.

The Kalman filter was tuned using the simulation results discussed above. The values of the tuning parameters which give the best fit are

$$\begin{aligned} q_1 &= 1 \\ q_2 &= 0.01 \end{aligned}$$

The tuning parameters are the same as those determined for case 1. The tuned Kalman filter results are shown in Fig. 44. Although there are more places where the estimation error exceeds the 3σ bounds in the first few seconds of case 2, the performance is about the same as case 1 after the solution converges. It takes about 10 seconds for the Kalman filter estimation error to converge within the 3σ bounds. The Kalman filter decreases both the magnitude and the frequency of the estimation error from VisNav. Compared to GLSDC alone, the estimation error in position is reduced by almost half. A direct comparison of the estimation error is shown in Fig. 45.

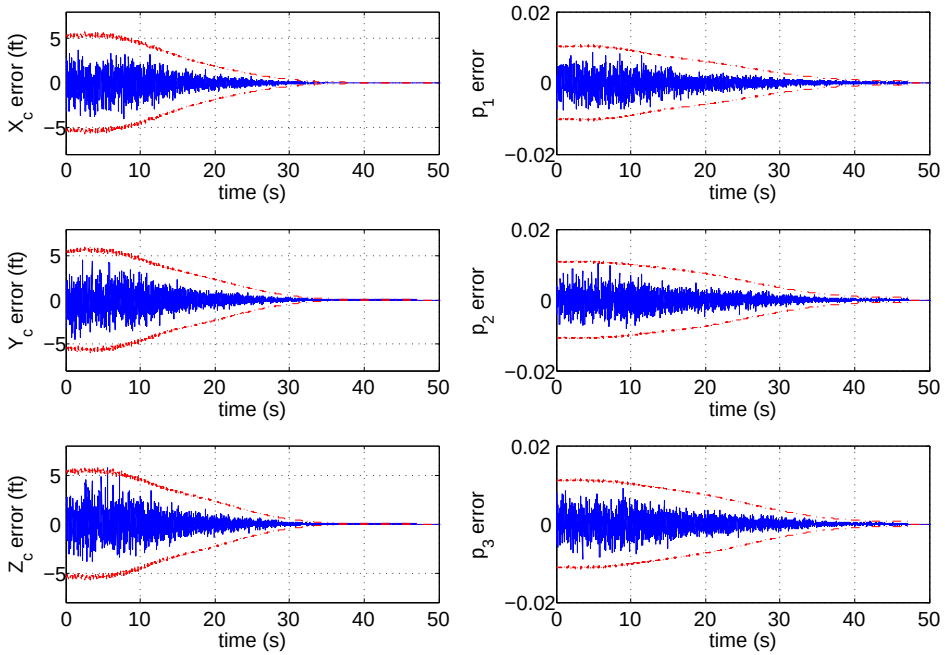

Fig. 43. VisNav error and 3σ bounds from GLSDC (case 2, light turbulence)

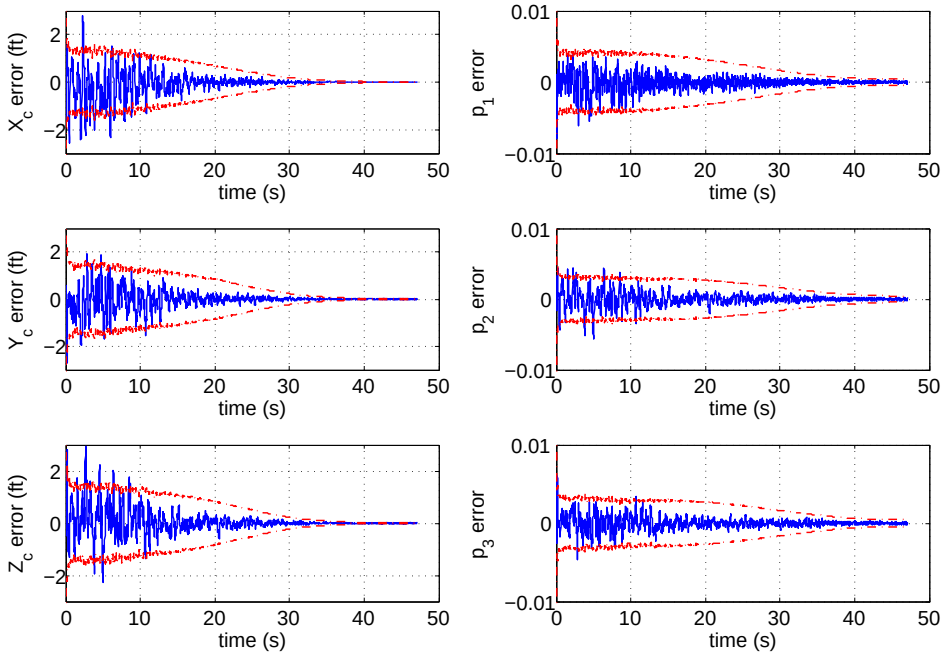

Fig. 44. Tuned Kalman filter error and 3σ bounds (case 2, light turbulence)

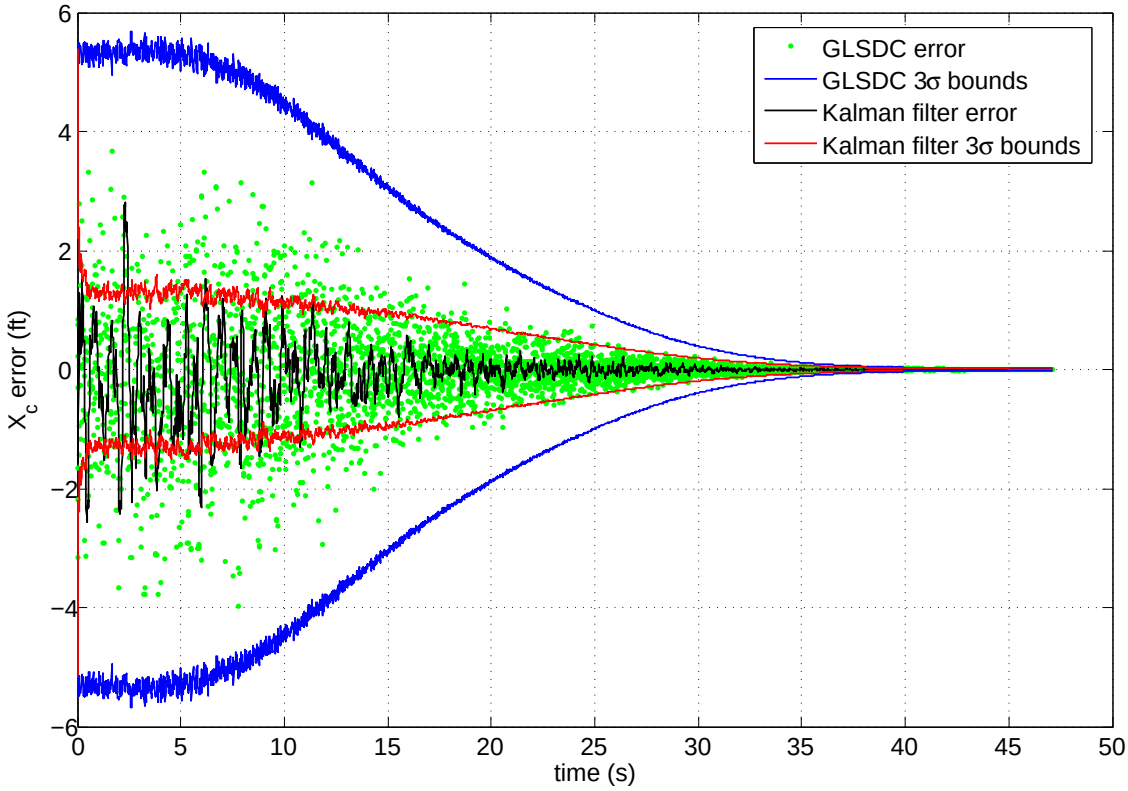

Fig. 45. Comparison of Kalman filter and GLSDC errors (case 2, light turbulence)

C. Tuning Case 3: Moderate Turbulence

Case 3 simulates an autonomous aerial refueling scenario in Dryden moderate turbulence, with turbulence intensity $\sigma_u = \sigma_v = \sigma_w = 5$ ft/s true airspeed (TAS). The two stages of the receiver aircraft trajectory and the trajectory of the drogue are illustrated in Fig. 46. The first stage of the receiver aircraft maneuver, the initial alignment phase, is shown in blue. The second stage, when the receiver aircraft tracks the drogue movement using measurements from the VisNav sensor, is shown in red. The path of the drogue is shown in green. The variation in the position of the drogue is much larger than in previous cases, due to the increased turbulence intensity level.

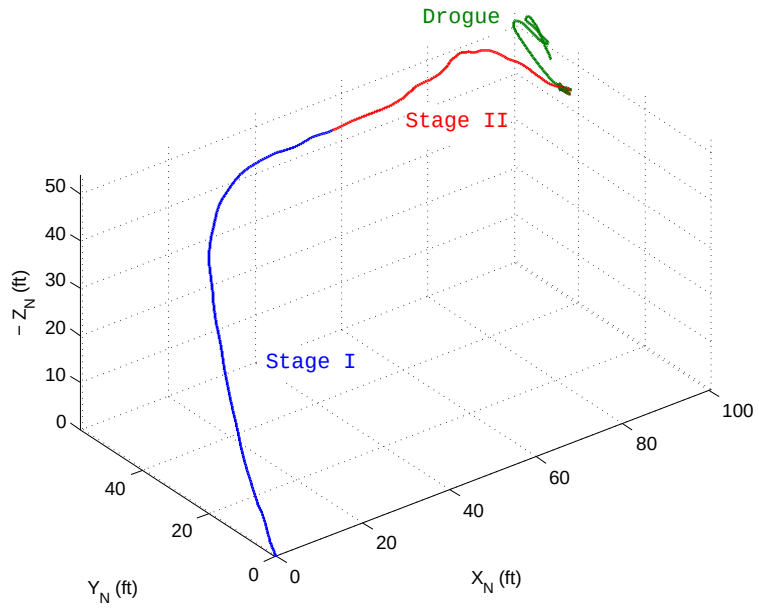

Fig. 46. Receiver aircraft and drogue trajectories (case 3, moderate turbulence)

Fig. 47 shows the drogue's inertial position and velocity relative to the steady-state flight path of the receiver aircraft. The time history of x_d shows that the drogue moves closer to the receiver aircraft as it approaches, resulting in a docking time of about 42 seconds, which is 8 seconds before the projected docking time. When docking is achieved, the probe of the receiver aircraft pushes into the drogue, causing it to move about 6 inches in the X_N direction. The disturbances due to moderate turbulence may be seen in the velocity time histories of the drogue on the right hand side of Fig. 47. The drogue movements are much larger than in cases 1 and 2, but the controller is still able to track the movements and achieve successful docking.

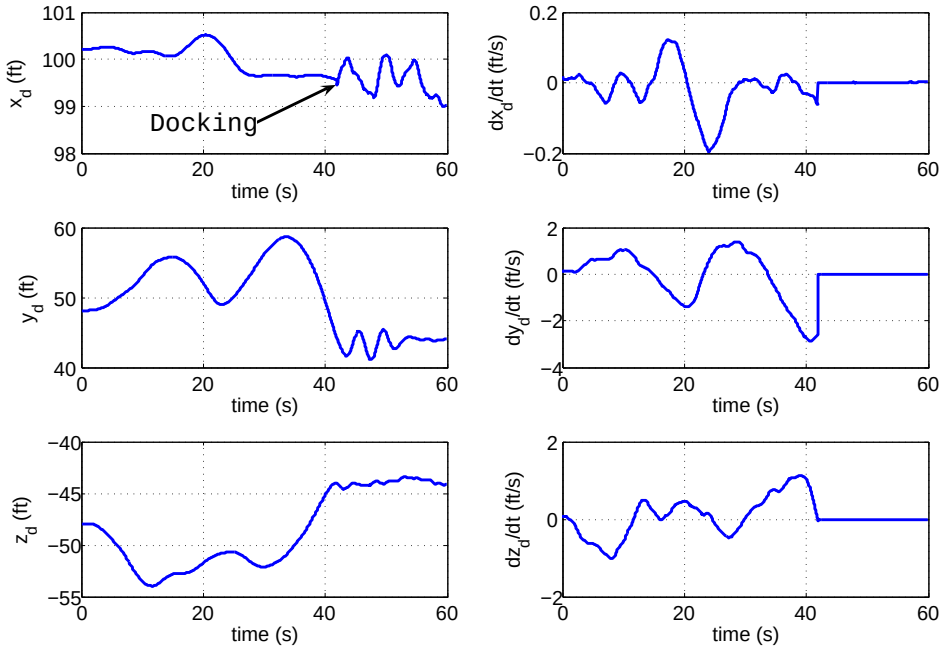

Fig. 47. Drogue position and velocity (case 3, moderate turbulence)

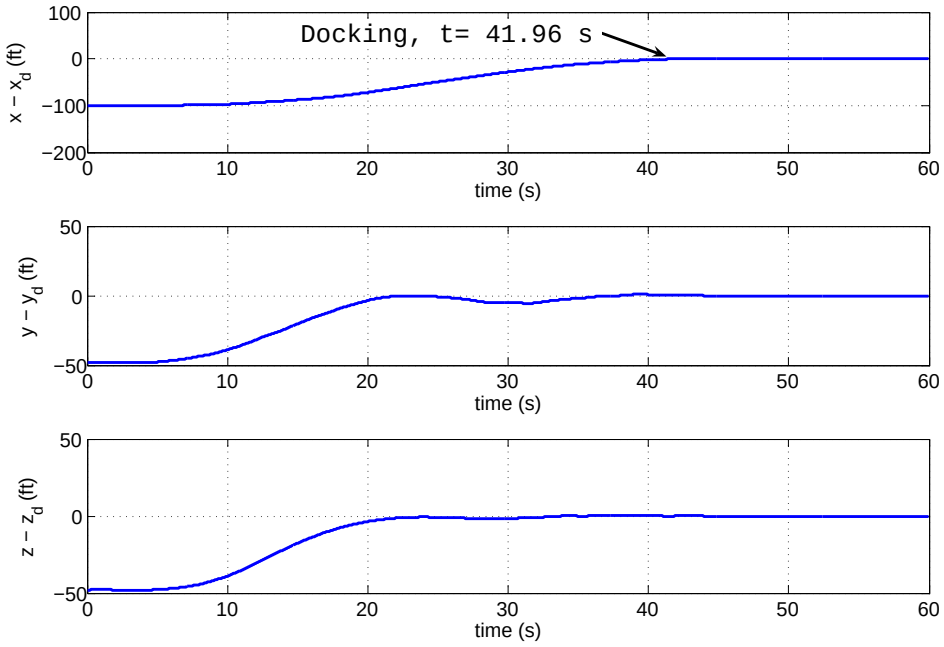

Fig. 48. Tracking error (case 3, moderate turbulence)

Fig. 48 shows the tracking error between the receiver and the drogue over the entire maneuver. Successful docking is achieved at $t = 41.96$ seconds, with a docking error of 2.4 inches.

The receiver aircraft states are plotted in in Fig. 49. The inertial coordinates x, y, and z each converge to the position of the drogue. The effect of moderate turbulence can be seen most clearly in the body axis forward velocity, which has a much smoother time history in cases 1 and 2. The bank angle Φ is much higher in case 3, especially after the docking time of $t = 41.96$ sec. This is due to large aileron inputs that are needed to keep the receiver and the drogue together after docking. Roll rate P and yaw rate R are also much higher in for moderate turbulence. Even in moderate turbulence, however, deviations from the steady-state values for all of the states are small.

The receiver aircraft control inputs are presented in Fig. 50. The effects of moderate turbulence are apparent in the time histories of the controls and control rates. Compared to the case with cases 1 and 2, case 3 has significantly more control activity. The additional inputs represent corrections and adjustments that the receiver aircraft must make as it is perturbed from the reference trajectory. When the second stage begins after 25 seconds, the control inputs increase in magnitude as the receiver aircraft tracks the drogue using measurements from VisNav. The control positions and rates remain well below the limits specified in Table V. Again, the aileron control surface has the highest rate, about 12 deg/s, which is well below the limit of 100 deg/s.

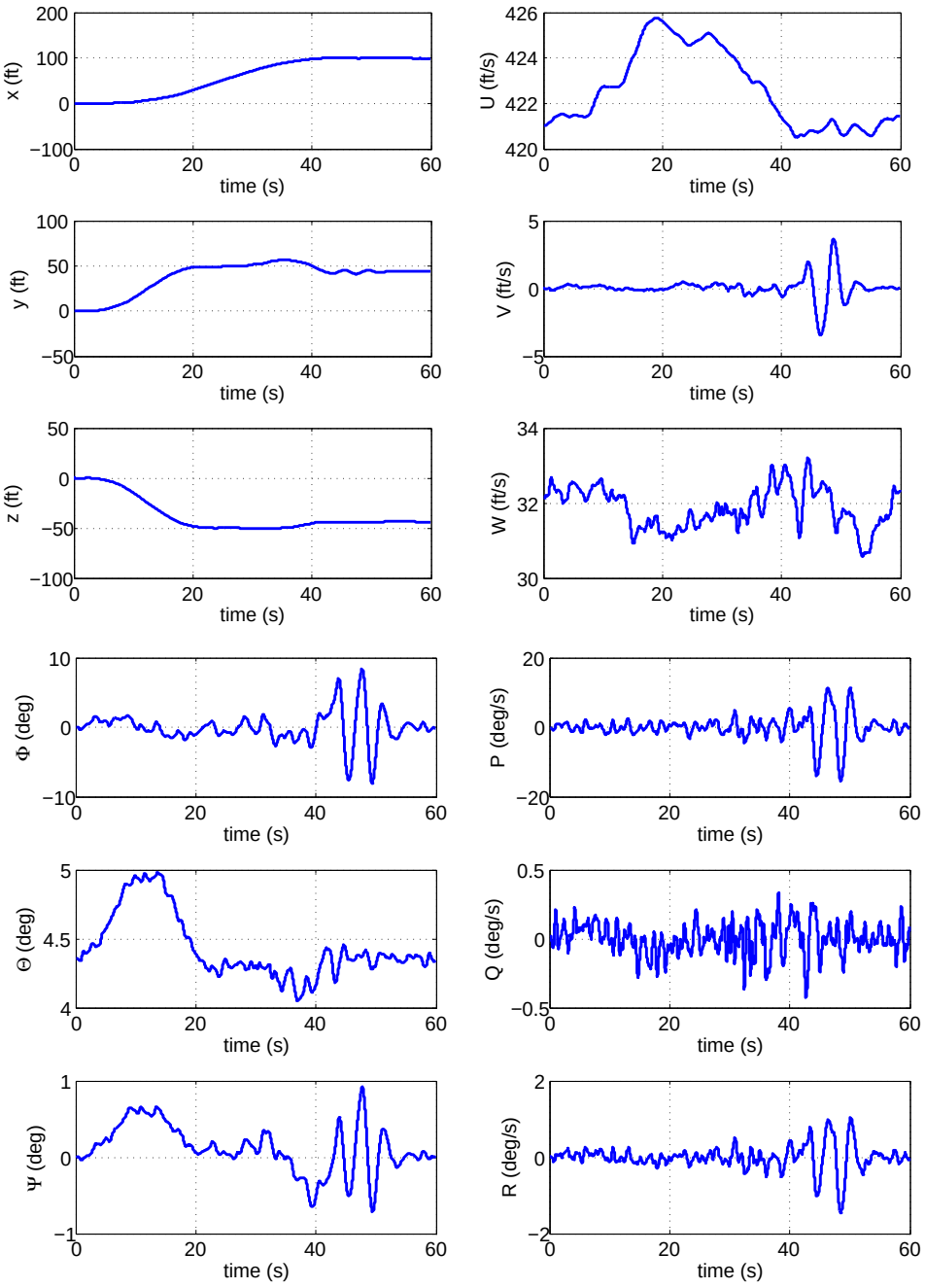

Fig. 49. Receiver aircraft states (case 3, moderate turbulence)

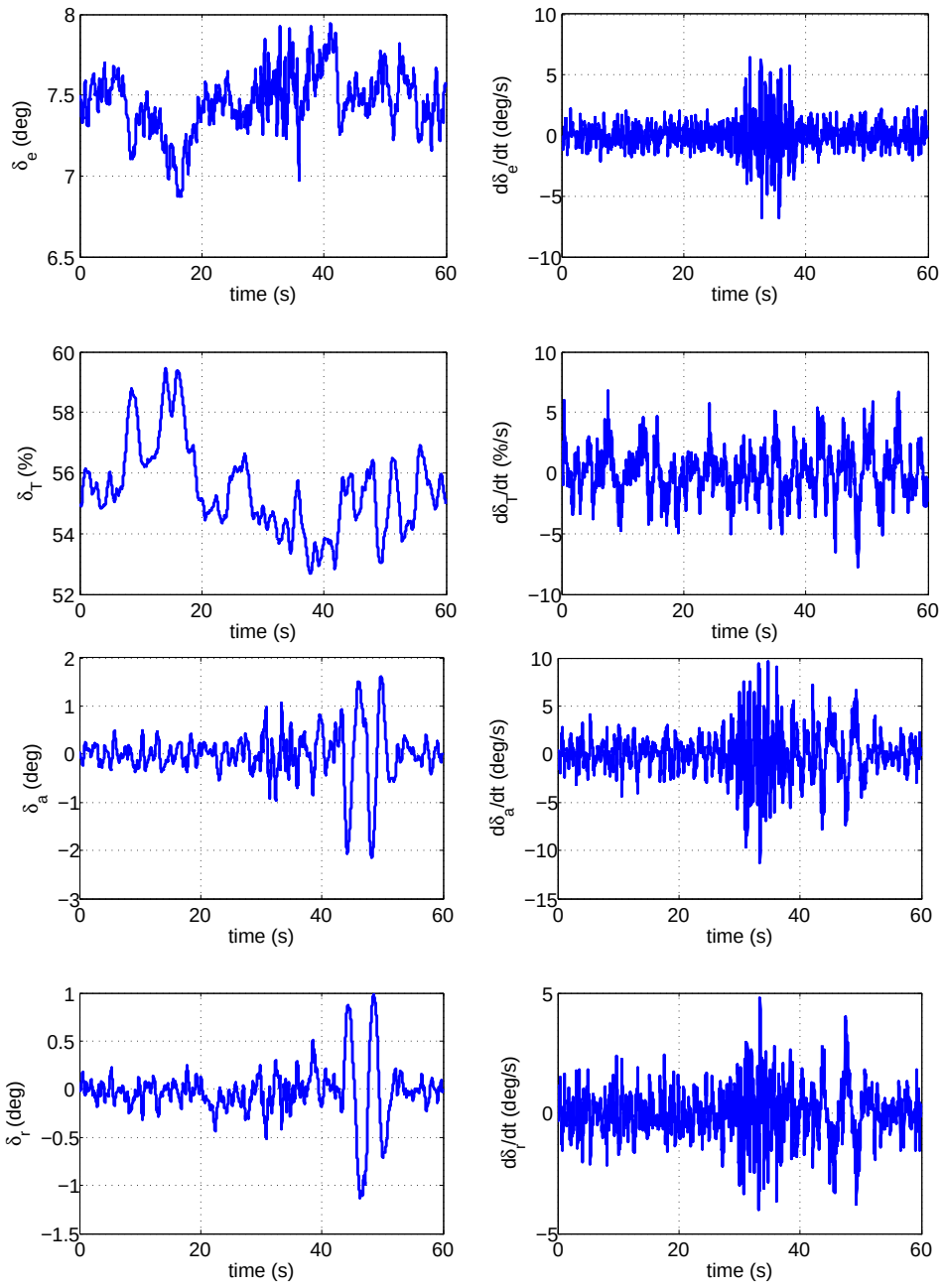

Fig. 50. Receiver aircraft controls and control rates (case 3, moderate turbulence)

Fig. 51 shows the error in the navigation solution from VisNav, along with the 3σ bounds from the GLSDC algorithm. The initial estimation error begins at about 3 ft in position, and converges to zero as the sensor moves closer to the beacon array, and more measurements are taken. By the time measurements from VisNav are used in the control law at $t = 25$, the position estimate is within 1 ft of the true value. Noise from the sensor shows up at a frequency of 100 Hz, which is the rate at which GLSDC produces and updated estimate. No beacons drop out of the field of view during the maneuver.

The Kalman filter was tuned using the simulation results discussed above. The values of the tuning parameters which give the best fit are

$$\begin{aligned} q_1 &= 1 \\ q_2 &= 0.01 \end{aligned}$$

The tuning parameters are the same as those determined for cases 1 and 2. The tuned Kalman filter results are shown in Fig. 52. Although there are more places where the estimation error exceeds the 3σ bounds in the first few seconds of case 3, the performance is about the same as cases 1 and 2 after the solution converges. It takes about 10 seconds for the Kalman filter estimation error to converge within the 3σ bounds. The Kalman filter decreases both the magnitude and the frequency of the estimation error from VisNav. Compared to GLSDC alone, the estimation error in position is reduced by almost half. A direct comparison of the estimation error is shown in Fig. 53.

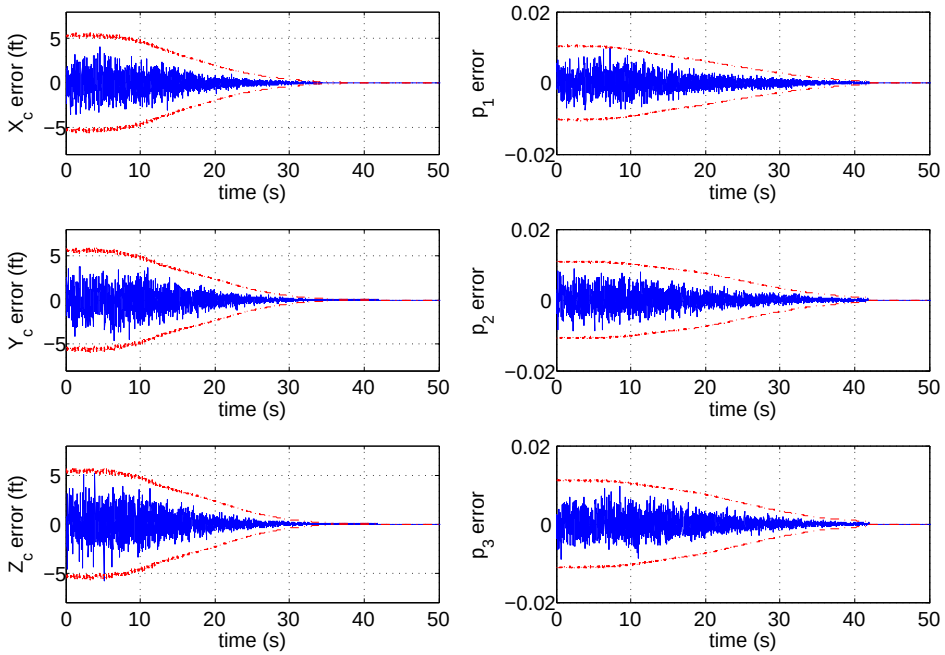

Fig. 51. VisNav error and 3σ bounds from GLSDC (case 3, moderate turbulence)

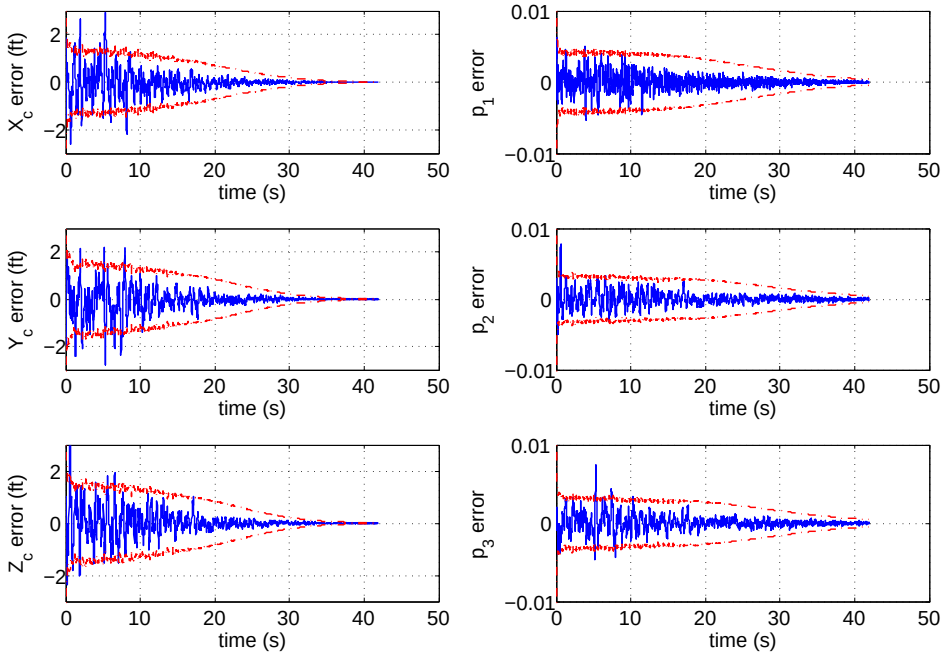

Fig. 52. Tuned Kalman filter error and 3σ bounds (case 3, moderate turbulence)

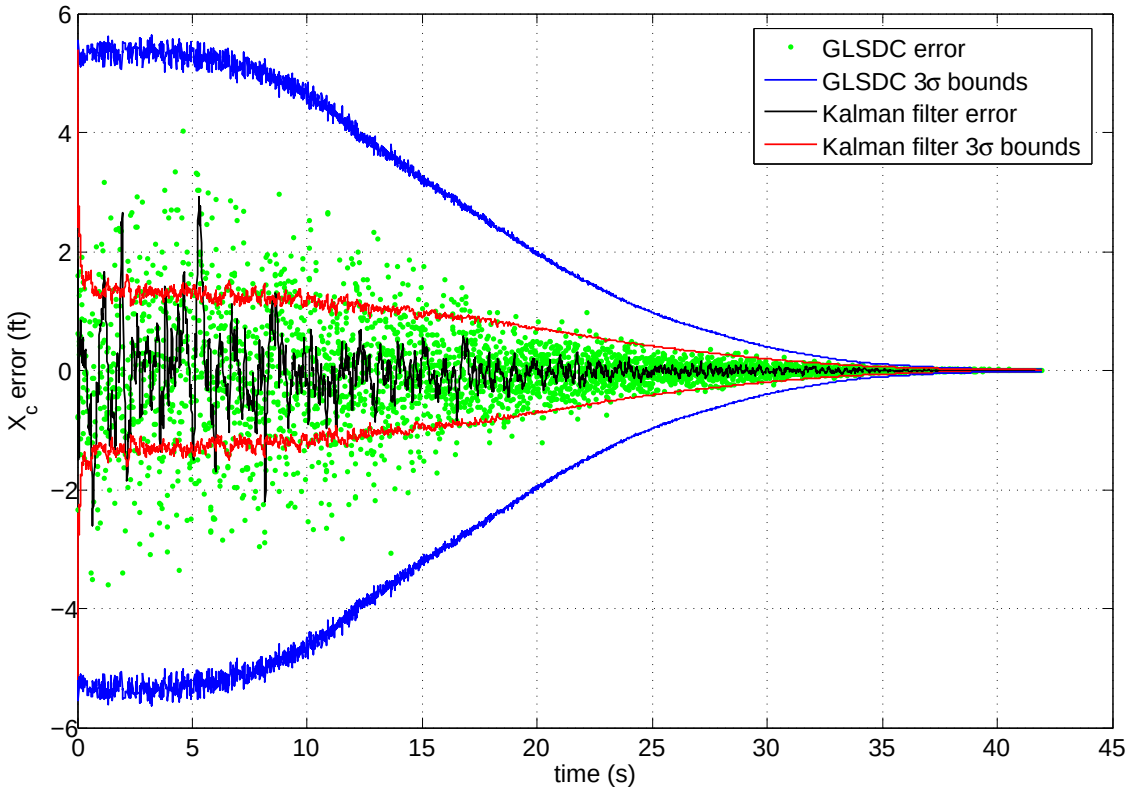

Fig. 53. Comparison of Kalman filter and GLSDC errors (case 3, moderate turbulence)

D. Tuning Case 4: Severe Turbulence

Case 4 simulates an autonomous aerial refueling scenario in severe turbulence, with turbulence intensity $\sigma_u = \sigma_v = \sigma_w = 10$ ft/s true airspeed (TAS) ft/s. The two stages of the receiver aircraft trajectory and the trajectory of the drogue are illustrated in Fig. 54. The first stage of the receiver aircraft maneuver, the initial alignment phase, is shown in blue. The second stage, when the receiver aircraft tracks the drogue movement using measurements from the VisNav sensor, is shown in red. The path of the drogue is shown in green. The variation in the position of the drogue is much larger than in previous cases due to the increased turbulence intensity level.

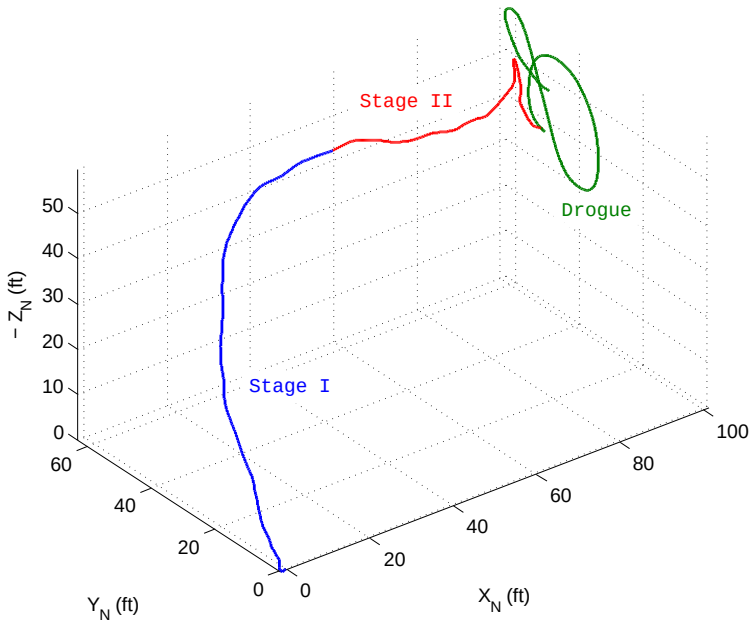

Fig. 54. Receiver aircraft and drogue trajectories (case 4, severe turbulence)

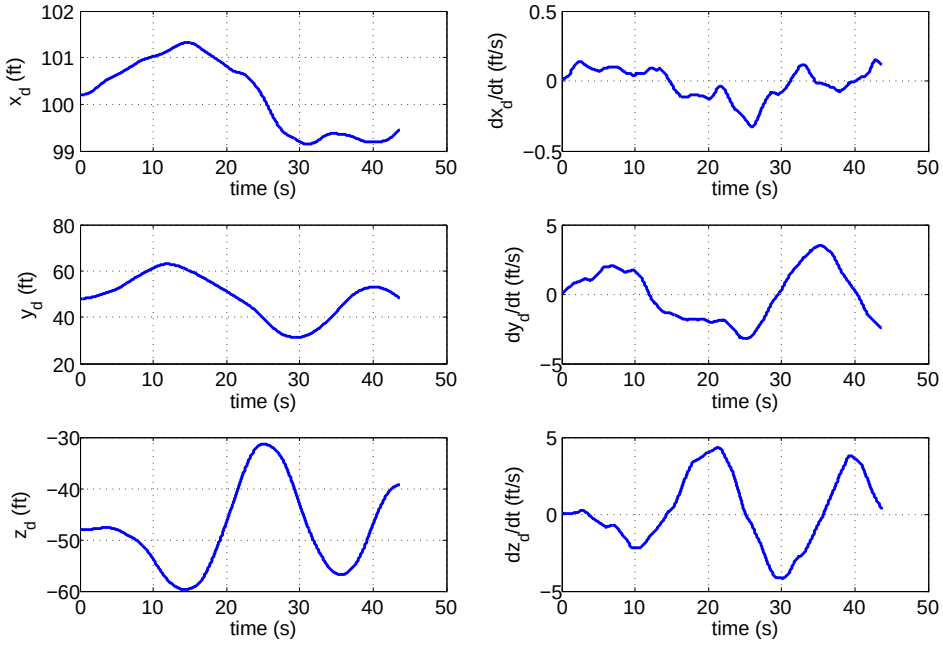

Fig. 55. Drogue position and velocity (case 4, severe turbulence)

Fig. 55 shows the drogue's inertial position and velocity relative to the steady-state flight path of the receiver aircraft. The drogue moves about 30 feet vertically and laterally during the maneuver with much larger oscillations than in the previous cases. It is noted that piloted refueling under these conditions would not be attempted according to established criteria for manned probe and drogue refueling [42]. The disturbances due to severe turbulence may be seen in the velocity time histories of the drogue on the right hand side of Fig. 55. The simulation is stopped after the receiver aircraft's probe tip passes the drogue without docking at around $t = 44$ seconds.

Fig. 56 shows the tracking error between the receiver and the drogue over the entire maneuver. The docking error is 0.75 feet, or about 9 inches. Although this value is larger than the requirement for successful docking defined in Chapter VII, the

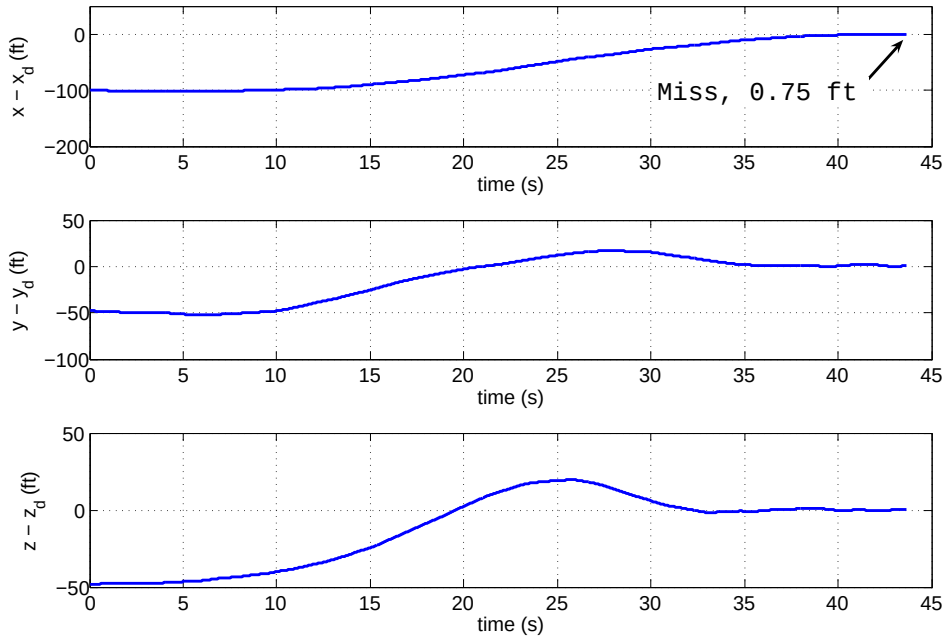

Fig. 56. Tracking error (case 4, severe turbulence)

docking performance is very good considering the aircraft and drogue are experiencing severe turbulence.

The receiver aircraft states are plotted in in Fig. 57. The effects of severe turbulence can be seen most clearly all of the states. The magnitude of the control inputs for overcoming the turbulence and for tracking the drogue is about the same, making it difficult to see the difference between Stage I and Stage II of the maneuver. The body-axis velocities U, V, and W, and the angular rates P, Q, and R are larger than previous cases, deviations from the steady-state values remain within acceptable values.

The receiver aircraft control inputs are presented in Fig. 58. The effects of severe turbulence are apparent in the time histories of the controls and control rates. Case 4 has the most control activity and the highest control rates of all the cases. The aileron control surface has the highest rate, about 15 deg/s, which is still well below

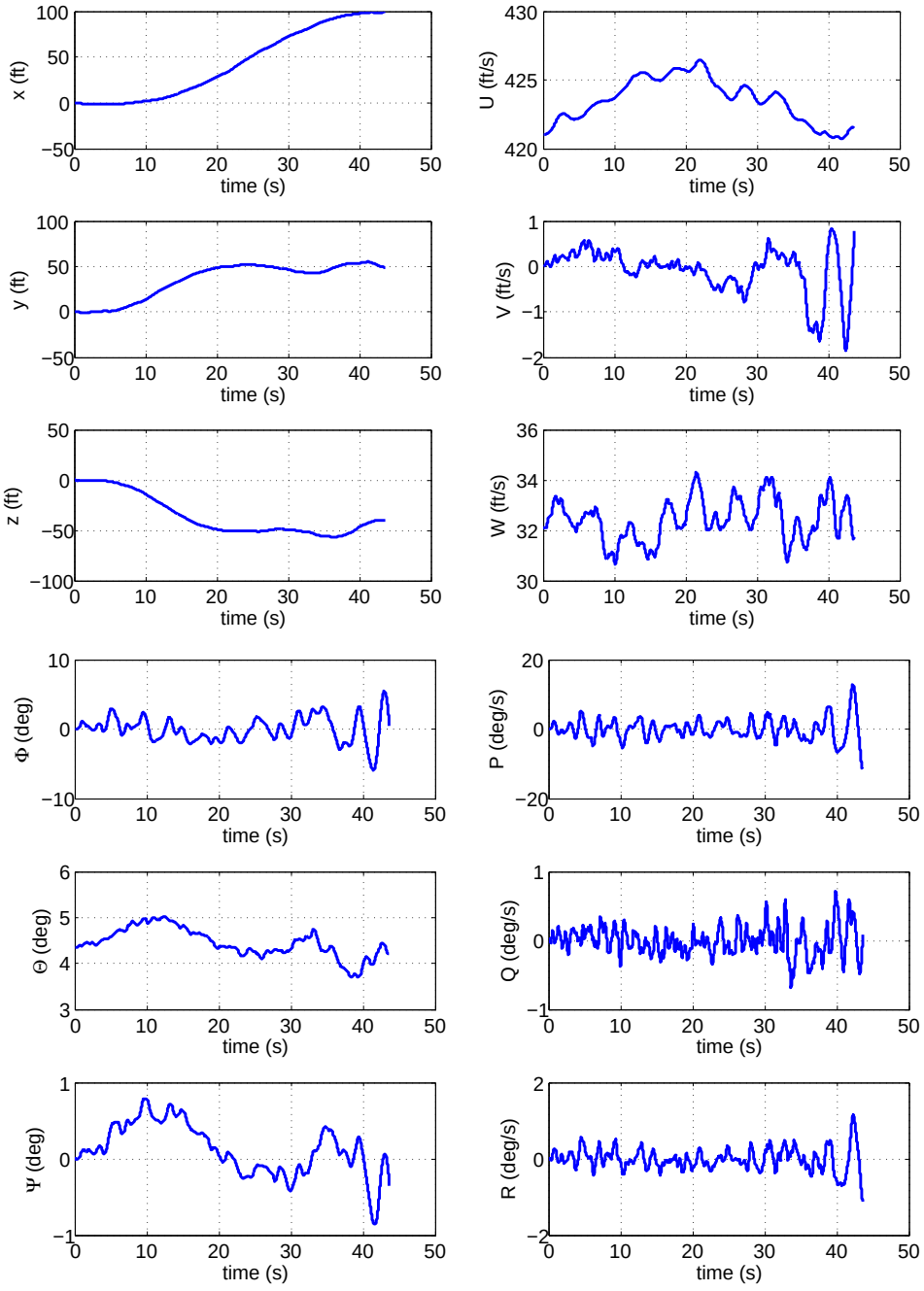

Fig. 57. Receiver aircraft states (case 4, severe turbulence)

the limit of 100 deg/s.

Fig. 59 shows the error in the navigation solution from VisNav, along with the 3σ bounds from the GLSDC algorithm. The initial estimation error begins at about 3 ft in position, and converges to zero as the sensor moves closer to the beacon array, and more measurements are taken. By the time measurements from VisNav are used in the control law at $t = 25$, the position estimate is within 1 ft of the true value. Noise from the sensor shows up at a frequency of 100 Hz, which is the rate at which GLSDC produces and updated estimate. No beacons drop out of the field of view during the maneuver. The severe turbulence does not appear to affect the ability of VisNav to obtain a solution in this case.

The Kalman filter was tuned using the simulation results discussed above. The values of the tuning parameters which give the best fit are

$$\begin{aligned} q_1 &= 1 \\ q_2 &= 0.01 \end{aligned}$$

The tuning parameters are the same as those determined for all cases. The tuned Kalman filter results are shown in Fig. 60. Although there are several places where the estimation error exceeds the 3σ bounds in the first few seconds of case 4, the performance is about the same as cases 1, 2, and 3 after the solution converges. It takes about 10 seconds for the Kalman filter estimation error to converge within the 3σ bounds. The Kalman filter decreases both the magnitude and the frequency of the estimation error from VisNav. Compared to GLSDC alone, the estimation error in position is reduced by almost half. A direct comparison of the estimation error is shown in Fig. 61.

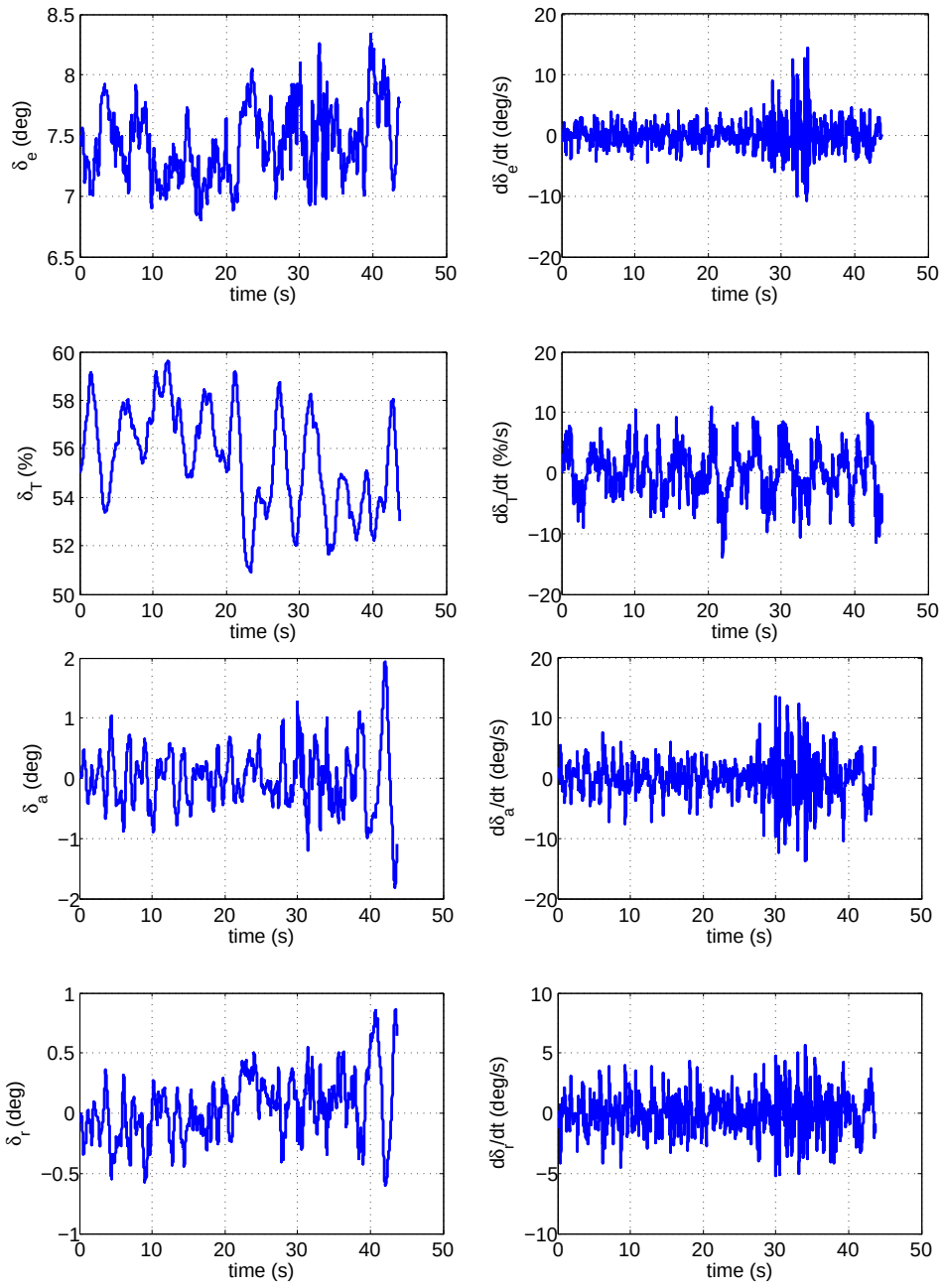

Fig. 58. Receiver aircraft controls and control rates (case 4, severe turbulence)

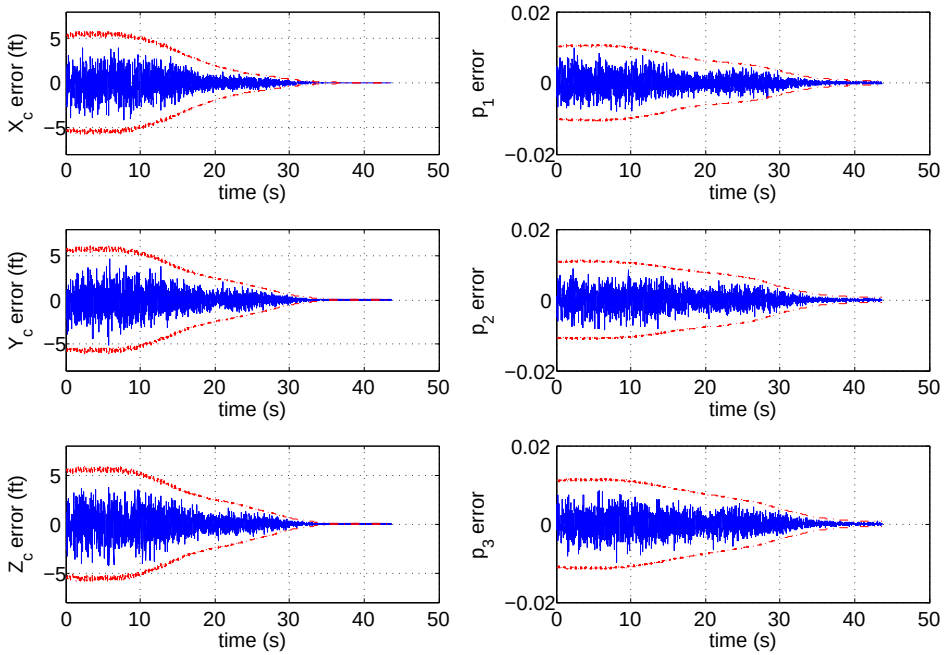

Fig. 59. VisNav error and 3σ bounds from GLSDC (case 4, severe turbulence)

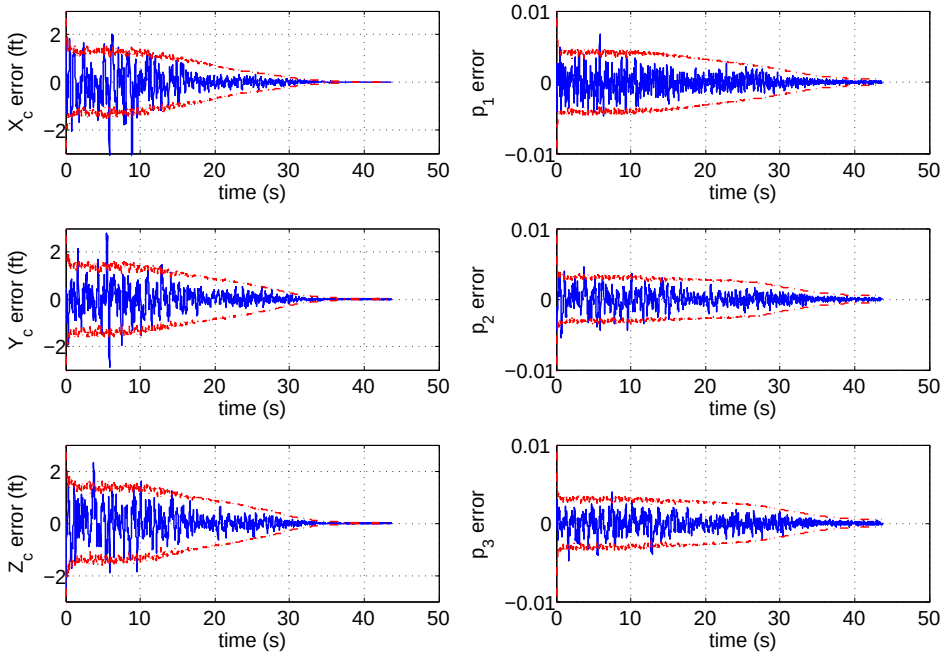

Fig. 60. Tuned Kalman filter error and 3σ bounds (case 4, severe turbulence)

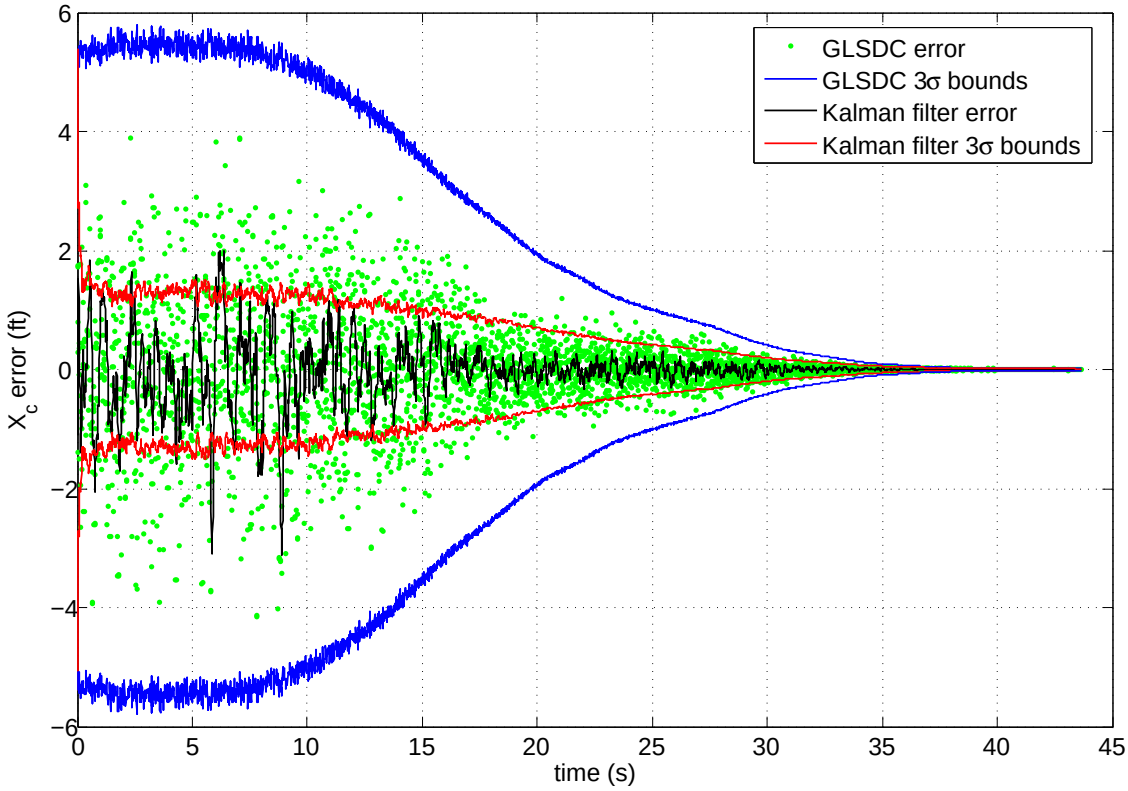

Fig. 61. Comparison of Kalman filter and GLSDC errors (case 4, severe turbulence)

E. Closed-loop Performance with the Kalman Filter

This section presents results of the closed-loop simulations with the tuned Kalman filter in the loop. The values of the tuning parameters for all of the results presented in this section are

$$q_1 = 1$$

$$q_2 = 0.01$$

Subsection 1 presents the results of one simulated aerial refueling in moderate turbulence with the Kalman filter in the loop. Subsection 2 summarizes a series of simulations with and without the Kalman filter in no turbulence, and in light, moderate, and severe turbulence.

1. Moderate Turbulence with Kalman Filter

The refueling scenario simulated for this case is identical to tuning case 3 in Section C, with the exception that the output of the Kalman filter is included in the loop (see Fig. 29). Figs. 62 through 65 present the trajectories, Kalman filter output, and the receiver aircraft states and controls for this case. The random nature of the gust inputs and sensor noise cause the results to be slightly different than case 3, however the results are in general very similar. This is due to the fact that when the second stage of the maneuver begins, the errors from VisNav have already converged to very small values, and the improvement from the Kalman filter is not as significant as it is in the beginning of the simulation. The receiver aircraft does not achieve a successful docking in this case, however the final docking error is 4.01 inches, just above the criteria of 4 inches. The receiver states have small excursions from their steady-state values, and the controls do not exceed position or rate limits.

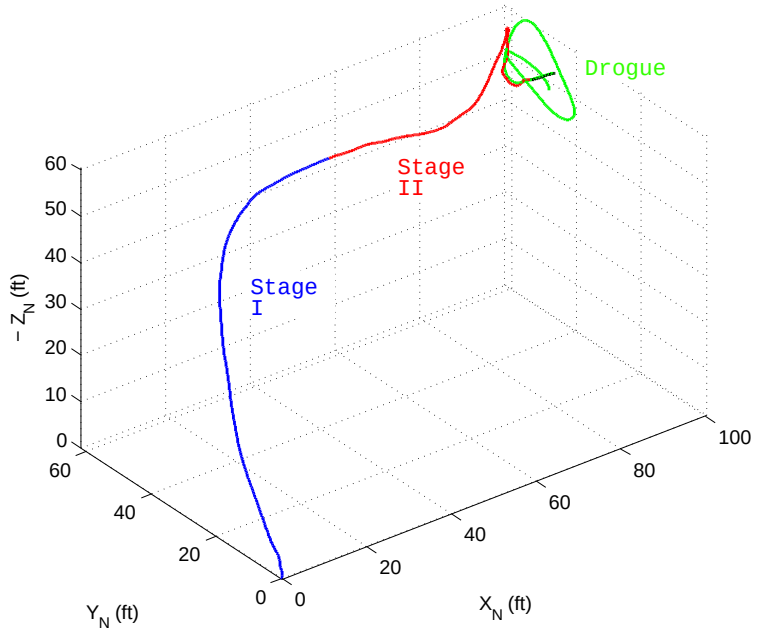

Fig. 62. Receiver aircraft and drogue trajectories, moderate turbulence, with Kalman filter

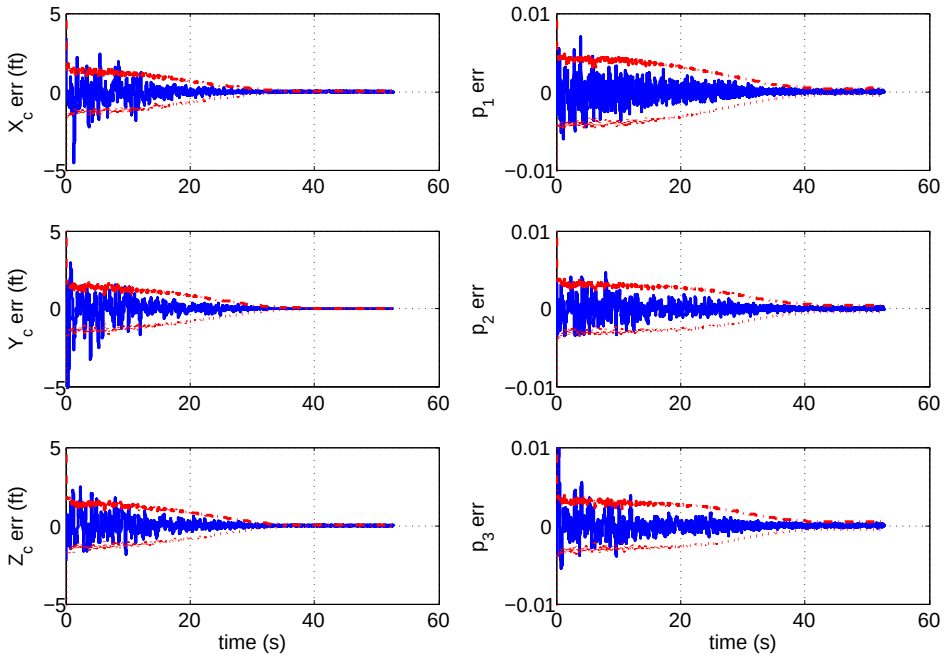

Fig. 63. Kalman filter error and 3σ bounds, moderate turbulence

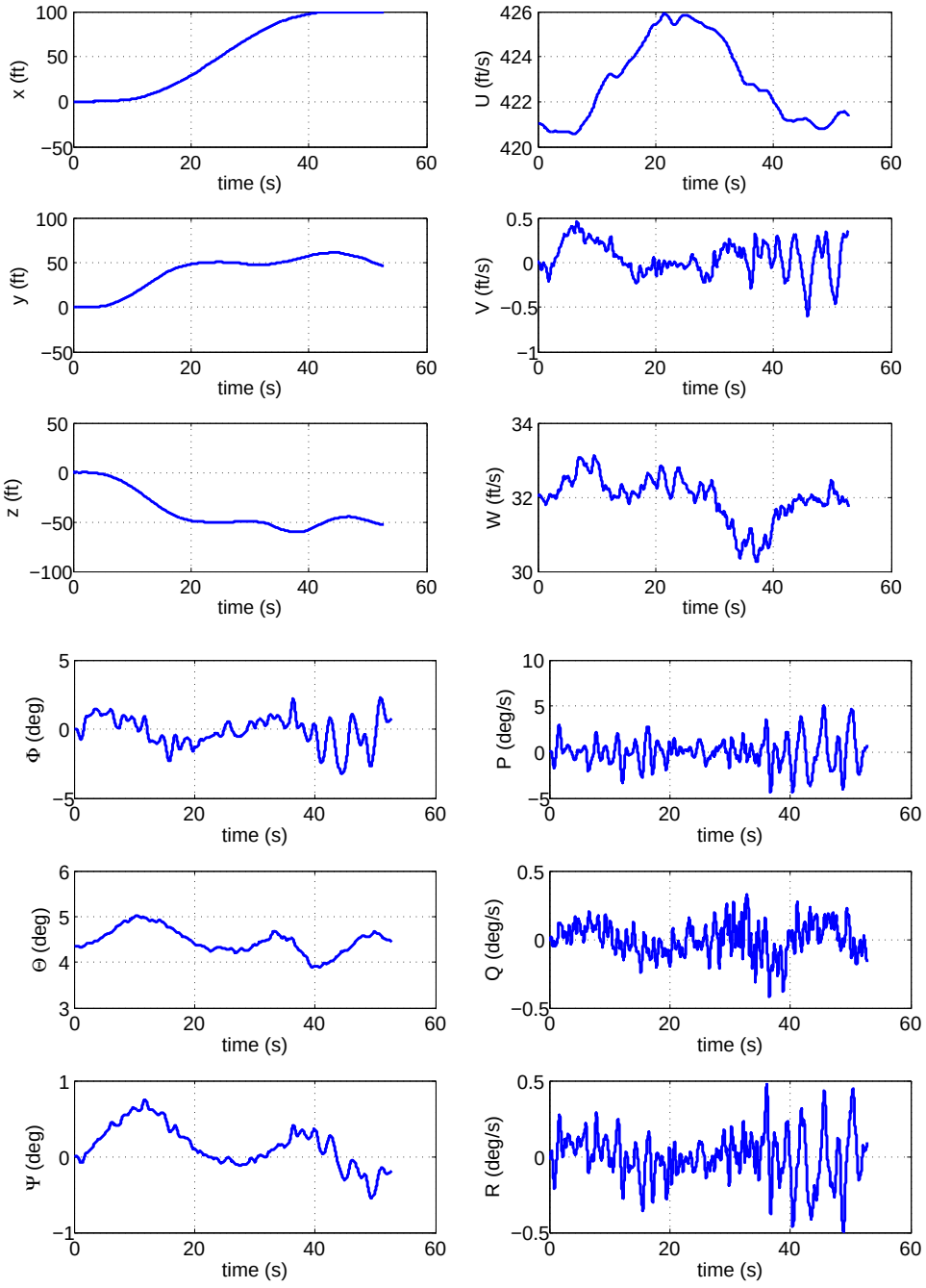

Fig. 64. Receiver aircraft states, moderate turbulence, with Kalman filter

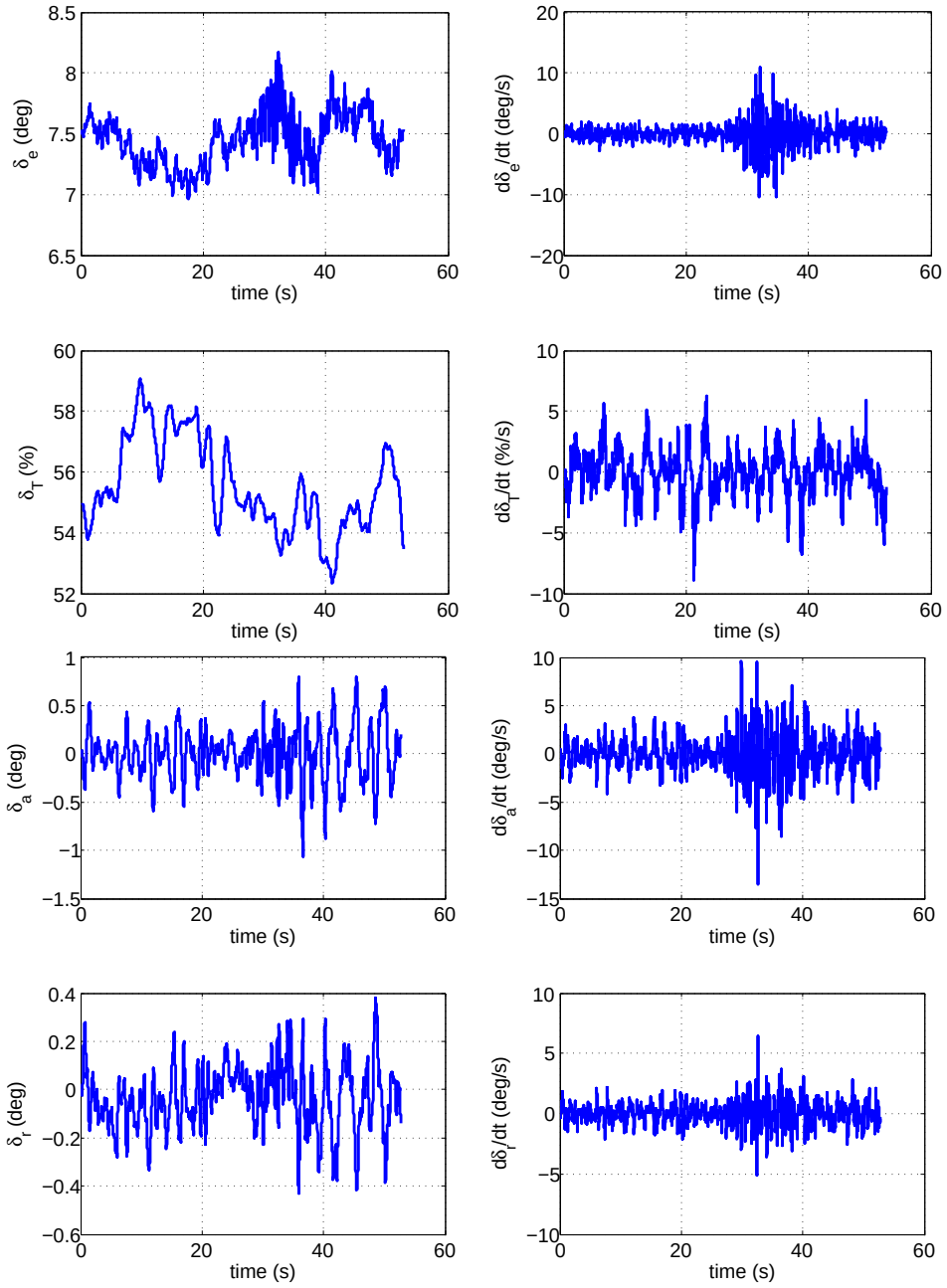

Fig. 65. Receiver aircraft controls, moderate turbulence, with Kalman filter

2. Tuned Kalman Filter Simulation Results

In order to determine the performance improvement afforded by including the Kalman filter after VisNav, a series of simulations was run with and without the filter in the loop for varying levels of turbulence. Tables IX through XII summarize the results of these simulations. The mean error is calculated as the mean of the final docking error over all simulations, evaluated when $(x - x_d) = 0$ as

$$\text{docking error} = \sqrt{(y - y_d)^2 + (z - z_d)^2} \tag{8.1}$$

Successful docking is achieved when the docking error is less than four inches. The level of turbulence intensity (none, light, moderate, and severe) corresponds to the root-mean-square turbulence amplitudes listed in Table VII.

Table IX. Simulation results, no turbulence

	Number of runs	Number of successes	Mean error (inches)	Std. deviation (inches)
VisNav Only	30	30	0.066	0.027
VisNav with Kalman filter	30	30	0.061	0.024

Table X. Simulation results, light turbulence

	Number of runs	Number of successes	Mean error (inches)	Std. deviation (inches)
VisNav Only	30	30	1.213	0.663
VisNav with Kalman filter	30	30	0.838	0.483

Table XI. Simulation results, moderate turbulence

	Number of runs	Number of successes	Mean error (inches)	Std. deviation (inches)
VisNav Only	30	12	5.417	3.517
VisNav with Kalman filter	30	13	4.335	2.779

Table XII. Simulation results, severe turbulence

	Number of runs	Number of successes	Mean error (inches)	Std. deviation (inches)
VisNav Only	30	4	11.033	5.205
VisNav with Kalman filter	30	1	12.749	4.994

In the absence of turbulence, and in light turbulence, the closed-loop system achieves docking for all cases, both with and without the Kalman filter. Tables IX and X show that the mean docking error and standard deviation of the docking error are slightly smaller when the Kalman filter is used in combination with VisNav. Table XI indicates that in moderate turbulence the mean and standard deviation of the final docking error with the Kalman filter are also smaller than with VisNav alone. Without the Kalman filter, successful docking is achieved in 40% of the moderate turbulence cases. This increases to 43% when the Kalman filter is included. Successful docking is rarely achieved in severe turbulence. Four cases of successful docking were achieved with VisNav alone, and only one case of successful docking was achieved with VisNav and the Kalman filter. The mean docking error and standard deviation are roughly the same with and without the Kalman filter in severe turbulence.

F. Summary of Results

This section presents a summary of the simulation results presented in this chapter. Table XIII presents the outcome of each of the four tuning cases. Successful docking was demonstrated for aerial refueling in the cases with no turbulence, light turbulence, and moderate turbulence. The system did not meet the docking criteria for the severe turbulence case, however the final docking error was small. It was found that increasing the value of turbulence intensity results in an increase in the magnitude and frequency of the control inputs and their rates. Even in severe turbulence, however, the controls and control rates of the receiver aircraft remained within the limits specified in Table V. The receiver aircraft state variables remained near steady-state values, confirming the appropriateness of a linear model and linear control methods for this analysis.

The VisNav system performed well in each case, with errors less than 1 foot in relative position over the final stage of the maneuver. No beacons dropped out of the field of view in any of the cases, primarily due to the chosen beacon configuration. Because the beacons were close together, they remained in the field of view of the sensor over the entire range of interest.

The tuning parameters for the Kalman filter were chosen to be the same for each case. The value of RMS turbulence intensity did not significantly affect the tuning or performance of the filter. The Kalman filter improved the navigation solution from VisNav by as much as 50% in the early stages of the maneuver, however the errors from the sensor and the filter both converged to zero as the simulation progressed.

The docking performance of the system with and without the Kalman filter was examined through a series of two-hundred and fourty simulations, summarized in Tables IX through XII. These results showed a slight improvement in the accuracy (as

Table XIII. Summary of tuning cases

	σ (ft/s)	Docking Time (s)	Docking Error (ft)	q_1	q_2
Case 1	0	46.05	0.007	1	0.01
Case 2	1	47.13	0.070	1	0.01
Case 3	5	41.96	0.205	1	0.01
Case 4	10	—	0.756	1	0.01

measured by the mean final docking error) and precision (as measured by the standard deviation of the final docking error) of the closed-loop system with the Kalman filter. The addition of the Kalman filter did not, however significantly improve the probability of a successful docking with any level of turbulence.

CHAPTER IX

CONCLUSIONS

This thesis described the development and simulation of a system intended to enable unmanned aerial vehicles to perform autonomous aerial refueling. The system uses a novel vision based sensor called VisNav, which is capable of providing six degree-of-freedom relative navigation information with an update rate of 100 Hz. A Kalman filter was developed to improve the quality of the navigation solution from VisNav in the presence of measurement noise and sensor errors due to beacon drop-out.

To examine the behavior of VisNav and the Kalman filter in realistic aerial refueling scenarios, a simulation was developed which uses the Reference Observer-based Tracking Controller (ROTC) to achieve autonomous aerial refueling. ROTC includes a trajectory generation module, an observer to estimate the reference states and controls, and a trajectory tracking optimal controller. Simulation results show that VisNav and the ROTC can achieve successful docking in the absence of turbulence, and in Dryden light to moderate turbulence. The Kalman filter was tuned using data from four docking scenarios with varying levels of turbulence intensity. The value of turbulence intensity did not significantly affect the tuning or performance of the filter. The Kalman filter improved the navigation solution from VisNav by as much as 50% in the early stages of the docking scenarios, however the errors from the sensor and the filter both converged to zero as the simulation progressed. The beacon drop-out phenomemon was not observed in the simulation due to the judicious choice of beacon configuration.

A series of closed-loop simulations was performed to compare the docking performance of ROTC with VisNav alone to the performance of ROTC with VisNav and the Kalman filter. Thirty simulated dockings were performed for each of four values

of turbulence intensity without the Kalman filter, and then repeated with the Kalman filter. The mean and standard deviation of the final docking error were compared for each set of simulations with and without the Kalman filter in the loop.

The following conclusions may be made in light of the results presented in this thesis:

1. The value of turbulence intensity did not significantly affect the tuning or performance the Kalman filter. This is most likely due to the chosen sample rate of 100 Hz for the Kalman filter. Because the Kalman filter samples much faster than the relative dynamics, the constant relative acceleration assumption turned out to be good, even in cases with severe turbulence. If the sample rate of the Kalman filter is decreased, the tuning parameters may need to be adjusted based on turbulence intensity. For a sample rate of 100 Hz, however, it may be concluded that the filter only needs to be tuned once for operation in a wide range of turbulence intensity levels. This is significant because the filter may be tuned with a minimal amount of simulation and testing.

2. Post filtering the VisNav sensor with a Kalman filter provides up to a 50% improvement in accuracy in the early stages of the docking scenario, and reduces high-frequency noise from VisNav. In later stages of docking, however, the estimate from VisNav is already very good, and the Kalman filter does not make a significant difference.

3. For the aerial refueling scenarios modeled in this thesis, the addition of the Kalman filter to the VisNav/ROTC structure resulted in a small improvement in the docking accuracy and precision. The Kalman filter did not, however, significantly improve the probability of a successful docking in turbulence.

4. The Reference Observer-based tracking controller achieves successful docking in the presence of sensor noise, modeling uncertainties, and atmospheric turbulence. Unlike the PIF-NSZP-CRW and PIF-CGT-CRW in [23, 24, 25, 26, 43, 29], the ROTC controller does not need *a priori* knowledge of the position or model of the refueling drogue. Even in cases with severe turbulence, the receiver aircraft controls did not exceed position or rate limits, and the aircraft states remained close to steady-state values.

5. The VisNav sensing system's highly accurate relative navigation solution provides excellent tracking capabilities for the autonomous aerial refueling system using the ROTC controller. The VisNav solution is updated at 100 Hz, a rate which is fast enough to track a refueling drogue in moderate to severe turbulence. Spacing the beacons in a compact, asymmetric array with no three beacons in the same plane helps to prevent beacon drop-out in the final stages of docking.

CHAPTER X

RECOMMENDATIONS

This chapter presents recommendations for the VisNav sensor, the ROTC controller, and the autonomous aerial refueling simulation. The VisNav sensor system offers the best solution to the sensor problem in autonomous probe and drogue aerial refueling. There are, however, several issues which must be investigated before the sensor is ready to be used in flight. Several recommendations are made here with the goal of preparing VisNav for realistic flight operations:

1. A way to integrate several sensors such as VisNav, inertial measurement unit (IMU), GPS, and rate gyros should be developed. This may be done using an extended Kalman filter formulation, as in [15]. Such a system would be able to fuse measurements from several sources to obtain a better navigation solution.

2. An investigation into the effects of beacon drop-outs during aerial refueling should be performed. Beacon drop-out is an important factor which affects the tracking performance of any system that uses the VisNav sensor. The beacon arrangement chosen for this research consists of eight beacons concentrated inside a small area on the refueling drogue. Some refueling applications may require a more scattered array, with beacons on the wingtips or empennage of the tanker, for example. This is done to improve the range of the VisNav sensor, however it dramatically increases the chance of beacon drop-outs in the final seconds of the docking maneuver. Although the VisNav simulation in this thesis did not take into account the nonlinear calibration function which is used to map the measured PSD voltages into image-space coordinates, it is noted that this will limit the field of view of the sensor and increase the number of

drop-outs. The optical distortion from the wide angle lens (which is accounted for in the calibration function) can wreak havoc on the GLSDC solution, which assumes an ideal pin-hole camera measurement model.

3. As a solution to the beacon drop-out problem, a new Kalman filter used as a pre-filter should be designed to estimate the position of beacons which are no longer in the field of view. This will avoid discontinuities in the solution from VisNav and improve its performance in the event beacons move out of the field of view.

4. A study of the effects of uncertainty in the locations of the beacons in the target frame should be conducted. In an ideal world, the target-frame beacon locations will be known, but it is not clear what will happen if a beacon is moved inadvertently. In some applications the beacons may move relative to each other during flight; for instance, if some are mounted on the refueling drogue and some on the tanker aircraft itself. It is not known what level of uncertainty is tolerable before the relative navigation solution is not accurate enough for control purposes.

The simulated air refueling scenarios in this thesis demonstrated the ability of the Reference Observer-based Tracking controller to achieve successful docking between the receiver aircraft and the refueling drogue. This was done assuming that the full state vector of the receiver aircraft is available for feedback, and all of the measured and estimated quantities in the simulation are available at the same update rate (100 Hz). In light of these facts, there are several issues concerning the implementation of the controller which are recommended for future work:

1. The effects of estimating the state vector using an observer or Kalman filter in the feedback loop should be investigated. It is expected that this will add latency and affect the robustness properties of the controller.

2. The effect of multi-rate sampling on the controller should be explored and modeled, considering realistic sensor sample rates and measurement noise.

Finally, it is recommended that the autonomous air refueling simulation developed for this thesis be further developed to act as a tool for the evaluation of future improvements to the AAR system. The simulation should include:

1. A supervisory system to coordinate rendezvous and refueling sequences for multiple UAVs. Designs for aerial refueling supervisory systems are proposed in [43] and [44].

2. An improved drogue model based on empirical data or an analytical model. This is especially important because the tracking performance of the controller was shown to depend on the drogue dynamics. A more accurate drogue model will allow for more realistic design gains to be chosen in the simulation stage of development.

3. The aerodynamic interactions and wake effects from the tanker aircraft on the refueling drogue and the receiver aircraft.

REFERENCES

[1] J. L. Stephenson, "The air refueling receiver that does not complain," Master's thesis, School of Advanced Airpower Studies, Maxwell Air Force Base, AL, Oct. 1999.

[2] J. L. Junkins, D. C. Hughes, K. P. Wazni, and V. Pariyapong, "Vision-based navigation for rendezvous, docking, and proximity operations," in *22nd Annual AAS Guidance and Control Conference*, Breckenridge, CO, Feb. 1999, paper AAS-99-021.

[3] M. May, "Gas stations in the sky," *American Heritage of Invention & Technology*, vol. 19, no. 4, pp. 10–19, 2004.

[4] W. P. Maiersperger, "General design aspects of flight refueling," *Aeronautical Engineering Review*, vol. 13, no. 3, pp. 52–61, March 1954.

[5] P. S. Killingsworth, *Multipoint Aerial Refueling, A Review and Assessment*. Santa Monica, CA: Rand, 1996.

[6] A. W. Bloy and M. M. Khan, "Modeling of the receiver aircraft in air-to-air refueling," *Journal of Aircraft*, vol. 38, no. 2, pp. 393–396, Apr. 2001.

[7] W. B. Blake, E. G. Dickes, and D. R. Gingras, "UAV aerial refueling - wind tunnel results and comparison with analytical predictions," in *AIAA Atmospheric Flight Mechanics Conference and Exhibit*, Providence, RI, Aug. 2004, paper AIAA-2004-4820.

[8] J. L. Hansen, J. E. Murray, and N. V. Campos, "The NASA Dryden AAR project: A flight test approach to an aerial refueling system," in *AIAA Atmo-*

spheric Flight Mechanics Conference and Exhibit, Providence, RI, Aug. 2004, paper AIAA-2004-4939.

[9] J. Vassberg, D. Yeh, A. Blair, and J. Evert, "Numerical simulations of KC-10 centerline aerial refueling hose-drogue dynamics with a reel take-up system," in *AIAA Applied Aerodynamics Conference and Exhibit*, Providence, RI, Aug. 2004, paper AIAA-2004-4719.

[10] S. Venkataramanan and A. Dogan, "Dynamic effects of trailing vortex with turbulence & time-varying inertia in aerial refueling," in *AIAA Atmospheric Flight Mechanics Conference and Exhibit*, Providence, RI, Aug. 2004, paper AIAA-2004-4945.

[11] "DGPS general information," U.S. Coast Guard Navigation Center, 2005. [Online]. Available: http://www.navcen.uscg.gov/dgps

[12] M. Fravolini, A. Ficola, M. Napolitano, G. Campa, and M. Perhinschi, "Development of modeling and control tools for aerial refueling for UAVs," in *AIAA Guidance, Navigation, and Control Conference and Exhibit*, Austin, TX, Aug. 2003, paper AIAA-2003-5798.

[13] G. Campa, B. Seanor, M. Perhinschi, M. Fravolini, A. Ficola, and M. Napolitano, "Autonomous aerial refueling for UAVs using a combined GPS-machine vision guidance," in *AIAA Guidance, Navigation, and Control Conference and Exhibit*, Providence, RI, Aug. 2004, paper AIAA-2004-5350.

[14] R. Alonso, J. L. Crassidis, and J. L. Junkins, "Vision-based relative navigation for formation flying of spacecraft," in *AIAA Guidance, Navigation, and Control Conference and Exhibit*, Denver, CO, Aug. 2000, paper AIAA-2000-4439.

[15] B. Awalt, D. Turner, R. Miller, and W.-S. Chen, "Extended Kalman filter applications to multi-vehicle UAV cooperative controls," in *2nd AIAA "Unmanned and Unlimited" Systems, Technologies, and Operations*, San Diego, CA, Sept. 2003, paper AIAA-2003-6538.

[16] B. Sinopoli, M. Micheli, G. Donato, and T. J. Koo, "Vision based navigation for an unmanned aerial vehicle," in *Proceedings of the IEEE International Conference on Robotics & Automation*, Seoul, Korea, May 2001, pp. 1757–1764.

[17] S. Saripalli, J. F. Montgomery, and G. S. Sukhatme, "Visually guided landing of an unmanned aerial vehicle," vol. 19, no. 3, pp. 371–380, June 2003.

[18] L. Pollini, G. Campa, F. Giulietti, and M. Innocenti, "Virtual simulation setup for UAVs aerial refueling," in *AIAA Modeling and Simulation Technologies Conference and Exhibit*, Austin, TX, Aug. 2003, paper AIAA-2003-5682.

[19] L. Pollini, R. Mati, and M. Innocenti, "Experimental evaluation of vision algorithms for formation flight and aerial refueling," in *AIAA Modeling and Simulation Technologies Conference and Exhibit*, Providence, RI, Aug. 2004, paper AIAA-2004-4918.

[20] J. L. Junkins, H. Schaub, and D. Hughes, "Noncontact position and orientation measurement system and method," U.S. Patent 6,266,142, 2001.

[21] W. Williamson, M. Abdel-Hafez, I. Rhee, E. J. Song, J. Wolfe, D. Cooper, D. Chichka, and J. L. Speyer, "An instrumentation system applied to formation flight," in *AIAA 1st Technical Conference and Workshop on Unmanned Aerospace Vehicles, Technologies, and Operations*, Portsmouth, VA, May 2002, paper AIAA-2002-3430.

[22] M. Pachter, C. H. Houpis, and D. W. Trosen, "Design of an air-to-air automatic refueling flight control system using quantitative feedback theory," *International Journal of Robust and Nonlinear Control*, vol. 7, no. 6, pp. 561–580, June 1997.

[23] J. Valasek, J. Kimmett, D. Hughes, K. Gunnam, and J. L. Junkins, "Vision based sensor and navigation system for autonomous aerial refueling," in *AIAA 1st Technical Conference and Workshop on Unmanned Aerospace Vehicles, Technologies, and Operations*, Portsmouth, VA, May 2002, paper AIAA-2002-3441.

[24] J. Kimmett, J. Valasek, and J. L. Junkins, "Autonomous aerial refueling utilizing a vision based navigation system," in *AIAA Guidance, Navigation, and Control Conference*, Monterey, CA, Aug. 2002, paper AIAA-2002-4469.

[25] J. Valasek, K. Gunnam, J. Kimmett, M. Tandale, J. L. Junkins, and D. Hughes, "Vision-based sensor and navigation system for autonomous air refueling," *Journal of Guidance, Control, and Dynamics*, 2005, (accepted).

[26] J. Kimmett, J. Valasek, and J. L. Junkins, "Vision based controller for autonomous aerial refueling," in *Proceedings of the IEEE Control Systems Society Conference on Control Applications*, Glasgow, Scotland, Sept. 2002, paper CCA02-CCAREG-1126.

[27] M. Tandale, R. Bowers, and J. Valasek, "A robust trajectory tracking controller for vision based autonomous aerial refueling of unmanned aircraft," in *AIAA Guidance, Navigation, and Control Conference and Exhibit*, San Francisco, CA, Aug. 2005, paper AIAA-2005-5868.

[28] V. Stepanyan, E. Lavretsky, and N. Hovakimyan, "Aerial refueling autopilot design methodology: Application to F-16 aircraft model," in *AIAA Guidance,*

Navigation, and Control Conference, Providence, RI, Aug. 2004, paper AIAA-2004-5321.

[29] J. J. Kimmett, "Autonomous aerial refueling of UAVs utilizing a vision based navigation system," Master's thesis, Texas A&M University, Department of Aerospace Engineering, College Station, TX, Aug. 2002.

[30] H. Schaub and J. L. Junkins, *Analytical Mechanics of Aerospace Systems*. Reston, VA: American Institute of Aeronautics and Astronautics, 2003.

[31] J. L. Crassidis and J. L. Junkins, *Optimal Estimation of Dynamic Systems*. Boca Raton, FL: Chapman & Hall/CRC, 2004.

[32] D. C. Montgomery and G. C. Runger, *Applied Statistics and Probability for Engineers*, 3rd ed. New York, NY: John Wiley & Sons, Inc., 2003.

[33] F. L. Lewis and V. L. Syrmos, *Optimal Control*. New York, NY: John Wiley & Sons, 1995.

[34] P. Dorato and A. H. Levis, "Optimal linear regulators: The discrete-time case," vol. 16, no. 6, pp. 613–620, Dec. 1971.

[35] J. Valasek, "Digital control of aerospace systems, course notes," Texas A&M University, Department of Aerospace Engineering, Fall 2003 (unpublished).

[36] G. E. Ziegler, "Conceptual aircraft dynamics from inverse aircraft modeling," Master's thesis, Texas A&M University, Department of Aerospace Engineering, College Station, TX, December 1999.

[37] J. Roskam, *Airplane Flight Dynamics and Automatic Flight Controls*. Lawrence, KS: DARcorporation, 2001.

[38] "Automated air refueling movie collection," NASA Dryden Flight Research Center, 2003. [Online]. Available: http://www.dfrc.nasa.gov/Gallery/Movie/AAR/

[39] "Military specification, flying qualities of piloted airplanes," MIL-F-8785C, Nov. 1980.

[40] "Aerospace blockset, Dryden wind turbulence model," The MathWorks, Inc., 2005. [Online]. Available: http://www.mathworks.com/

[41] J. Valasek, "High fidelity flight simulation of autonomous air refueling using a vision based sensor," Flight Simulation Laboratory, Texas A&M University, College Station, TX, Final Technical Report, January 2005.

[42] M. Bandak, Sargent Fletcher, Inc., Jan. 2002, private communication.

[43] J. Valasek and J. L. Junkins, "Intelligent control systems and vision based navigation to enable autonomous aerial refueling of UAVs," in *27th Annual AAS Guidance and Control Conference*, Breckenridge, CO, Feb. 2004, paper AAS-04-012.

[44] K. Subbarao and A. Dogan, "Intelligent integrated sensor, control and maneuver mapping architecture for autonomous vehicle rendezvous and docking," in *3rd AIAA "Unmanned and Unlimited" Systems, Technologies, and Operations*, San Diego, CA, Sept. 2004, paper AIAA-2004-6573.

APPENDIX A

UCAV6 LINEAR MODEL

The six degree-of-freedom aircraft motion variables for building a linear model consist of the three body-axis components of the airplane velocity vector (U, V, W), the body-axis components of angular velocity (P, Q, R), and the attitude of the aircraft relative to the inertial frame, expressed as 3-2-1 Euler attitude angles, (Ψ, Θ, Φ). Each independent motion variable may be expressed as the sum of a steady-state value and a perturbation:

$$\begin{array}{lllllllll} U & = & U_1 + u & P & = & P_1 + p & \Psi & = & \Psi_1 + \psi \\ V & = & V_1 + v & Q & = & Q_1 + q & \Theta & = & \Theta_1 + \theta \\ W & = & W_1 + w & R & = & R_1 + r & \Phi & = & \Phi_1 + \phi \end{array} \tag{A.1}$$

The steady-state flight condition considered in this research is steady, level $1g$ trim. In this equilibrium state, the aircraft experiences no net translational acceleration or rotational velocity. In terms of the motion variables, steady, level $1g$ trim means that

$$\begin{array}{lllllllll} V_1 & = & 0 & \Phi_1 & = & 0 & \Psi_1 & = & 0 \\ P_1 & = & 0 & Q_1 & = & 0 & R_1 & = & 0 \end{array} \tag{A.2}$$

and the steady-state values of U_1, W_1, Θ_1, are known constants.

The six degree-of-freedom aircraft equations of motion may be linearized about the steady-state flight condition, as described in [37]. The UCAV6 equations of motion are thus represented as

$$\dot{\underline{\mathbf{x}}}(t) = \mathcal{A}\underline{\mathbf{x}}(t) + \mathcal{B}\mathbf{u}(t) + \mathcal{G}\mathbf{w}_g(t) \tag{A.3}$$

where the state vector $\underline{\mathbf{x}} \in \Re^9$ is composed of the perturbed motion variables

$$\underline{\mathbf{x}} = \begin{bmatrix} u & v & w & p & q & r & \phi & \theta & \psi \end{bmatrix}^T \tag{A.4}$$

and the control vector $\mathbf{u} \in \Re^4$ are the perturbed control variables

$$\mathbf{u} = \begin{bmatrix} \delta_e & \delta_t & \delta_a & \delta_r \end{bmatrix}^T \tag{A.5}$$

The exogenous input is composed of disturbances to the three body-axis velocities from gusts:

$$\mathbf{w}_g = \begin{bmatrix} u_{gust} & v_{gust} & w_{gust} \end{bmatrix}^T \tag{A.6}$$

The state matrix $\mathcal{A}$ and control distribution matrix $\mathcal{B}$, which were found using the simulation described in [36], are given as

$$\mathcal{A} = \begin{bmatrix} -0.0343 & 0 & 0.1618 & 0 & -32.00 & 0 & 0 & -32.02 & 0 \\ 0 & -0.3326 & 0 & 32.00 & 0 & -418.1 & 32.02 & 0 & 0 \\ -0.0658 & 0 & -1.347 & 0 & 409.5 & 0 & 0 & -2.434 & 0 \\ 0 & -0.0192 & 0 & -3.643 & 0 & 1.725 & 0 & 0 & 0 \\ -0.0007 & 0 & -0.0225 & 0 & -0.7782 & 0 & 0 & 0 & 0 \\ 0 & 0.0178 & 0 & -0.2158 & 0 & -1.192 & 0 & 0 & 0 \\ 0 & 0 & 0 & 1 & 0 & 0.0760 & 0 & 0 & 0 \\ 0 & 0 & 0 & 0 & 1 & 0 & 0 & 0 & 0 \\ 0 & 0 & 0 & 0 & 0 & 1.003 & 0 & 0 & 0 \end{bmatrix}$$

$$\mathcal{B} = \begin{bmatrix} 0.0081 & 0.2559 & 0 & 0 \\ 0 & 0 & -0.2945 & 0.4481 \\ 0.2772 & 0.2286 & 0 & 0 \\ 0 & 0 & 0.5171 & 0.0704 \\ 0.1164 & 0.0143 & 0 & 0 \\ 0 & 0 & 0.0239 & -0.0895 \\ 0 & 0 & 0 & 0 \\ 0 & 0 & 0 & 0 \\ 0 & 0 & 0 & 0 \end{bmatrix}$$

and the disturbance distribution matrix $\mathcal{G}$ is given as

$$\mathcal{G} = \begin{bmatrix} 0.0343 & 0 & -0.1618 \\ 0 & 0.3326 & 0 \\ 0.0658 & 0 & 1.347 \\ 0 & 0.0192 & 0 \\ 0.0007 & 0 & 0.0225 \\ 0 & -0.0178 & 0 \\ 0 & 0 & 0 \\ 0 & 0 & 0 \\ 0 & 0 & 0 \end{bmatrix}$$

For control purposes, the inertial coordinates of the receiver aircraft relative to the steady-state flight path (x, y, z) are added as states. To do this, the relationship

between the inertial coordinate frame and the body-fixed coordinate frame is utilized. The inertial coordinates of the aircraft are defined as (X, Y, Z); thus the components of the airplane's velocity in inertial coordinates are $(\dot{X}, \dot{Y}, \dot{Z})$. The 3-2-1 Euler angles (Ψ, Θ, Φ) represent the attitude of the body-fixed frame B with respect to the inertial, or earth-fixed, frame N. The velocity of the aircraft in inertial frame coordinates is related to the velocity expressed in the body frame coordinates with

$$\begin{bmatrix} \dot{X} \\ \dot{Y} \\ \dot{Z} \end{bmatrix} = \begin{bmatrix} c\Theta c\Psi & s\Phi s\Theta c\Psi - c\Phi s\Psi & c\Phi s\Theta c\Psi + s\Phi s\Psi \\ c\Theta s\Psi & s\Phi s\Theta s\Psi + c\Phi c\Psi & c\Phi s\Theta s\Psi - s\Phi c\Psi \\ -s\Theta & s\Phi c\Theta & c\Phi c\Theta \end{bmatrix} \begin{bmatrix} U \\ V \\ W \end{bmatrix} \tag{A.7}$$

where the trigonometric functions sin and cos have been abbreviated as s and c. (A.7) may also be linearized about the steady-state flight condition. Using the assumptions in (A.2) and neglecting higher-order terms, the following approximations are obtained:

$$\dot{X} \approx \dot{X}_1 + \dot{x} \tag{A.8}$$

$$\dot{Y} \approx \dot{Y}_1 + \dot{y} \tag{A.9}$$

$$\dot{Z} \approx \dot{Z}_1 + \dot{z} \tag{A.10}$$

where the known steady-state flight path is given by

$$\dot{X}_1 = U_1 \cos\Theta_1 + W_1 \sin\Theta_1 \tag{A.11}$$

$$\dot{Y}_1 = 0 \tag{A.12}$$

$$\dot{Z}_1 = -U_1 \sin\Theta_1 + W_1 \cos\Theta_1 \tag{A.13}$$

and the perturbations from steady-state are

$$\dot{x} = \cos\Theta_1 u + \sin\Theta_1 w + (W_1\cos\Theta_1 - U_1\sin\Theta_1)\theta \quad (A.14)$$

$$\dot{y} = v + (U_1\cos\Theta_1 + W_1\sin\Theta_1)\psi - W_1\phi \quad (A.15)$$

$$\dot{z} = -\sin\Theta_1 u + \cos\Theta_1 w - (U_1\cos\Theta_1 + W_1\sin\Theta_1)\theta \quad (A.16)$$

Equations (A.14) through (A.16) represent the trajectory of the receiver relative to the steady-state flight path expressed in inertial coordinates. They are linear in terms of the perturbed state variables u, w, v, ψ, θ, and ϕ. The inertial coordinates x, y, and z may be included as states in the linear model in (A.3). The augmented state vector is

$$\mathbf{x} = \begin{bmatrix} x & y & z & u & v & w & p & q & r & \phi & \theta & \psi \end{bmatrix}^T \quad (A.17)$$

and the new state equation is

$$\dot{\mathbf{x}}(t) = A\mathbf{x}(t) + B\mathbf{u}(t) + G\mathbf{w}_g(t) \quad (A.18)$$

where

$$A = \begin{bmatrix} \mathbf{0} & A_1 \\ \mathbf{0} & \mathcal{A} \end{bmatrix} \quad B = \begin{bmatrix} \mathbf{0} \\ \mathcal{B} \end{bmatrix} \quad G = \begin{bmatrix} \mathbf{0} \\ \mathcal{G} \end{bmatrix}$$

and A_1 is formed from (A.14)-(A.15) using the steady-state values for UCAV6 from Table III

$$A_1 = \begin{bmatrix} 0.9971 & 0 & 0.0759 & 0 & 0 & 0 & 0 & 0 & 0 \\ 0 & 1 & 0 & 0 & 0 & 0 & -32.06 & 0 & 422.3 \\ -0.0759 & 0 & 0.9971 & 0 & 0 & 0 & 0 & -422.3 & 0 \end{bmatrix} \quad (A.19)$$

The output of the system is chosen as the three position states

$$\mathbf{y} = \begin{bmatrix} x & y & z \end{bmatrix}^T \quad (A.20)$$

Thus the output equation may be written as

$$\mathbf{y} = C\mathbf{x} \tag{A.21}$$

where

$$C = \begin{bmatrix} 1 & 0 & 0 & 0 & 0 & 0 & 0 & 0 & 0 & 0 & 0 & 0 \\ 0 & 1 & 0 & 0 & 0 & 0 & 0 & 0 & 0 & 0 & 0 & 0 \\ 0 & 0 & 1 & 0 & 0 & 0 & 0 & 0 & 0 & 0 & 0 & 0 \end{bmatrix}$$

The linear time-invariant UCAV6 model which is used in the control design and simulation for this thesis is given by

$$\begin{aligned} \dot{\mathbf{x}}(t) &= A\mathbf{x}(t) + B\mathbf{u}(t) \\ \mathbf{y}(t) &= C\mathbf{x}(t) \end{aligned} \tag{A.22}$$

VITA

Roshawn Elizabeth Bowers graduated from Kilgore High School in Kilgore, Texas in 1997. She subsequently attended Texas A&M University, where she received her Bachelor of Science in Aerospace Engineering (2002), and Master of Science in Aerospace Engineering (2005). Upon completion of her graduate degree, she accepted employment at Northrop Grumman Integrated Systems in El Segundo, California. She may be contacted via her permanent address,

1301 Coryell

League City, Texas 77573

PUBLICATION

M. Tandale, R. Bowers, and J. Valasek, "A robust trajectory tracking controller for vision based autonomous aerial refueling of unmanned aircraft." in *AIAA Guidance, Navigation, and Control Conference and Exhibit*, San Francisco, CA, Aug. 2005, paper AIAA-2005-5868.